EFFECT OF TURBULENT TRANSPORT MODELS AND GRID SPACING ON PANS CALCULATIONS OF A LID-DRIVEN CAVITY

A Thesis

by

ADITYA MURTHI

Submitted to the Office of Graduate Studies of
Texas A&M University
in partial fulfillment of the requirements for the degree of

MASTER OF SCIENCE

August 2004

Major Subject: Aerospace Engineering

EFFECT OF TURBULENT TRANSPORT MODELS AND GRID SPACING ON PANS CALCULATIONS OF A LID-DRIVEN CAVITY

A Thesis

by

ADITYA MURTHI

Submitted to Texas A&M University
in partial fulfillment of the requirements
for the degree of

MASTER OF SCIENCE

Approved as to style and content by:

Sharath S Girimaji (Chair of Committee)	Rodney D Bowersox (Member)
Prabir Daripa (Member)	Walter E. Haisler (Head of Department)

August 2004

Major Subject: Aerospace Engineering

ABSTRACT

Effect of Turbulent Transport Models and Grid Spacing
on PANS Calculations of a Lid-Driven Cavity. (August 2004)
Aditya Murthi, B. En., Amrita Institute of Technology and Science
Chair of Advisory Committee: Dr. Sharath S. Girimaji

The three-dimensional lid-driven cavity flow is investigated at Reynolds Number (Re)=10,000 for a wide range of spanwise aspect-ratios of 3:1:1,1:1:1 and 0.5:1:1, using the PANS (Partially Averaged Navier-Stokes) turbulence closure model. The PANS method is a variable resolution turbulence closure model, where the unresolved-to-total ratios of kinetic energy (f_k) and dissipation (f_ϵ), serve as resolution control parameters. This study focuses on two main aspects of the PANS: first, the evaluation of Turbulent Transport models and second, the effect of grid spacing on accuracy of the numerical solution. The PANS calculations are tested against the LES and experimental results of Jordan (1994), in terms of both qualitative and quantitative quantities. The main conclusions are: (i) for a given f_k value, the Zero-Transport (ZT) model is superior to the Maximum-Transport (MT) model for unresolved dissipation ϵ_u, (ii) both the ZT and the MT models are adequate for unresolved kinetic energy K_u and, (iii) for a given grid size, the results depend heavily on grid spacing especially for larger f_k values.

To my parents Ram and Rajyasree without whom this would not have been possible

ACKNOWLEDGMENTS

It is a pleasure to acknowledge all the individuals who affected my thought process and supported me in various ways during the course of earning a master's degree. First I would like to thank Dr. Sharath S Girimaji, my committe chair, who not only supported me financially, but also provided sound teaching, technical advice and encouragement, without which this thesis would not have materialized. Here, I also note that this thesis has evolved from the Partially-Averaged Navier-Stokes turbulence modeling project supported by NASA, Langley Research Center and Sandia Labs.

I also thank Dr. David H Allen and Dr. Raytcho Lazarov, who provided useful comments, insights, and suggestions on my work and also helped in enhancing my knowledge during my course work. In addition to that, I would also like to thank Dr. Prabir Daripa and Dr. Rodney D Bowersox, who are my committee members, and also Dr. Svetlana Poroseva for their invaluable suggestions that helped this thesis come to completion.

I am also grateful to my friends and colleagues with whom I have worked over the years. In particular, I thank my fellow graduate students, Amarnath Sambasivam, Eunhwan Jeong, Sunil Lakshmipathy and Vijay Ramakrishnan, for their useful discussions, collaboration and support.

Finally, I would like to express my thanks for all the secretarial and administrative support provided by Ms Karen Knabe and Ms Donna Holick.

TABLE OF CONTENTS

CHAPTER Page

I INTRODUCTION 1

A. Overview 1
B. Literature Review 3
1. 2-D Simulations 3
2. Experiments 4
3. 3-D Simulations 5
C. Objective 6

II METHOD OF SOLUTION 8

A. The PANS Turbulence Model 8
1. Theoretical Basis of PANS 9
2. RANS-type Sub-Filter Stress Closure 11
3. The K_u and ϵ_u Model Equations 12

III TURBULENT TRANSPORT MODELS 15

IV PROBLEM SET-UP AND DETAILS OF THE FLUENT FLOW SOLVER 20

A. Problem Formulation Using FLUENT Flow Solver 20
B. Computational Domain 21

V RESULTS AND DISCUSSION 24

1. Maximum-Transport Vs Zero-Transport Model 25
2. Clustered Grid Vs Uniform Grid 46
3. Grid Convergence 67
4. Results for Mixed Model 72
5. Results for SAR=0.5:1:1 and 1:1:1 75

VI SUMMARY AND CONCLUSIONS 78

REFERENCES 80

VITA 84

LIST OF TABLES

TABLE Page

I Grid Sizes for Various f_k Calculations 23

II Grid Sizes and Grading Schemes for Clustered Grid 46

LIST OF FIGURES

FIGURE Page

1 Sketch of the basic features of recirculation in the two-dimensional lid-driven cavity flow 2

2 Sketch of the Taylor-Goertler-Like (TGL) vortex pairs spanning the cavity floor 3

3 Control volume showing flux of K_u and ϵ_u 16

4 The three-dimensional lid-driven cavity setup for SAR = 3:1:1 23

5 Edge mesh grading parameters 25

6 Mean U-Velocity profiles, bottom wall closeup, (RANS, UG) 26

7 Mean V-Velocity profiles, downstream wall closeup, (RANS, UG) . . 27

8 X-Vorticity contours along downstream wall, (RANS, UG) 28

9 Mean U-Velocity profiles, bottom wall closeup, $f_k = 0.7$, (ZT Vs MT) 29

10 Mean V-Velocity profiles, downstream wall closeup, $f_k = 0.7$, (ZT Vs MT) 30

11 X-Vorticity contours along downstream wall, $f_k = 0.7$, (ZT, UG) . . . 31

12 X-Vorticity contours along downstream wall, $f_k = 0.7$, (MT, UG) . . 31

13 Mean U-Velocity profiles, bottom wall closeup, $f_k = 0.4$, (ZT Vs MT) 32

14 Mean V-Velocity profiles, downstream wall closeup, $f_k = 0.4$, (ZT Vs MT) 33

15 X-Vorticity contours along downstream wall, $f_k = 0.4$, (ZT, UG) . . . 34

16 X-Vorticity contours along downstream wall, $f_k = 0.4$, (MT, UG) . . 34

17 Mean U-Velocity profiles, bottom wall closeup, $f_k = 0.2$, (ZT Vs MT) 35

FIGURE Page

18 Mean V-Velocity profiles, downstream wall closeup, $f_k = 0.2$, (ZT Vs MT) 36

19 X-Vorticity contours along downstream wall, $f_k = 0.2$, (ZT, UG) . . . 37

20 X-Vorticity contours along downstream wall, $f_k = 0.2$, (MT, UG) . . 37

21 Mean U-Velocity profiles, bottom wall closeup, (ZT, UG) 38

22 Mean V-Velocity profiles, downstream wall closeup, (ZT, UG) 39

23 Mean U-Velocity profiles, full cavity, (ZT, UG) 40

24 Mean U-Velocity profiles, full cavity, (ZT, UG) 41

25 X-Vorticity contours: $f_k = 0.2$ 42

26 X-Vorticity contours: $f_k = 0.4$ 42

27 X-Vorticity contours: $f_k = 0.7$ 42

28 X-Vorticity contours: RANS 42

29 Spiralling spanwise motions due to interactions among the primary recirculation vortex, downstream secondary eddy, TGL vortex and corner vortices 44

30 Spanwise distribution and streamwise extent of the TGL vortex contours 45

31 Mean U-Velocity profiles, bottom wall closeup, (RANS, CG Vs UG) . 47

32 Mean V-Velocity profiles, downstream wall closeup, (RANS, CG Vs UG) 48

33 X-Vorticity contours along downstream wall, (RANS, CG) 49

34 X-Vorticity contours along downstream wall, (RANS, UG) 49

35 Mean U-Velocity profiles, bottom wall closeup, $f_k = 0.7$, (CG Vs UG) 50

FIGURE Page

36 Mean V-Velocity profiles, downstream wall closeup, $f_k = 0.7$, (CG Vs UG) 51

37 X-Vorticity contours along downstream wall, ($f_k = 0.7$, CG) 52

38 X-Vorticity contours along downstream wall, ($f_k = 0.7$, UG) 52

39 Mean U-Velocity profiles, bottom wall closeup, $f_k = 0.5$, (CG Vs UG) 54

40 Mean V-Velocity profiles, downstream wall closeup, $f_k = 0.5$, (CG Vs UG) 55

41 X-Vorticity contours along downstream wall, ($f_k = 0.5$, CG) 56

42 X-Vorticity contours along downstream wall, ($f_k = 0.5$, UG) 56

43 Mean U-Velocity profiles, bottom wall closeup, $f_k = 0.4$, (CG Vs UG) 57

44 Mean V-Velocity profiles, downstream wall closeup, $f_k = 0.4$, (CG Vs UG) 58

45 X-Vorticity contours along downstream wall, ($f_k = 0.4$, CG) 59

46 X-Vorticity contours along downstream wall, ($f_k = 0.4$, UG) 59

47 Mean U-Velocity profiles, bottom wall closeup, $f_k = 0.2$, (CG Vs UG) 60

48 Mean V-Velocity profiles, downstream wall closeup, $f_k = 0.2$, (CG Vs UG) 61

49 X-Vorticity contours along downstream wall, ($f_k = 0.2$, CG) 62

50 X-Vorticity contours along downstream wall, ($f_k = 0.2$, UG) 62

51 Mean U-Velocity profiles, bottom wall closeup, (ZT, CG) 63

52 Mean V-Velocity profiles, downstream wall closeup, (ZT, CG) 64

53 Mean U-Velocity profiles, full cavity, (ZT, CG) 65

54 Mean U-Velocity profiles, bottom wall closeup, (ZT, CG) 66

55 Mean U-Velocity profiles, (RANS: 81*81*81 Vs 51*51*51) 68

FIGURE Page

56 Mean V-Velocity profiles, (RANS: 81*81*81 Vs 51*51*51) 69

57 Mean U-Velocity profiles, ($f_k = 0.7$: 81*81*81 Vs 64*64*64) 70

58 Mean V-Velocity profiles, ($f_k = 0.7$: 81*81*81 Vs 64*64*64) 71

59 Mean U-Velocity profiles, (Mixed Model, CG) 73

60 Mean V-Velocity profiles, (Mixed Model, CG) 74

61 Mean U-Velocity profiles for SAR = 1:1:1, bottom wall closeup, (ZT, CG) 76

62 Mean U-Velocity profiles for SAR = 0.5:1:1, bottom wall closeup, (ZT, CG) 77

CHAPTER I

INTRODUCTION

A. Overview

With the advent of high-speed computers, detailed numerical simulation of flow physics has been receiving increased acceptance as an efficient and practical scientific investigation method in research institutes and industry. A favorable attribute of the computational fluid dynamics (CFD) technique is its flexibility when conducting *parametric studies* [1]. Not all turbulence simulation methods can be applied to solve practical problems, much less to the treatment of complex geometries. As in any engineering method, a compromise is needed between accuracy of results and the time/cost of effort spent in acquiring the results. Resolving all the scales of a turbulent flow proves to be very costly, while employing highly empirical turbulence models to complex problems could give inaccurate simulation results. PANS (Partially Averaged Navier-Stokes Equations) is a method that serves as a bridge between the highly empirical models and direct computation by being computationally less expensive and time-effective compared to the previous techniques. In this study, PANS calculations have been performed for a *three-dimensional lid-driven cavity.*

The turbulence within a lid-driven cavity is maintained by continuous production of kinetic energy from the lid (moving wall). This production is confined to a very thin viscous layer of fluid next to the lid. The blocking action of the bounding walls and a great variety of other hydrodynamic phenomena unevenly distribute this energy over most of the cavity volume. In order to provide an accurate description of such complex phenomena, the lid-driven cavity needs to be investigated further.

The journal model is the *Journal of Computational Physics.*

The investigation of such a flow is motivated by three major factors. First, the lid-driven cavity flow offers the opportunity to study "stationary captive" primary vortices (Fig.1) [2] as well as a number of complex secondary phenomena such as the corner vortices and the Taylor-Goertler vortices (Fig.2). Second, the flow is a typical representation of several engineering situations, such as flow over cutouts, slots on walls of heat exchangers, the mixing container of chemical plants etc. Third, the problem formulation is straight-forward: the geometry is regular and the boundary conditions are well-posed. For these reasons, this flow a popular test case for various turbulence models and computational schemes.

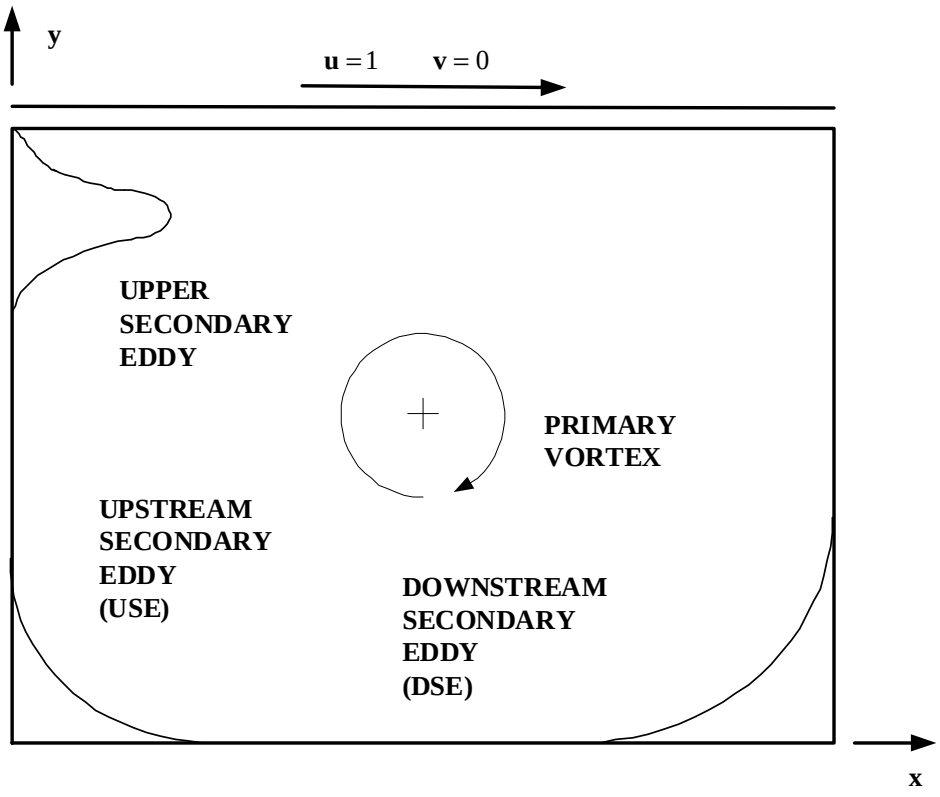

Fig. 1. Sketch of the basic features of recirculation in the two-dimensional lid-driven cavity flow

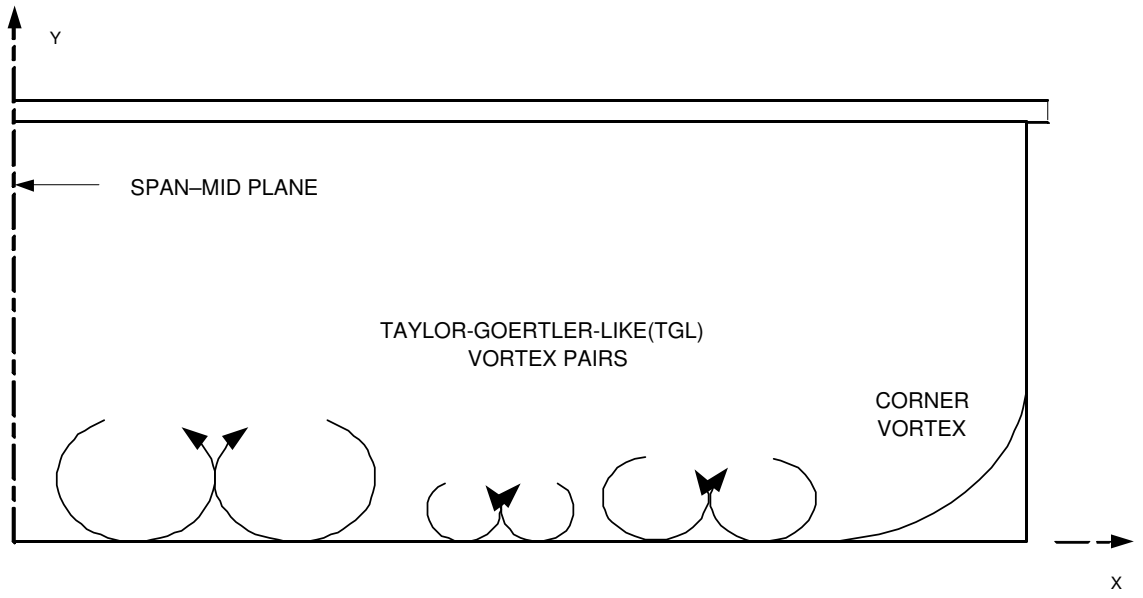

Fig. 2. Sketch of the Taylor-Goertler-Like (TGL) vortex pairs spanning the cavity floor

B. Literature Review

1. 2-D Simulations

A basic test case involves simulating a two-dimensional cavity at a low Reynolds Number ($Re \leq 1000$), wherein the flow is strictly laminar and steady. Some two-dimensional simulations (for example Ghia et al., 1982 [3] and Gustafson and Halasi, 1986 [4]) reveal salient features of steady cavity flow at much higher Reynolds number ($Re \leq 10000$). In particular, the extensive results of Ghia et al. serve best as a basis for comparison of 2D predictions because of the finer grid resolution employed in their simulations, corresponding to a Reynolds number of 10,000. Several numerical investigations have reported the turbulent characteristics of the lid-driven cavity flow (Young et al., 1976 [5], Ideriah, 1978 [6] and Gaskell and Lau, 1988 [7], for instance). Each of the above cited investigations involve simulations performed

on a 2D geometry with turbulence fully modelled. The results obtained primarily focus on validating the the numerical scheme or evaluating a particular turbulence model. Other studies showing the flow evolution in a 2D cavity under an impulsively started lid and an oscillating lid have been reported by Soh and Goodrich (1988) [8]. The above cited two-dimensional efforts have substantially deepened and clarified our qualitative understanding of the complex nature of flow in a cavity driven by a moving solid boundary. It should be emphasized, however, that any realistic flow in a closed cavity of finite cross-section possesses three-dimensional characteristics because of the physically imposed no-slip boundary conditions at the end-walls. This has led to a number of experimental efforts.

2. Experiments

On the experimental front, the lid-driven cavity flow has been investigated by a number of researchers such as Koseff and Street (1984a) [9], Pan and Acrivos, 1967 [10]; Mills, 1965 [11]. In a series of insightful and far-reaching publications, Koseff and Street (1984a-c) [9, 12, 13] presented the results of their elaborate and well-conceived experimental measurements to depict the essential features of fully-developed three-dimensional flows in a driven cavity. By varying the span-to-width ratio (spanwise aspect ratio), complete flow visualization studies were conducted. The main observation that emerged from their experiments was that the flows exhibit inherent three-dimensional features with significant transverse motions, the Taylor-Goertler-like (TGL) vortices and end-wall vortices. A theoretical study of global stability by Ramanan and Homsy (1994) [14] of two-dimensional flow in a square cavity (infinite span), found that for infinitesimal three-dimensional disturbances the critical Reynolds number based on lid velocity and height of the cavity was nearly 600. The

visualization studies of Aidun et al.,(1991) [15] on transition in a cavity of square cross-section but with a spanwise extent three times its height, concluded that this flow becomes unsteady at a Reynolds number of approximately 825. They showed that at first a Taylor instability develops near the downstream during flow startup and the subsequent development of the Taylor-Goertler-like (TGL) vortices in the region of the Downstream Secondary Eddy (DSE) is attributed to the concave viscous shear layer, that forms between the DSE and the primary circulation cell. Moreover their appearance is viewed as a mechanism for transition to turbulence. The size and number of pairs of TGL vortices depend strongly on the Reynolds number and the Spanwise-Aspect Ratio (SAR).

3. 3-D Simulations

Numerical investigations carried out by Jordan and Ragab (1991) [16], include a Direct Numerical Simulation (DNS) that was carried out at $Re = 5000$ and a Large Eddy Simulation (LES) that was carried out at $Re = 10000$, for a SAR of 3:1:1. At $Re = 5000$, the flow was laminar, while the three-dimensionality and unsteadiness of the flow resulted in severe distortion of the basic flow structure. Rapid changes in the size of the TGL vortices were noticed and they were shown to meander along the cavity bottom. At higher Reynolds numbers, the vortices themselves became distorted due to the onset of turbulence. The other important feature that was observed in the spanwise direction was the lower corner vortex. The appearance of this vortex was due to shear and pressure force adjustment in the streamwise recirculating flow caused by the no-slip condition along the end wall. Like the TGL vortices, it was also observed that the corner vortex became unsteady at moderate Reynolds numbers ($Re \geq 3200$). Experimental observations showed the first signs of turbulence

taking place within the free shear layer that lies between the primary vortex and downstream secondary eddy (DSE). This local transition was found to occur at a Reynolds number somewhere between 6000 and 8000 (Koseff and Street, 1984a). If the Reynolds number was increased, the structure of the vortices became obscured due to their diffusion by turbulence. Other published results from three-dimensional simulations includes those of Kim and Moin (1985) [17], Frietas et al.(1985) [18], and Prasad et al. (1988) [19] where the Reynolds number was restricted to low to moderate values ($Re \leq 3200$). In these works, the simulations showed the appearance of quasi-steady and unsteady spanwise TGL vortices along the cavity bottom, which had been observed experimentally.

C. Objective

In the present study, we carry out extensive numerical simulations of the three-dimensional lid-driven cavity flow using the PANS method and compare the results with those from LES and experiment (Jordan, 1994 [16]). The main objectives are:

(i) to test various turbulence transport modeling concepts for unresolved kinetic energy and dissipation

(ii) to determine the effect of grid spacing on PANS and,

(iii) to verify ability of PANS to serve as **bridging** model between RANS and DNS.

The numerical investigation is presented for $Re = 10,000$, over a varying range of spanwise aspect ratios ($SAR = 2L/W$): $0.5:1:1, 1:1:1$ and $3:1:1$. This will be compared with the the complete flow details available from three-dimensional simulations provided by Jordan and Ragab (1994) [16]. Such comparisons would complement and reinforce the three-dimensional flow characteristics that have been

uncovered by the laboratory experiments (Koseff and Street, 1984 a-c [9, 12, 13]), while also validating the predictive abilities of the PANS method in obtaining accurate results. The three-dimensional numerical data generated in the present study will be thoroughly analyzed to illustrate the proximity of the PANS solutions to LES and experiment and hence verifying its ability to serve as a bridging model between RANS and DNS. All the simulations in the present study have been performed using the FLUENT 6.0 software, which is the most widely used commercial fluid flow solver to date.

CHAPTER II

METHOD OF SOLUTION

A. The PANS Turbulence Model

In practical engineering applications, a large number of flows are turbulent in nature and usually involve a wide range of flow scales. The number of scales of motion increase rapidly with Reynolds number and hence not amenable to exact simulation on even the most powerful of computers. In many flows of interest, large scales of fluctuations play important roles in the dynamics of the problem. Thus these large scales of motion need to be resolved accurately. Turbulence modeling techniques such as the Reynolds-averaged Navier-Stokes Equations (RANS), Large-eddy Simulation (LES) and Direct Numerical Simulation (DNS) that were used previously for modeling such flows, either suffer from inherent limitations or are too expensive computationally. As a consequence, researchers have been trying to develop new or improved turbulence modeling techniques that are capable of incorporating some of the useful features of the previous methods (RANS and LES). The main objective of these methods (DES-Spalart, 2000 [20]), hybrid RANS/LES, unsteady Reynolds-averaged Navier Stokes (URANS), limited numerical scales (LNS) method etc.) involves reducing computational time and costs. The Partially Averaged Navier Stokes Equations (PANS) is a recently developed mixed method and it is the subject of this study.

In RANS, the non-linear governing equations are solved for averaged fields, $\overline{U}$, while in LES, equations are solved for filtered fields (large scales), $\langle U \rangle$. The PANS method used in the current study, has been developed for resolving a portion of the large, unsteady scales of motion (partial averaging) by making use of the averaging invariance property (Germano,1992 [21]) of the governing equations. In PANS, as in

LES, the total field is decomposed into resolved and unresolved parts. PANS, however, is distinctly different from LES in three main aspects: (i) the decomposition is based on the fraction (f_k) of kinetic energy (K_u) to be modeled and not on the cut-off wavenumber, (ii) PANS filtering (or averaging) is implied rather than explicit and no filtering is performed, and (iii) the SFS (sub-filter scale) stress ($\tau(V_i, V_j)$) is independent of the grid size (Δ): i.e. the level of physical resolution achievable depends wholly, upon the prescription of f_k and hence is independent of the numerical resolution.

1. Theoretical Basis of PANS

The PANS method is described in detail in Girimaji (2003) [22] and the salient issues are given below. Starting from the instantaneous incompressible flow equations

$$\frac{\partial V_i}{\partial t} + V_j \frac{\partial V_i}{\partial x_j} = -\frac{\partial p}{\partial x_i} + \nu \frac{\partial^2 V_i}{\partial x_j \partial x_j} \tag{2.1}$$

$$\frac{\partial V_i}{\partial x_i} = 0; \tag{2.2}$$

we define $\langle\rangle$ to be a general/arbitrary filtering operator, that is constant preserving and commutes with spatial and temporal differentiation. The instantaneous field can then be decomposed into a filtered field and a residual field:

$$V_i = U_i + u_i \tag{2.3}$$

where $U_i = \langle V_i \rangle$, corresponds to the filtered field and u_i corresponds to the field that needs to be modeled. On applying such a filtering operator to the instantaneous equations we get

$$\frac{\partial \langle V_i \rangle}{\partial t} + \langle V_j \frac{\partial V_i}{\partial x_j} \rangle \;\; = \;\; \frac{\partial \langle V_i \rangle}{\partial t} + \langle \frac{\partial (V_i, V_j)}{\partial x_j} \rangle$$

$$= \frac{\partial \langle V_i \rangle}{\partial t} + \langle V_j \rangle \frac{\partial V_i}{\partial x_j} + \frac{\partial}{\partial x_j}(\langle V_i V_j \rangle - \langle V_i \rangle \langle V_i \rangle) \tag{2.4}$$

from which we get the PANS equations as

$$\begin{aligned} \frac{\partial U_i}{\partial t} + U_j \frac{\partial U_i}{\partial x_j} + \frac{\partial \tau(V_i, V_j)}{\partial x_j} &= -\frac{\partial \langle p \rangle}{\partial x_i} + \nu \frac{\partial^2 \langle V_i \rangle}{\partial x_j \partial x_j} \\ &= -\frac{\partial p_u}{\partial x_i} + \nu \frac{\partial^2 U_i}{\partial x_j \partial x_j} \end{aligned} \tag{2.5}$$

In the above equation, $\tau(V_i, V_j)$ is the generalized second moment as defined by Germano, 1992 [21]. The generalized second and third order moments can be written as

$$\tau(V_i, V_j) = \langle V_i V_j \rangle - \langle V_i \rangle \langle V_j \rangle; \tag{2.6}$$

$$\begin{aligned} \tau(V_i, V_j, V_k) = \langle V_i V_j V_k \rangle &- \tau(V_i, V_j)\langle V_k \rangle - \tau(V_i, V_k)\langle V_j \rangle - \tau(V_j, V_k)\langle V_i \rangle \\ &- \langle V_i \rangle \langle V_j \rangle \langle V_k \rangle \end{aligned} \tag{2.7}$$

Equation 2.5 is **unclosed** with respect to the sub-filter scale stress (SFS) term $\tau(V_i, V_j)$. The evolution equation for the SFS stress is similar in form to its RANS counterpart:

$$\frac{\partial \tau(V_i, V_j)}{\partial t} + U_k \frac{\partial \tau(V_i, V_j)}{\partial x_k} = P_{ij} + \phi_{ij} - D_{ij} + \mathrm{T_{ij}} \tag{2.8}$$

where

$$P_{ij} = -\tau(V_i, V_j)\frac{\partial U_j}{\partial x_k} - \tau(V_j, V_k)\frac{\partial U_i}{\partial x_k}; \tag{2.9}$$

$$\phi_{ij} = 2\tau(p, S_{ij}); \tag{2.10}$$

$$D_{ij} = 2\nu\tau(\frac{\partial U_i}{\partial x_k}, \frac{\partial U_j}{\partial x_k}); \tag{2.11}$$

$$\mathrm{T_{ij}} = -\frac{\partial}{\partial x_k}\Big(\tau(V_i, V_j, V_k) + \tau(p, V_j)\delta_{ik} - \nu\frac{\partial \tau(V_i, V_j)}{\partial x_k}\Big) \tag{2.12}$$

are the terms for production, pressure-strain correlation, dissipation and transport of SFS stresses respectively.

Thus the form of the SFS stress equation is invariant to the type of filter (Germano, 1992 [21]). Consequently, the SFS stress model form must be invariant to the type of averaging provided the generalized central moments are used (Germano, 1992 [21]; Lilly, 1966 [23]; Deardorff, 1970 [24], Khorrami et al, 2002 [25, 26], Girimaji, 2002 [27]).

2. RANS-type Sub-Filter Stress Closure

Based on the arguments presented in the previous section, PANS can inherit its model form from either RANS or LES. Current subgrid LES closures, which are all zero-equation models, are algebraic in nature and hence too elementary to be used as a basis for PANS. Moreover, the advanced two or seven equation RANS models are notably the most sophisticated one-point closures, as complicating physics such as curvature, rotation etc. can be accurately modelled and different physical processes such as return to isotropy, dissipation, production etc. can be accounted for. In PANS the extent of filtering is quantified by specifying the ratios of unresolved kinetic energy and dissipation

$$f_k = \frac{K_u}{K} \quad f_\epsilon = \frac{\epsilon_u}{\epsilon} \tag{2.13}$$

Invoking the **averaging invariance** property, we can use a Boussinesq-type approximation or mixing-length arguments for partial fields as well and hence can close the SFS stress term $\tau(V_i, V_j)$ according to

$$\tau(V_i, V_j) = -\nu_u\Big(\frac{\partial U_i}{\partial x_j} + \frac{\partial U_j}{\partial x_i}\Big) + \frac{2}{3}K_u\delta_{ij}; \quad \text{where} \quad \nu_u = C_\mu\frac{K_u^2}{\epsilon_u} \tag{2.14}$$

From the above equation, it is observed that in order to completely close the SFS stress term, suitable models for K_u and ϵ_u have to be prescribed. In Girimaji (2003 [22]) the equations for K_u and ϵ_u are derived from the RANS two-equation $K-\epsilon$ model:

$$\frac{\partial K}{\partial t}+\overline{U_j}\frac{\partial K}{\partial x_j} = P-\epsilon+\frac{\partial}{\partial x_j}\Big(\frac{\nu_t}{\sigma_k}\frac{\partial K}{\partial x_j}\Big); \tag{2.15}$$

$$\frac{\partial \epsilon}{\partial t}+\overline{U_j}\frac{\partial \epsilon}{\partial x_j} = C_{\epsilon 1}\frac{P\epsilon}{K}-C_{\epsilon 2}\frac{\epsilon^2}{K}+\frac{\partial}{\partial x_j}\Big(\frac{\nu_t}{\sigma_\epsilon}\frac{\partial \epsilon}{\partial x_j}\Big), \tag{2.16}$$

where $\overline{U}$ is the mean velocity, P is the production of kinetic energy, ϵ is the dissipation-rate, ν_t is the total turbulent viscosity ($\nu_t = C_\mu \frac{K^2}{\epsilon}$) and $C_{\epsilon 1}$, $C_{\epsilon 2}$ are model coefficients.

3. The K_u and ϵ_u Model Equations

The model equations for K_u and ϵ_u are derived by considering the following requirements:

(i) the ratios of unresolved to total kinetic energy and dissipation must be equal to f_k and f_ϵ respectively.

(ii) PANS must reduce to RANS as f_k tends to unity and

(iii) PANS must reduce to DNS as f_k tends to zero.

Hence, f_k and f_ϵ serve as resolution control parameters and based on these, the desired level of resolution can be obtained. We are chiefly concerned with decomposition in the inertial scales of motion of length say l_i, that are considerably larger than the smallest Kolomogorov scales (η), i.e. $l_i \gg \eta$. Since the rate of convergence of a turbulence statistic depends on the corresponding length scale, ϵ_u, being a **small scale**($O(\eta)$) quantity, converges to its mean rather quickly. Therefore, it seems reasonable to believe that $\epsilon = \epsilon_u$ for all time (t), in the scales of interest. Hence, f_ϵ is

identically treated as unity and the desired resolution depends solely upon the prescription of f_k. However, if DNS type resolution, $l_i \approx \eta$, is desired then f_ϵ must also be smaller than unity.

Based on the above requirements, the model equation for K_u is written as

$$\begin{aligned} \frac{dK_u}{dt} &= f_k \frac{dK}{dt} \\ \frac{\partial K_u}{\partial t} + U_j \frac{\partial K_u}{\partial x_j} &= f_k \Big(\frac{\partial K}{\partial t} + \overline{U_j} \frac{\partial K}{\partial x_j} \Big) + (U_j - \overline{U_j}) \frac{\partial K_u}{\partial x_j} \\ &= f_k \Big(P - \epsilon + \frac{\partial}{\partial x_j} \Big(\frac{\nu_t}{\sigma_k} \frac{\partial K}{\partial x_j} \Big) \Big) + (U_j - \overline{U_j}) \frac{\partial K_u}{\partial x_j} \end{aligned} \tag{2.17}$$

The evolution equation for K_u can also be derived directly from the Navier–Stokes equation. Then it has the following form:

$$\frac{dK_u}{dt} = P_u - \epsilon_u + T_{k_u} \tag{2.18}$$

where $P_u = \tau(V_i, V_j) \frac{\partial U_i}{\partial x_j}$ corresponds to unresolved production, ϵ_u the unresolved dissipation and T_{k_u} the transport of unresolved kinetic energy. The above two equations (2.16 and 2.17) have to be consistent with one another and therefore after comparing equivalent terms in both equations and expressing all variables in terms of their PANS counterparts we get the evolution equation for K_u as

$$\frac{\partial K_u}{\partial t} + U_j \frac{\partial K_u}{\partial x_j} = P_u - \epsilon_u + \frac{\partial}{\partial x_j} \Big(\frac{\nu_t}{\sigma_k} \frac{\partial K_u}{\partial x_j} \Big) + (U_j - \overline{U_j}) \frac{\partial K_u}{\partial x_j} \tag{2.19}$$

The model equation for ϵ_u is developed in a similar fashion by requiring

$$\frac{d\epsilon_u}{dt} = f_\epsilon \frac{d\epsilon}{dt}. \tag{2.20}$$

This requirement implies

$$\frac{\partial \epsilon_u}{\partial t} + U_j \frac{\partial \epsilon_u}{\partial x_j} = f_\epsilon \Big[\frac{\partial \epsilon}{\partial t} + \overline{U_j} \frac{\partial \epsilon}{\partial x_j} \Big] + (U_j - \overline{U_j}) \frac{\partial \epsilon_u}{\partial x_j}$$

$$= f_\epsilon\Big[C_{\epsilon 1}\frac{P\epsilon}{K} - C_{\epsilon 2}\frac{\epsilon^2}{K} + \frac{\partial}{\partial x_j}\Big(\frac{\nu_t}{\sigma_\epsilon}\frac{\partial \epsilon}{\partial x_j}\Big)\Big] + (U_j - \overline{U_j})\frac{\partial \epsilon_u}{\partial x_j} \quad (2.21)$$

Here again, expressing all RANS variables in terms of their PANS counterparts we obtain the model equation for unresolved dissipation as

$$\begin{aligned}\frac{\partial \epsilon_u}{\partial t} + U_j\frac{\partial \epsilon_u}{\partial x_j} &= C_{\epsilon 1}\frac{P_u\epsilon_u}{K_u} - \Big(C_{\epsilon 1} + \frac{f_k}{f_\epsilon}(C_{\epsilon 2} - C_{\epsilon 1})\Big)\frac{\epsilon_u^2}{K_u} + \frac{\partial}{\partial x_j}\Big(\frac{\nu_t}{\sigma_\epsilon}\frac{\partial \epsilon_u}{\partial x_j}\Big) \\ &\quad + (U_j - \overline{U_j})\frac{\partial \epsilon_u}{\partial x_j} \qquad (2.22)\end{aligned}$$

Finally, the two equation PANS model can be summarized as follows:

$$\frac{\partial K_u}{\partial t} + U_j\frac{\partial K_u}{\partial x_j} = P_u - \epsilon_u + T_{k_u} \quad (2.23)$$

$$\frac{\partial \epsilon_u}{\partial t} + U_j\frac{\partial \epsilon_u}{\partial x_j} = C_{\epsilon 1}\frac{P_u\epsilon_u}{K_u} - C^*_{\epsilon 2}\frac{\epsilon_u^2}{K_u} + T_{\epsilon_u} \quad (2.24)$$

where

$$C^*_{\epsilon 2} = \Big(C_{\epsilon 1} + \frac{f_k}{f_\epsilon}(C_{\epsilon 2} - C_{\epsilon 1})\Big) \quad (2.25)$$

and $C_{\epsilon 1}$ and $C_{\epsilon 2}$ are the standard $K-\epsilon$ model constants. The two terms for transport of unresolved quantities T_{k_u} and T_{ϵ_u} are expressed as

$$T_{k_u} = \frac{\partial}{\partial x_j}\Big(\frac{\nu_t}{\sigma_k}\frac{\partial K_u}{\partial x_j}\Big) + (U_j - \overline{U_j})\frac{\partial K_u}{\partial x_j} \quad (2.26)$$

$$T_{\epsilon_u} = \frac{\partial}{\partial x_j}\Big(\frac{\nu_t}{\sigma_\epsilon}\frac{\partial \epsilon_u}{\partial x_j}\Big) + (U_j - \overline{U_j})\frac{\partial \epsilon_u}{\partial x_j} \quad (2.27)$$

The only terms that require further closure in the PANS model are these transport terms. Modeling these terms constitute an important objective of this thesis.

CHAPTER III

TURBULENT TRANSPORT MODELS

The equations for T_{k_u} and T_{ϵ_u} can be written wholly in terms of PANS variables by expressing the ratio of total viscosity to turbulent Prandtl numbers as

$$\begin{aligned} T_{k_u} &= \frac{\partial}{\partial x_j}\Big(\frac{\nu_t}{\sigma_k}\frac{\partial K_u}{\partial x_j}\Big) + (U_j - \overline{U_j})\frac{\partial K_u}{\partial x_j} \\ &= \frac{\partial}{\partial x_j}\Big(\frac{\nu_u f_\epsilon}{\sigma_k f_k^2}\frac{\partial K_u}{\partial x_j}\Big) + (\overline{U_j} - U_j) \end{aligned} \tag{3.1}$$

$$\begin{aligned} T_{\epsilon_u} &= \frac{\partial}{\partial x_j}\Big(\frac{\nu_t}{\sigma_\epsilon}\frac{\partial \epsilon_u}{\partial x_j}\Big) + (U_j - \overline{U_j})\frac{\partial \epsilon_u}{\partial x_j} \\ &= \frac{\partial}{\partial x_j}\Big(\frac{\nu_u f_\epsilon}{\sigma_\epsilon f_k^2}\frac{\partial \epsilon_u}{\partial x_j}\Big) + (\overline{U_j} - U_j) \end{aligned} \tag{3.2}$$

In the PANS equations, the unclosed terms that require modeling are the **convection of K_u, ϵ_u by resolved fluctuations** $(\overline{U_j} - U_j)$. In order to close these transport terms completely, we examine two extremes or limits.

Zero-Transport assumption: This assumption is based on the hypothesis that the *resolved fluctuations* $(\overline{U_j} - U_j)$ *do not take part in the net transport of unresolved kinetic energy* (K_u) at the scales of resolution in which we are interested (see Fig 3.). That is, we hypothesize that

$$K_u(x - \frac{dx}{2}) = K_u(x + \frac{dx}{2}) \tag{3.3}$$

$$\epsilon_u(x - \frac{dx}{2}) = \epsilon_u(x + \frac{dx}{2}) \tag{3.4}$$

where $dx \approx l_i$–inertial scales of motion. If our hypothesis is true then we will have $\frac{\partial K_u}{\partial x} = 0; \frac{\partial \epsilon_u}{\partial x} = 0.$ leading to,

$$T_{k_u} = \frac{\partial}{\partial x_j}\Big(\frac{\nu_u f_\epsilon}{\sigma_k f_k^2}\frac{\partial K_u}{\partial x_j}\Big) \tag{3.5}$$

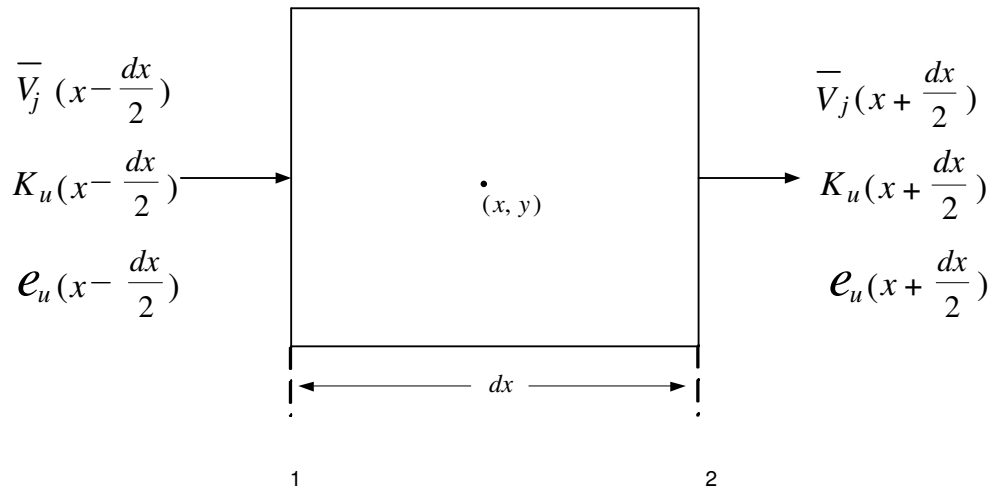

Fig. 3. Control volume showing flux of K_u and ϵ_u

$$T_{\epsilon_u} = \frac{\partial}{\partial x_j}\left(\frac{\nu_u f_\epsilon}{\sigma_\epsilon f_k^2}\frac{\partial \epsilon_u}{\partial x_j}\right) \tag{3.6}$$

which is finally written as

$$T_{k_u} = \frac{\partial}{\partial x_j}\left(\frac{\nu_u}{\sigma_{k_u}}\frac{\partial K_u}{\partial x_j}\right) \tag{3.7}$$

$$T_{\epsilon_u} = \frac{\partial}{\partial x_j}\left(\frac{\nu_u}{\sigma_{\epsilon_u}}\frac{\partial \epsilon_u}{\partial x_j}\right) \tag{3.8}$$

with the unresolved Prandtl numbers expressed as

$$\sigma_{k_u} = \frac{f_k^2}{f_\epsilon}\sigma_k \tag{3.9}$$

$$\sigma_{\epsilon_u} = \frac{f_k^2}{f_\epsilon}\sigma_\epsilon \tag{3.10}$$

Maximum-Transport Model: The second case is based on a more generalized gradient-transport closure and states that *the resolved field velocity is proportional to*

the resolved field eddy viscosity ν_r, which can be defined as

$$\nu_r = \nu_t - \nu_u = C_\mu \frac{K^2}{\epsilon} - C_\mu \frac{K_u^2}{\epsilon_u} \tag{3.11}$$

Thus,

$$(\overline{U_j} - U_j)\frac{\partial K_u}{\partial x_j} = \frac{\partial}{\partial x_j}\Big(\frac{\nu_r}{\sigma_k}\frac{\partial K_u}{\partial x_j}\Big) = \frac{\partial}{\partial x_j}\Big(\frac{(\nu_t - \nu_u)}{\sigma_k}\frac{\partial K_u}{\partial x_j}\Big) \tag{3.12}$$

$$(\overline{U_j} - U_j)\frac{\partial \epsilon_u}{\partial x_j} = \frac{\partial}{\partial x_j}\Big(\frac{\nu_r}{\sigma_\epsilon}\frac{\partial \epsilon_u}{\partial x_j}\Big) = \frac{\partial}{\partial x_j}\Big(\frac{(\nu_t - \nu_u)}{\sigma_\epsilon}\frac{\partial \epsilon_u}{\partial x_j}\Big) \tag{3.13}$$

For this case from equations (3.1) and (3.2), we get

$$\begin{aligned}(T_{k_u}, T_{\epsilon_u}) &= \frac{\partial}{\partial x_j}\Big(\frac{\nu_t}{(\sigma_k, \sigma_\epsilon)}\frac{\partial (K_u, \epsilon_u)}{\partial x_j}\Big) - \frac{\partial}{\partial x_j}\Big(\frac{(\nu_t - \nu_u)}{(\sigma_k, \sigma_\epsilon)}\frac{\partial (K_u, \epsilon_u)}{\partial x_j}\Big) \\ &= \frac{\partial}{\partial x_j}\Big(\frac{\nu_u}{(\sigma_k, \sigma_\epsilon)}\frac{\partial (K_u, \epsilon_u)}{\partial x_j}\Big)\end{aligned} \tag{3.14}$$

and finally

$$T_{k_u} = \frac{\partial}{\partial x_j}\Big(\frac{\nu_u}{\sigma_{k_u}}\frac{\partial K_u}{\partial x_j}\Big) \quad \text{and} \tag{3.15}$$

$$T_{\epsilon_u} = \frac{\partial}{\partial x_j}\Big(\frac{\nu_u}{\sigma_{\epsilon_u}}\frac{\partial \epsilon_u}{\partial x_j}\Big) \tag{3.16}$$

with the modified Prandtl numbers for unresolved kinetic energy and dissipation as

$$\sigma_{k_u} = \sigma_k \tag{3.17}$$

$$\sigma_{\epsilon_u} = \sigma_\epsilon \tag{3.18}$$

Now we will consider the physical implications of the two model. If we consider a continuum (Fig.1) whose width (dx) corresponds to an order of length equal to the intermediate scales of motion, then the net flux of K_u (or $\epsilon_u(e_u)$) between regions 1 and 2 of the continuum is given by

$$\overline{V_j}(x_j + \frac{dx_j}{2})K_u(x_j + \frac{dx_j}{2}) - \overline{V_j}(x_j - \frac{dx_j}{2})K_u(x_j - \frac{dx_j}{2}) \tag{3.19}$$

$$V_j\Big[\frac{\partial K_u}{\partial x_j} + K_u\frac{\partial V_j}{\partial x_j}\Big]d\underline{x} = V_j\frac{\partial K_u}{\partial x_j} \quad \text{invoking the continuity equation} \tag{3.20}$$

Now since ϵ_u is a small-scale quantity and consequently its statistics converge to a mean value quickly, for a given width of the continuum, it is reasonable to assume that its mean changes slowly between regions 1 and 2, and hence its gradient (or transport) is negligibly small in the region of interest.i.e.

$$\frac{\partial \epsilon_u}{\partial x_j} \approx 0 \tag{3.21}$$

Thus, in equation (3.4) the only remaining term is the viscous transport term

$$T_{\epsilon_u} = \frac{\partial}{\partial x_j}\Big(\frac{\nu_t}{\sigma_\epsilon}\frac{\partial \epsilon_u}{\partial x_j}\Big) \tag{3.22}$$

where the ratio of the total viscosity (ν_t) to the dissipation Prandtl number (σ_ϵ) can be written as

$$\frac{\nu_t}{\sigma_\epsilon} = \frac{C_\mu\frac{K^2}{\epsilon}}{\sigma_\epsilon} = \frac{C_\mu\frac{K_u^2}{\epsilon_u}}{\sigma_\epsilon\frac{f_k^2}{f_\epsilon}} = \frac{\nu_u}{\sigma_{\epsilon_u}} \tag{3.23}$$

which is essentially the **Zero-Transport** model for unresolved dissipation ϵ_u.

In the equation for K_u however, transport terms due to both viscosity and resolved fluctuations exist, as K_u is a large scale quantity whose mean changes considerably between regions 1 and 2 and therefore its gradient is significant in the region of interest, and thus cannot be neglected. Hence, in this case we have

$$T_{k_u} = \frac{\partial}{\partial x_j}\Big(\frac{\nu_t}{\sigma_k}\frac{\partial K_u}{\partial x_j}\Big) - (\overline{U_j} - U_j)\frac{\partial K_u}{\partial x_j} \tag{3.24}$$

and therefore make use of the second assumption based on gradient-transport closure and obtain

$$T_{k_u} \;=\; \frac{\partial}{\partial x_j}\Big(\frac{\nu_t}{\sigma_k}\frac{\partial K_u}{\partial x_j}\Big) - \frac{\partial}{\partial x_j}\Big(\frac{(\nu_t - \nu_u)}{\sigma_k}\frac{\partial K_u}{\partial x_j}\Big)$$

$$= \frac{\partial}{\partial x_j}\left(\frac{\nu_u}{\sigma_k}\frac{\partial K_u}{\partial x_j}\right) \tag{3.25}$$

which is the **Maximum-Transport** model for unresolved kinetic energy, K_u. This appears to indicate that the ZT model is better suited for modeling unresolved dissipation (ϵ_u), while the MT model is adequate for unresolved kinetic energy (K_u).

The objective of the current study is to determine which of these two transport models performs better for K_u and ϵ_u.

CHAPTER IV

PROBLEM SET-UP AND DETAILS OF THE FLUENT FLOW SOLVER

A. Problem Formulation Using FLUENT Flow Solver

FLUENT [28] is a computer program for modeling fluid flow and heat transfer in complex geometries. It is capable of solving flow problems with unstructured (as well as structured) meshes that can be generated about complex geometries with ease. A variety of mesh types are supported by **FLUENT** [28], which include 2D triangular/quadrilateral, 3D tetrahedral/hexahedral/pyramid/wedge, and mixed (hybrid) meshes. An important feature that **FLUENT** possesses is that it allows refinement or coarsening of the grid depending on the flow solution and this feature is extremely useful for accurately predicting flow fields in regions with large gradients, such as free shear layers and boundary layers. The time required to generate a grid is significantly reduced and grid refinement studies can be performed with ease. The computational effort is also reduced, as mesh refinement is limited to those regions where greater mesh resolution is needed.

Some of **FLUENT**'s [28] modeling capabilities include flows in 2D or 3D geometries using unstructured, structured or mixed (hybrid) grids, incompressible/compressible flows, inviscid , laminar, or turbulent flows, modeling heat transfer, chemical species mixing etc. The initial mesh for **FLUENT** is generated outside the solver, by employing a grid generation software such as **GAMBIT**. **FLUENT** [28] essentially provides the following three solver formulations: segregated, coupled implicit and coupled explicit. The segregated and the coupled solvers differ in the way they solve the continuity, momentum, and (where appropriate) energy and species equations. The segregated solver solves these equations sequentially, while the coupled solver

solves them simultaneously. The segregated solver is intended for incompressible and mildly compressible flows while the coupled approach is used for high-speed compressible flows. In the present analysis of lid-driven cavity flows, since we have assumed the flow to be incompressible, the segregated solver has been used to solve the system of equations.

The steps involved in setting up the **FLUENT** flow solver for solving the lid-driven cavity flow problem are briefly discussed below. First, the appropriate mesh file is read and following that the solver formulation is selected : segregated solver, unsteady formulation, second-order accurate, implicit discretization scheme. Next, the required turbulence equations ($K-\epsilon$ model) to be solved are selected and the material properties such as density (ρ), viscosity (μ) based on Reynolds No(=10,000), and lid-speed ($U = 1.0m/s$) are set. The appropriate boundary and operating conditions along with the solution control parameters such as Pressure-Velocity coupling method, pressure interpolation schemes, etc. are selected. This is followed by initialization of the entire flow field, which involves prescribing initial values to variables such as velocity, pressure, kinetic energy, dissipation, etc. Calculations are then started and the solution is checked for convergence. It is important to note that the **FLUENT** solver is typically intended for RANS. However, PANS calculations are effected by suitably changing the values of the model co-efficient $C_{\epsilon 2}$ as $\left(C_{\epsilon 1} + \frac{f_k}{f_\epsilon}(C_{\epsilon 2} - C_{\epsilon 1})\right)$ and Prandtl numbers σ_k and σ_ϵ, based on either transport modeling assumption for a given f_k in the solver formulation menu as per the definitions in the previous sections.

B. Computational Domain

The cavity geometry is modelled for three different spanwise aspect ratios (SAR) of 3:1:1, 0.5:1:1 and 1:1:1, although the majority of the simulations for which qualitative

as well as quantitative data are available for comparison (Jordan, 1994 [16]), have been performed on an SAR of 3:1:1 (see Fig.4). For the above cases, the width(W) and the height(H) are taken to be 1.0, in both x and y directions. For the SAR corresponding to 3:1:1, the span(L) is taken to be 1.5 in the z-direction, while for the other two cases, values of 0.75 (SAR=0.5:1:1) and 1 (SAR=1:1:1) are employed. One boundary of the span (L) corresponding to SAR's of 3:1:1 and 0.5:1:1 is modelled as the plane of symmetry (z=0.0) and the other end as a solid end-wall. The lid (top wall) has been prescribed with a velocity(U) of 1 m/s in the horizontal direction. No-slip conditions have been enforced along all boundaries except at the mid-span plane which is treated numerically as a plane of symmetry as mentioned earlier. Simulations have been performed for a Reynolds number of 10,000. Sampling for unsteady statistics is not enabled until ten cycles (corresponding to 60 seconds of flow time) are completed. Quantitative comparisons are available in terms of Centerline mean velocity profiles for the z=0.28 plane, while qualitative comparisons are available in the form of X-vorticity contours. The grid sizes used for the various SAR(s) based on the f_k values and the cavity geometry for an SAR of 3:1:1 are shown in table I.

Table I. Grid Sizes for Various f_k Calculations

	f_k	Grid size
1	0.2	95*95*95
2	0.4	81*81*81
3	0.5	75*75*75
4	0.7	64*64*64
5	1.0	51*51*51

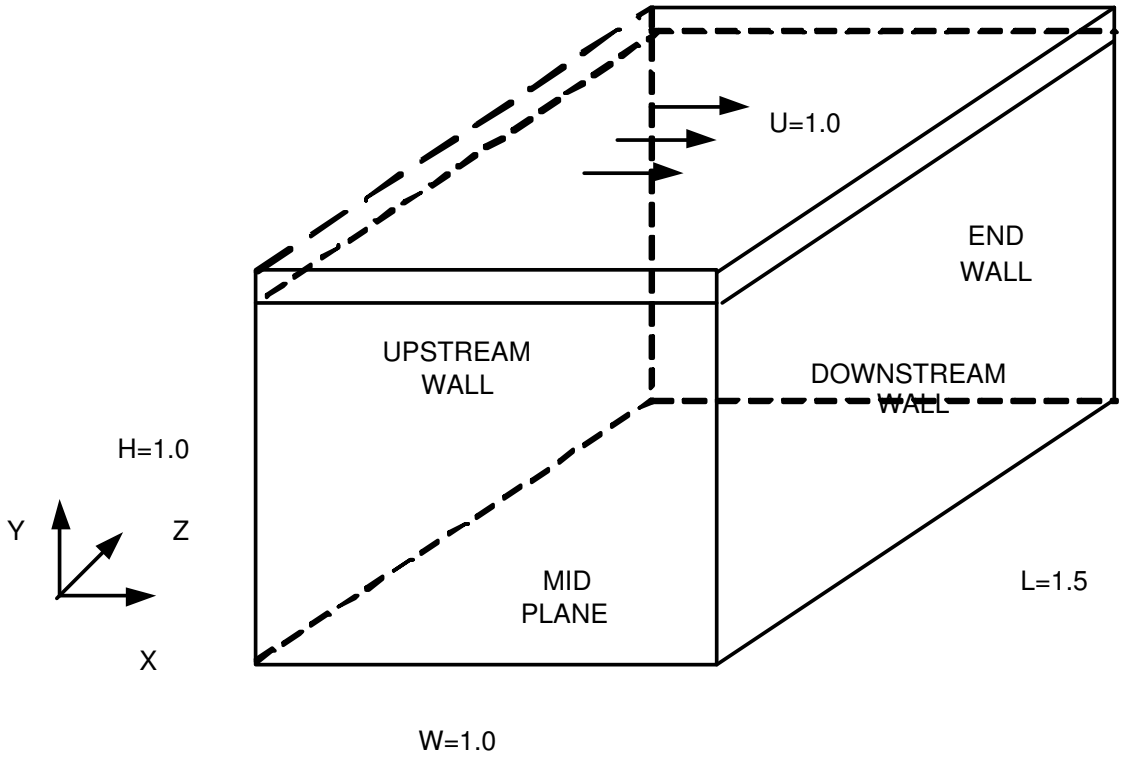

Fig. 4. The three-dimensional lid-driven cavity setup for SAR = 3:1:1

CHAPTER V

RESULTS AND DISCUSSION

In this section, the unsteady and turbulent flow results from numerical simulations of the three-dimensional lid-driven cavity flow are presented and compared with published experimental observations and LES results(Jordan, 1994 [16]). The results are presented in two sections. In the first, a comparison is made between simulations that are conducted using the Maximum-Transport (MT) and the Zero-Transport (ZT) models to evaluate which of the two models performs better for K_u and ϵ_u. Both simulations have been performed using a uniform grid arrangement. In the second section, a comparison is made between simulations conducted using two different types of grid arrangements (i.e between uniform and clustered grids), while also employing the ZT model. Such a simulation is performed to evaluate the effect of grid sketching on the accuracy of the numerical solution.

A majority of the simulations have been performed for a spanwise aspect ratio of 3:1:1, a case for which qualitative as well as quantitative data are available for comparison. Results for other spanwise aspect ratios of 0.5:1:1 and 1:1:1 on clustered grids are included for a single value of $f_k = 0.5$. These are used to determine the effects that a reduction of SAR would have on the accuracy of PANS, and to compare these with results described in literature (Prasad et al,(1989) [19]). All results have been generated on completion of the flow simulation corresponding to a flow time (T) of approximately 115 seconds. The plots for statistical quantities along cavity centerlines have been generated such that for the first 10 cycles (corresponding to about 60 seconds of flow time), no sampling of data is done in order for the flow to become fully turbulent, after which data is sampled every 6.5 seconds.

1. Maximum-Transport Vs Zero-Transport Model

In this section, the results of numerical simulations performed for an SAR of 3:1:1, using both the MT and the ZT models, are compared with each other as well as against LES and experiment. Qualitative comparisons are available in terms of contours of X-vorticity, while quantitative comparisons with LES are realized through plots of Centerline Mean Velocities at a $z = 0.28$ plane. The experimental results are available at the symmetry plane ($z = 0.0$), since LES results on the the $z = 0.28$ plane appear to closely follow the experimental data and which essentially proves that the simulation results are not affected by spatial variations (i.e. location of the planes). Both sets of simulations have been performed on a uniform grid arrangement (UG).

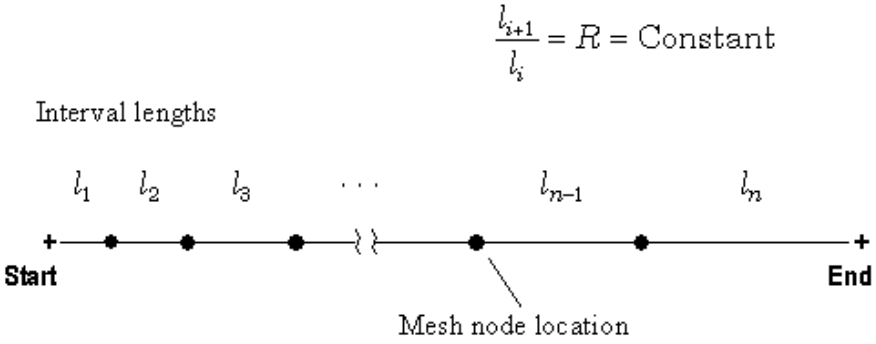

Fig. 5. Edge mesh grading parameters

Fig.5 shows a brief description of the grading scheme. Here l_{i+1} and l_i represent the lengths of the two succeeding intervals on any edge of the cavity and R is a fixed value. This scheme is known as the **Successive Ratio** grading scheme. Figures 6 and 7 show snapshots of the mean U and V velocity profiles along the cavity centerlines, while Fig. 8 presents contours of X-vorticity for a typical RANS (f_k=1) simulation. The plots illustrate the fact that RANS is inherently incapable of capturing many of the flow features and the plots for statistical quantities show its inability to produce LES-accurate results, especially near the boundaries of the cavity.

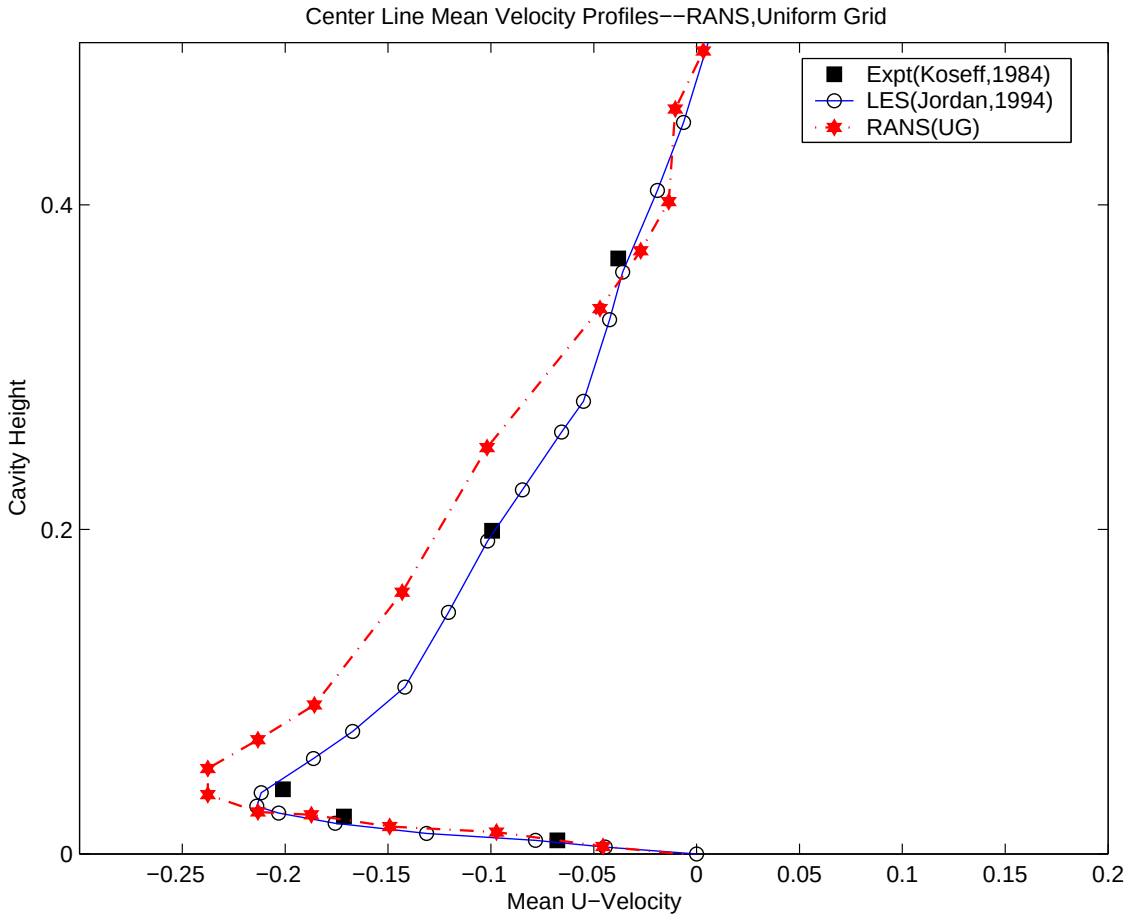

Fig. 6. Mean U-Velocity profiles, bottom wall closeup, (RANS, UG)

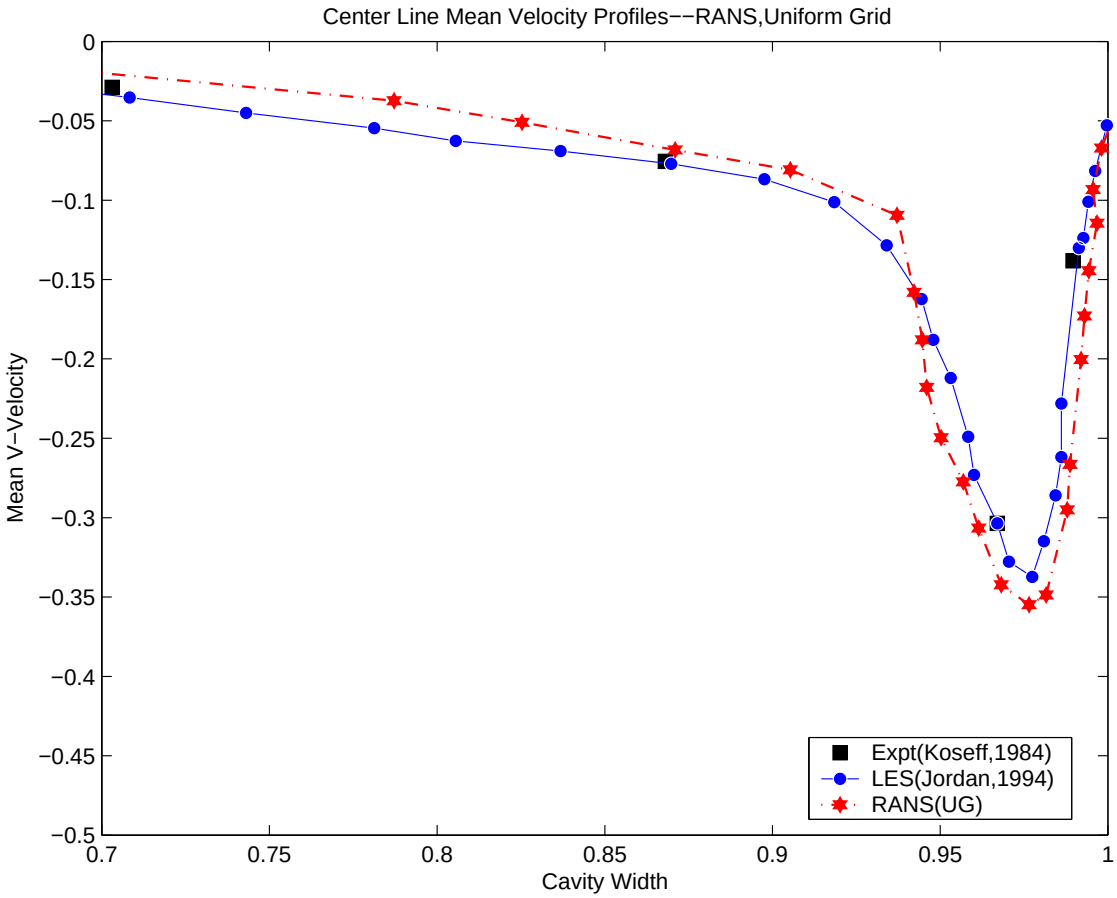

Fig. 7. Mean V-Velocity profiles, downstream wall closeup, (RANS, UG)

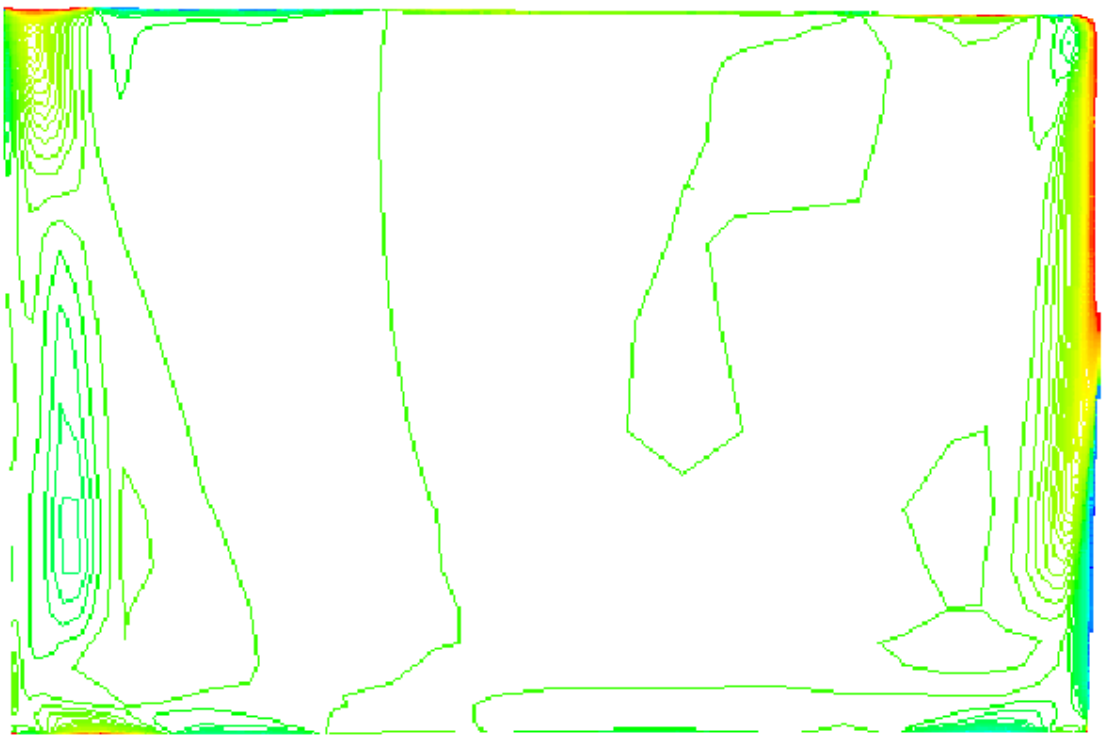

Fig. 8. X-Vorticity contours along downstream wall, (RANS, UG)

The next set of figures (9-24) show comparisons of the two turbulent transport models, ZT and MT, with each other as well as against LES and experiment. From the statistical comparisons for $f_k = 0.7$ (Figs. 9, 10), its is observed that (i) both models seem to be performing better than RANS and show greater convergence of the PANS calculations towards LES results; and (ii) the plots also illustrate the fact that the ZT model performs marginally better than the corresponding MT model near the cavity boundaries. Although marginally better accuracy is observed from the statistical comparisons, instantaneous X-Vorticity contours (Figs. 11 and 12) along the downstream wall display the fact that considerably more scales of flow are resolved by the ZT model when compared to the MT model, while both models are

able to uncover significantly more scales of flow than RANS, in terms of appearance of TGL vortex pairs. About three pairs of TGL vortices are observed for the ZT model (Fig. 11) while only one pair can be seen for the MT model (Fig. 12), for a value of f_k=0.7.

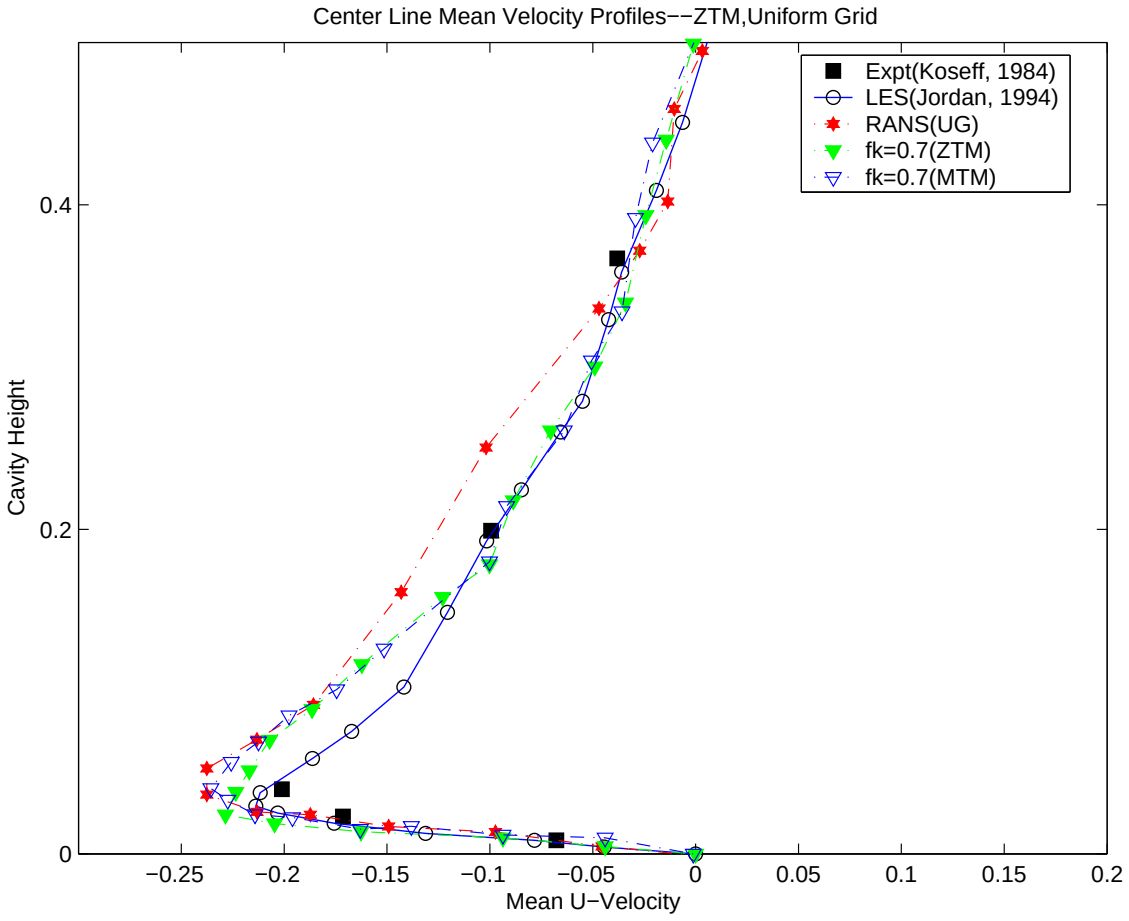

Fig. 9. Mean U-Velocity profiles, bottom wall closeup, $f_k = 0.7$, (ZT Vs MT)

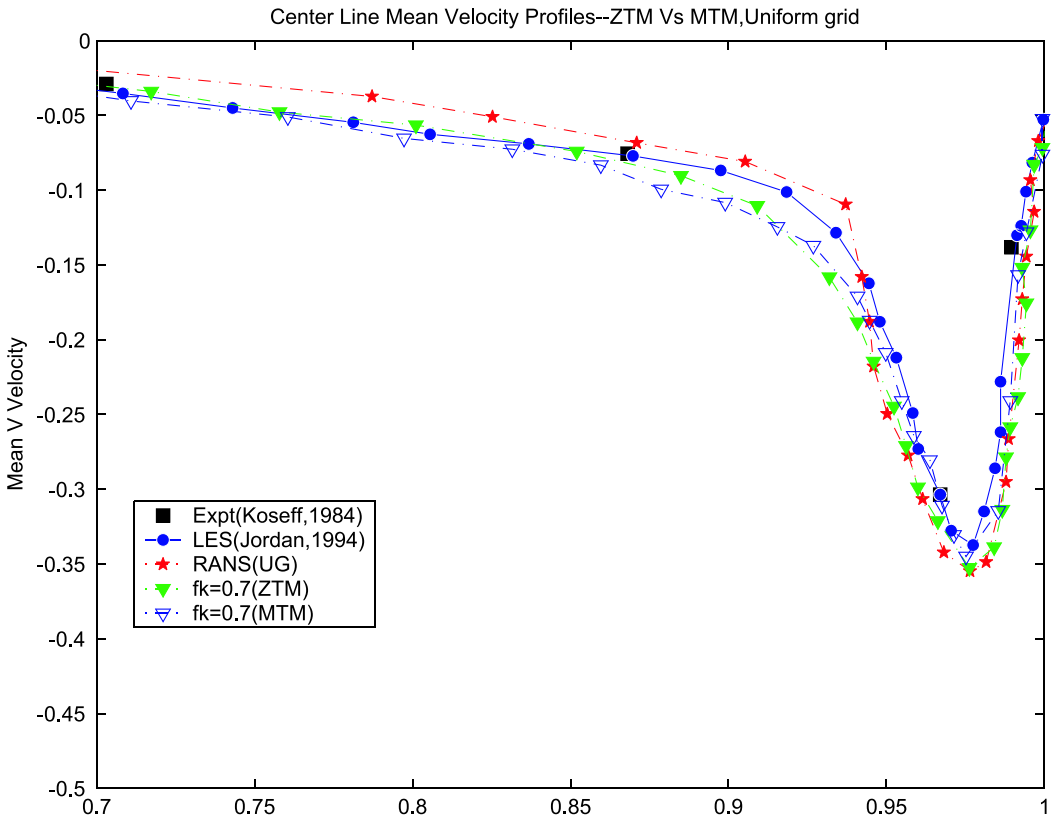

Fig. 10. Mean V-Velocity profiles, downstream wall closeup, $f_k = 0.7$, (ZT Vs MT)

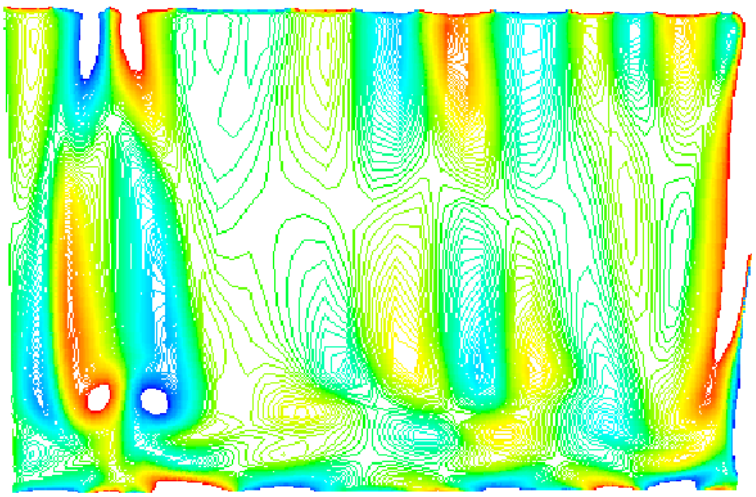

Fig. 11. X-Vorticity contours along downstream wall, $f_k = 0.7$, (ZT, UG)

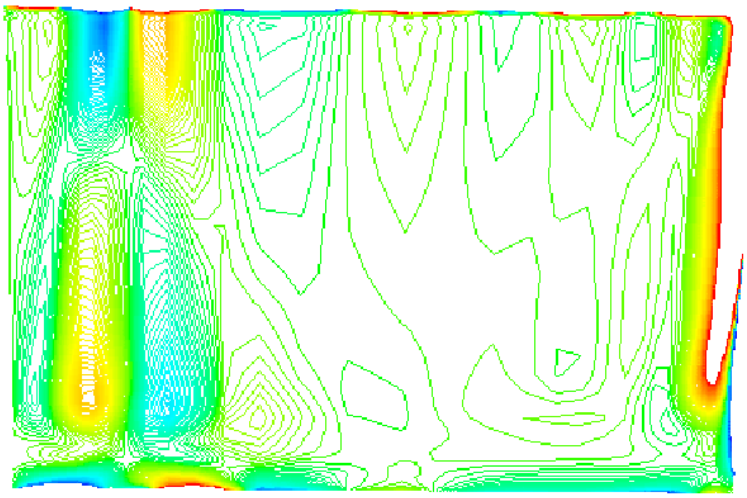

Fig. 12. X-Vorticity contours along downstream wall, $f_k = 0.7$, (MT, UG)

As the value of f_k is reduced, more and more vortices are uncovered and the number of flow features resolved by the ZT model is considerably more than the corresponding MT model for a given f_k. Specifically, 3(MT)-5(ZT) pairs are observed for f_k=0.4 (Figs. 15, 16). Statistical comparisons for the models indicate that although both models seem to perform fairly well along the center of the cavity, the ZT model appears to perform better than the MT model in the layers adjoining the upper and lower boundaries. Further, as the value of f_k is reduced, the ZT model shows closer agreement with LES and experiment than the corresponding MT model, for a given f_k. This trend can be seen in figures 13, 14 ($f_k = 0.4$).

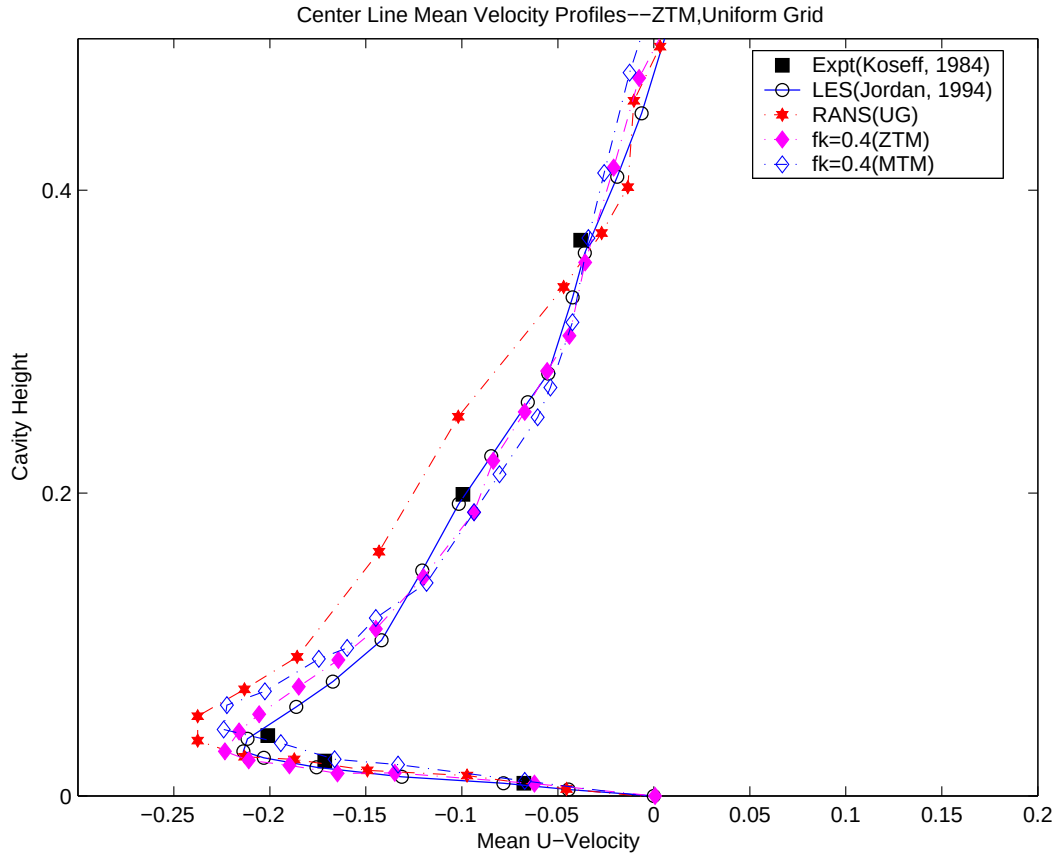

Fig. 13. Mean U-Velocity profiles, bottom wall closeup, $f_k = 0.4$, (ZT Vs MT)

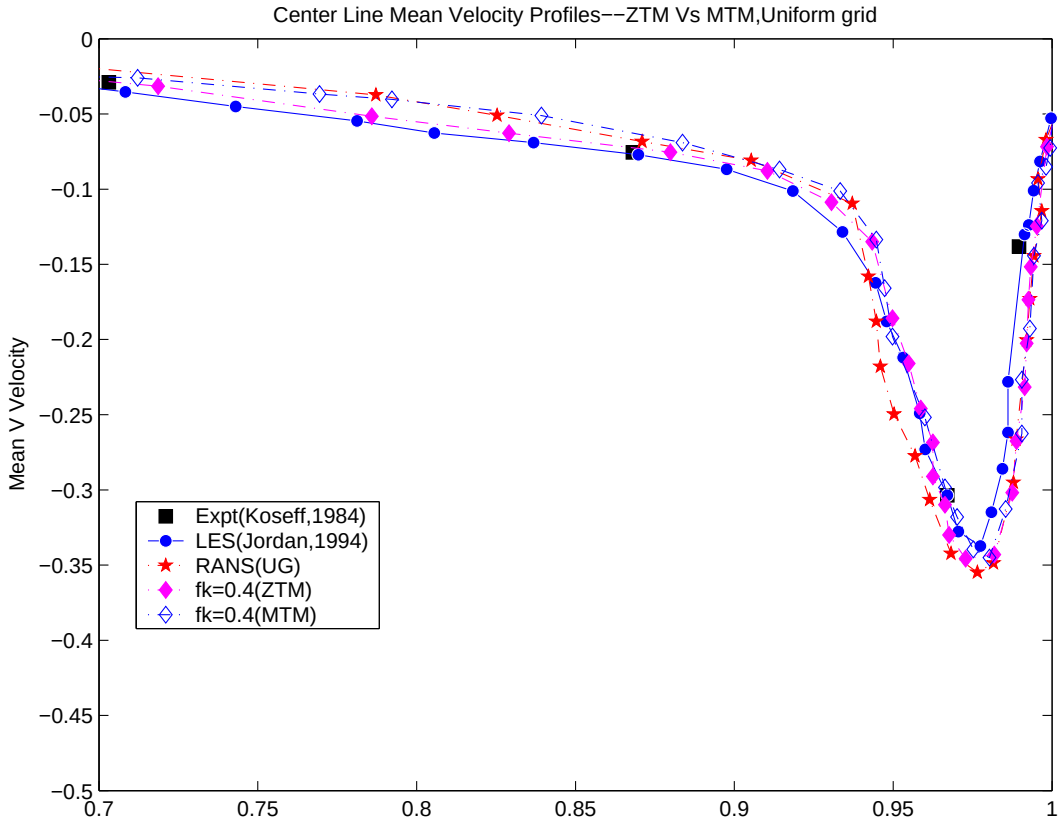

Fig. 14. Mean V-Velocity profiles, downstream wall closeup, $f_k = 0.4$, (ZT Vs MT)

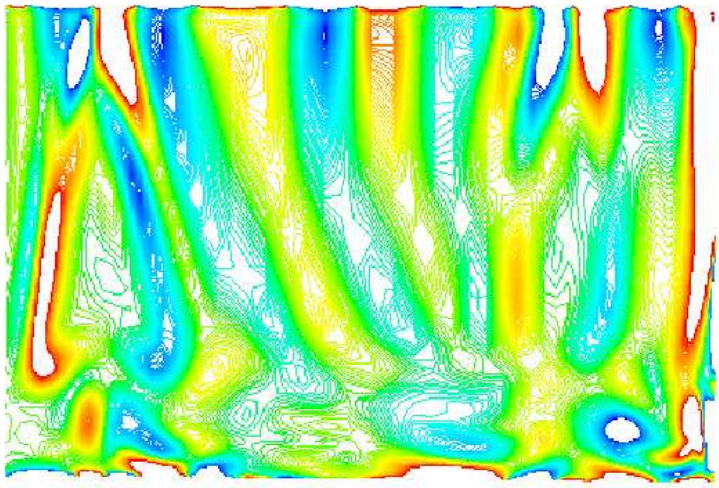

Fig. 15. X-Vorticity contours along downstream wall, $f_k = 0.4$, (ZT, UG)

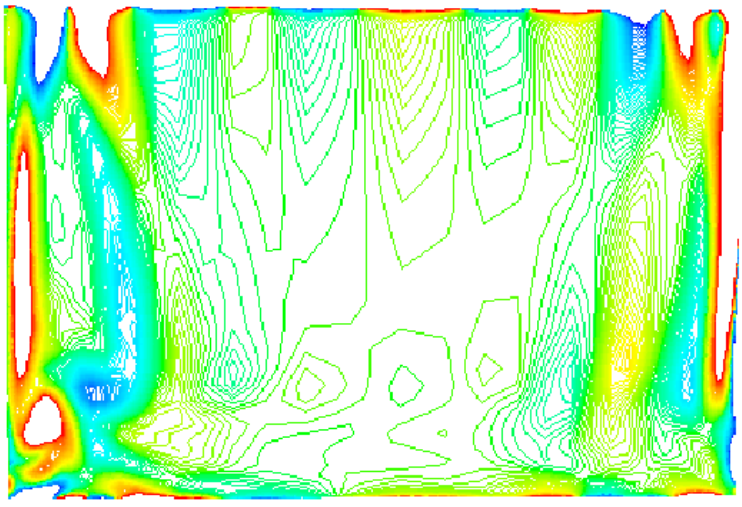

Fig. 16. X-Vorticity contours along downstream wall, $f_k = 0.4$, (MT, UG)

Figures 17-20 display results generated for $f_k = 0.2$. From these plots, it appears that results show near-LES accuracy in terms of realizations of mean quantities (Figs. 17, 18) and also maximum number of scales seem to be resolved : 4(MT)-6(ZT) pairs of TGL vortices (Figs. 19, 20).

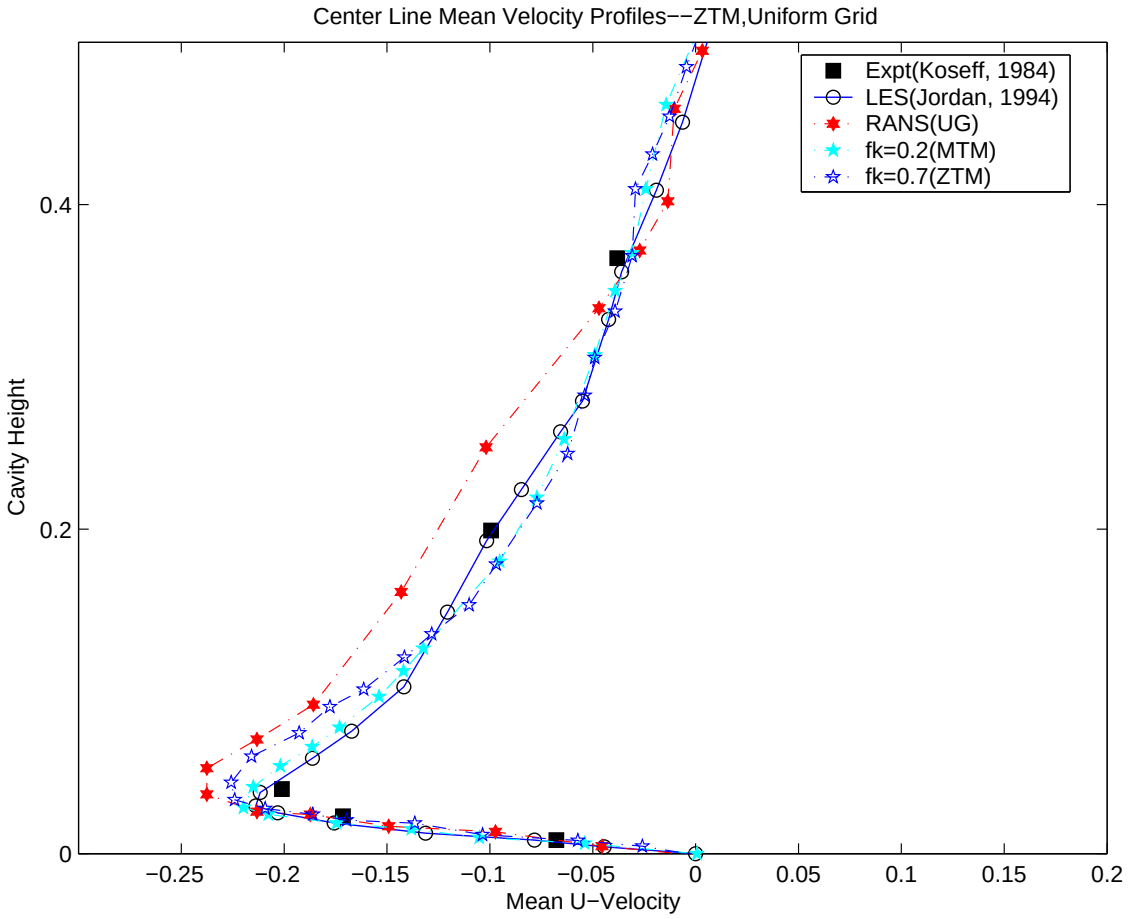

Fig. 17. Mean U-Velocity profiles, bottom wall closeup, $f_k = 0.2$, (ZT Vs MT)

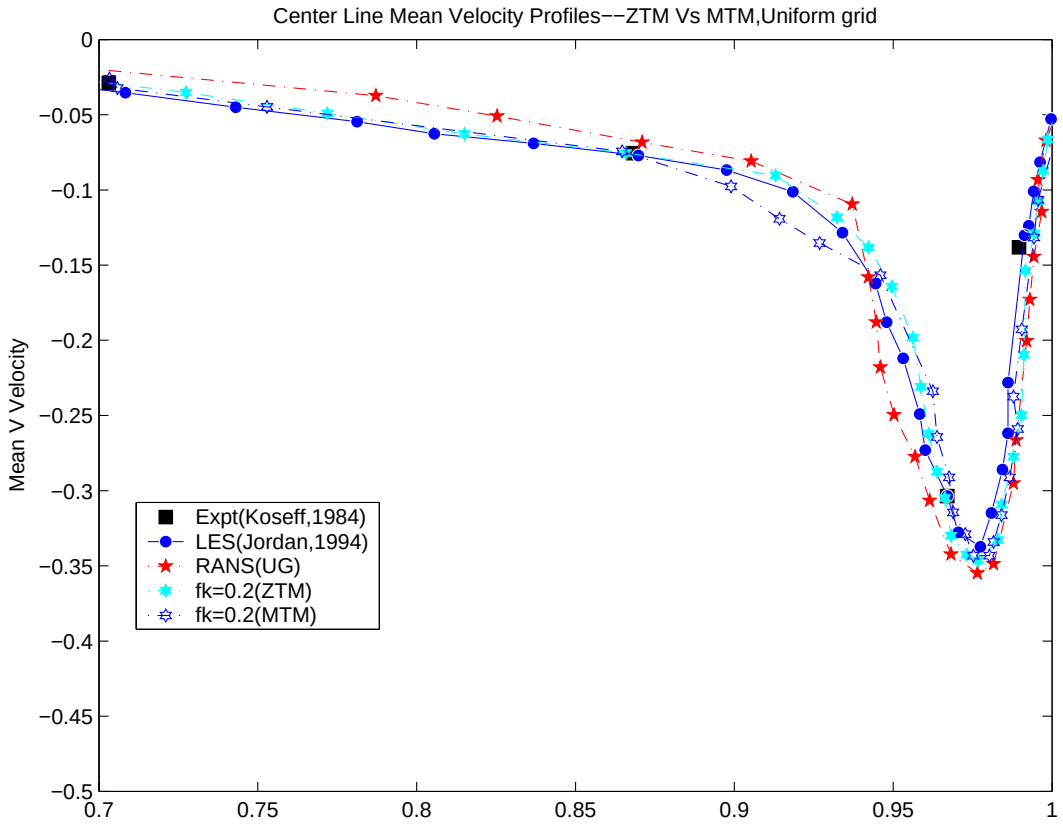

Fig. 18. Mean V-Velocity profiles, downstream wall closeup, $f_k = 0.2$, (ZT Vs MT)

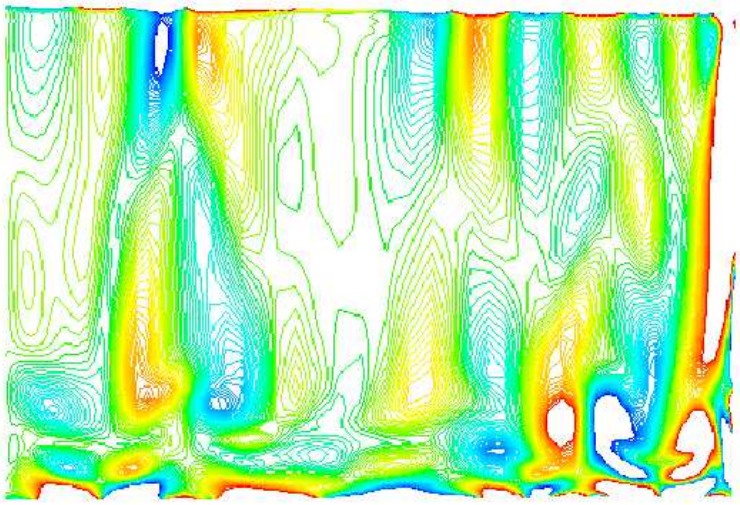

Fig. 19. X-Vorticity contours along downstream wall, $f_k = 0.2$, (ZT, UG)

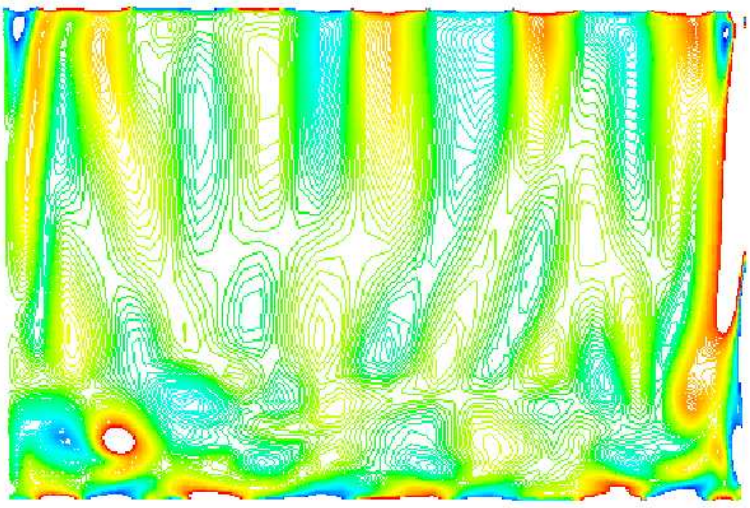

Fig. 20. X-Vorticity contours along downstream wall, $f_k = 0.2$, (MT, UG)

Since a majority of the disagreement is observed at the cavity boundaries, it seems necessary to refine the grid close to the wall, and this is discussed briefly in the next section. Finally, two important inferences that can be drawn from theses results are (i) the ZT model performs better than the corresponding MT model for a given f_k and (ii) as the value of f_k is decreased, better convergence towards LES and experiment is observed. The second inference is especially evident in figures 21-24. Figures 25-28 show a comparison between plots of contours of X-vorticity for various f_k values and essentially display the fact that a reduction in the value of f_k causes more and more scales to be resolved.

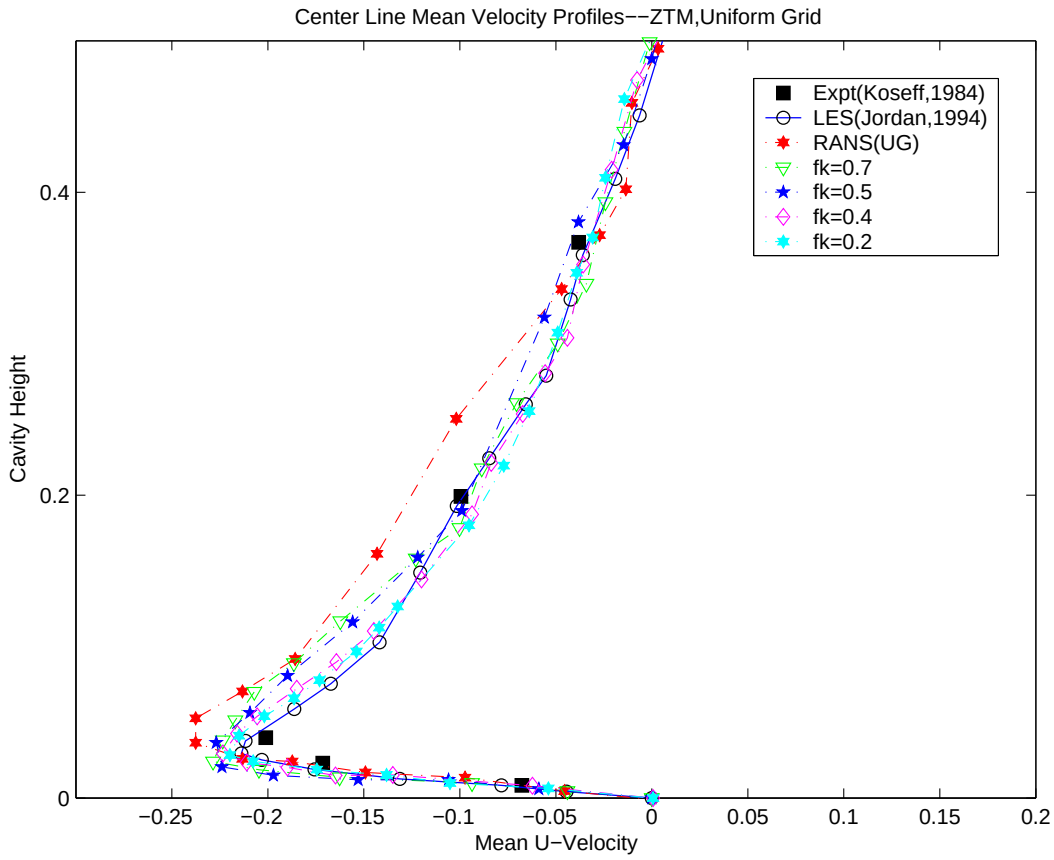

Fig. 21. Mean U-Velocity profiles, bottom wall closeup, (ZT, UG)

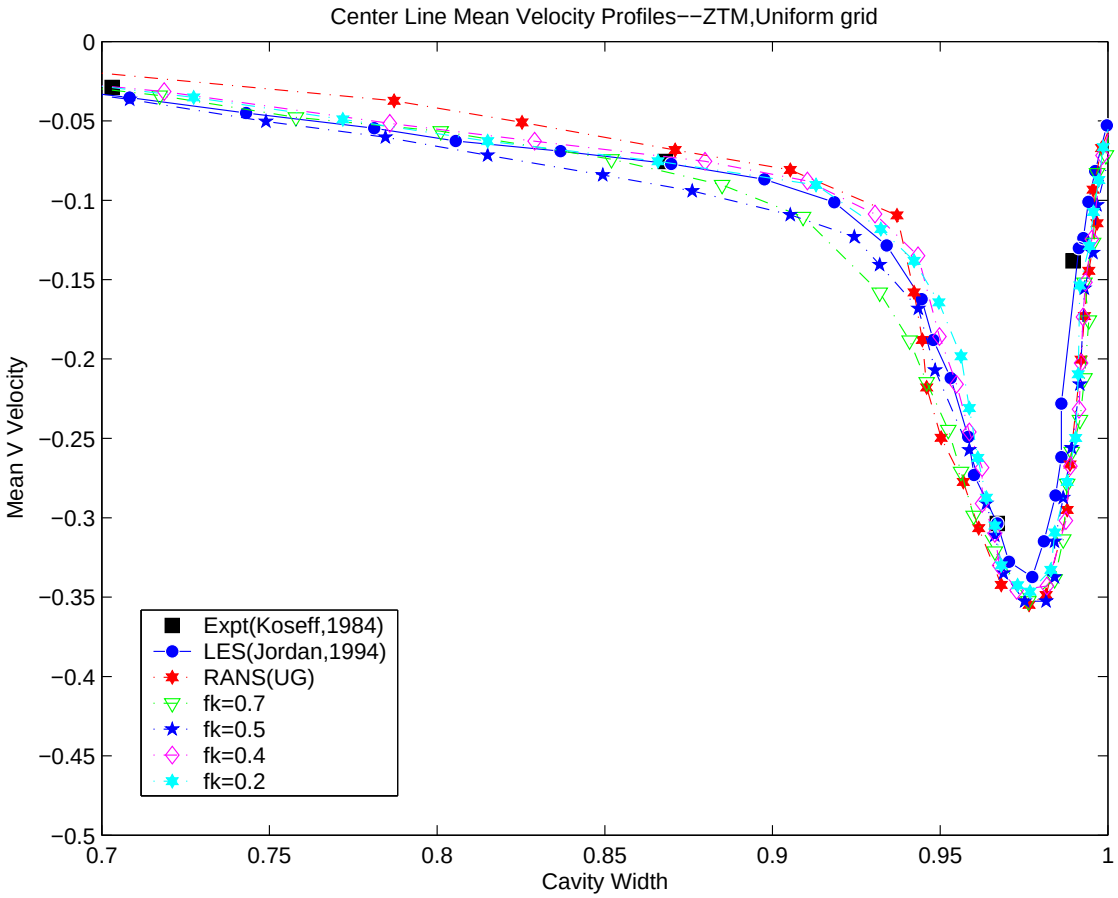

Fig. 22. Mean V-Velocity profiles, downstream wall closeup, (ZT, UG)

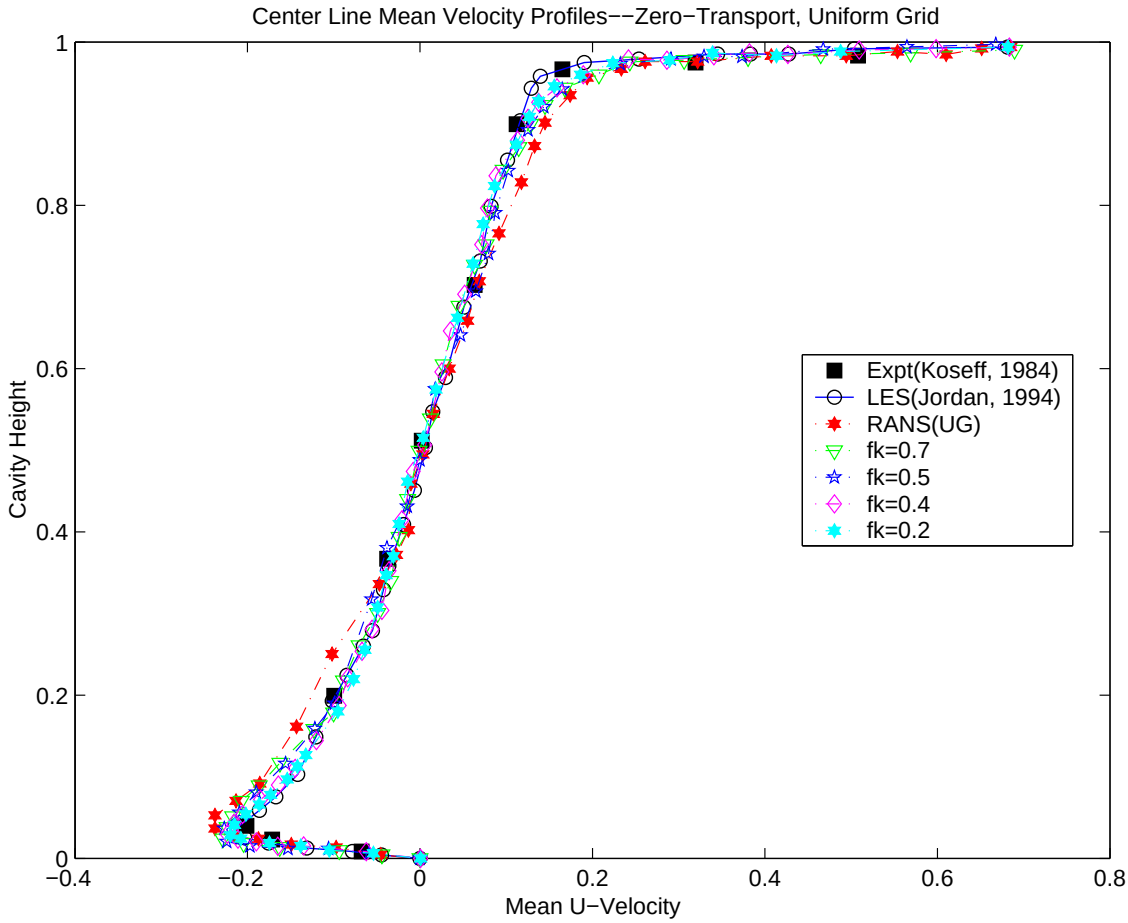

Fig. 23. Mean U-Velocity profiles, full cavity, (ZT, UG)

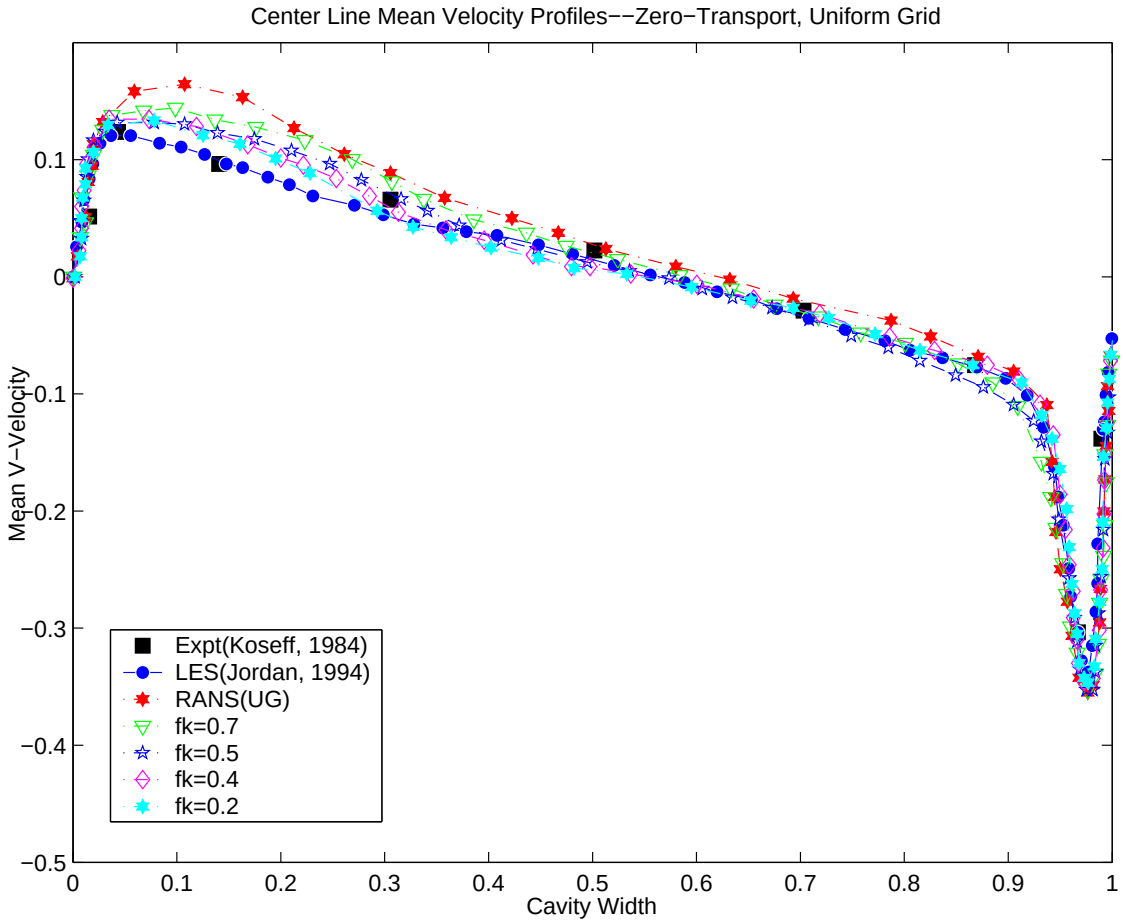

Fig. 24. Mean U-Velocity profiles, full cavity, (ZT, UG)

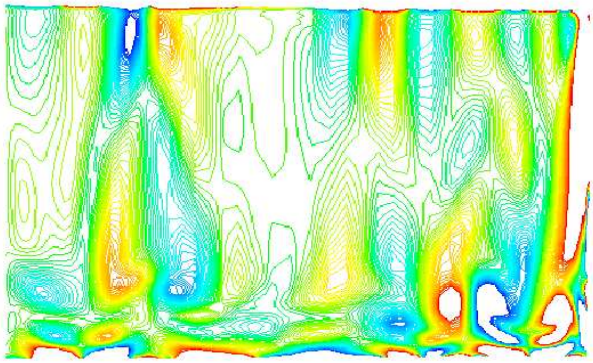

Fig. 25. X-Vorticity contours: $f_k = 0.2$

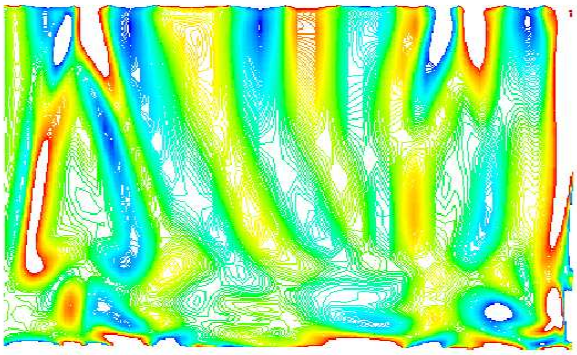

Fig. 26. X-Vorticity contours: $f_k = 0.4$

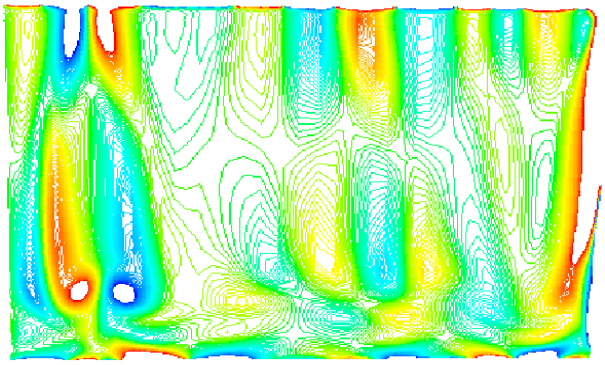

Fig. 27. X-Vorticity contours: $f_k = 0.7$

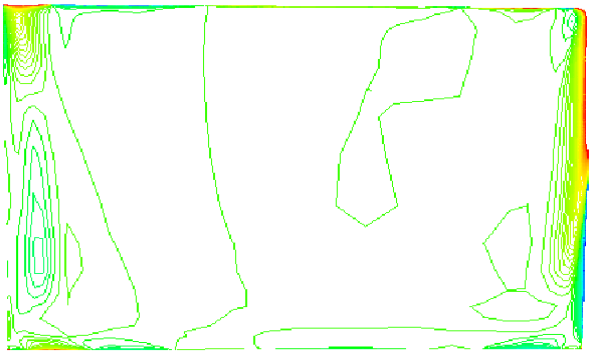

Fig. 28. X-Vorticity contours: RANS

All figures clearly display the effects of three-dimensionality on the basic recirculating flow features. For example, Figure 19 (f_k=0.2) shows the appearance of 6 pairs of TGL vortices which appear distorted due the onset of turbulence within the downstream free shear layer (Jordan, 1994 [16]). A DNS simulation performed on the cavity (SAR=3:1:1) at Re=5000 by Prasad et al (1988)[19], has reported the appearances of spiraling spanwise motions (see Fig.29) within the downstream secondary eddy (DSE), which is attributed to its interaction with the local vortices. A similar run has been performed at a corresponding Reynolds number(=5000) in which 4 pairs of TGL vortices are visible (see Fig.30), which is in accordance with results observed in the literature (Jordan, 1994 [16]).

As reported by Jordan, initially a few of the particles are convected by the primary recirculation vortex and as they near the cavity bottom, are entrained by the vortex rather than the DSE, while some of them are still entrained by the DSE. This complexity is owed to the fact that the large vortex induces a spanwise velocity component on the DSE, the particles thus trace out a broad spanwise spiral which quickly turns streamwise once fully entrained by the primary vortex. Hence it is concluded that the streamwise extent of the TGL vortices are sustained by the processes of fluid entrainment. Close to the downstream wall, these vortices entrain fluid from the adjacent DSE regions which in turn extract fluid from the primary recirculation vortex. Upstream of the DSE region however, the TGL vortices entrain the fluid directly from the primary vortex. Loss of the vortex structure occurs upstream once the primary vortex separates from the cavity bottom. Towards the end wall, another vortex pair is created which is due to opposing spanwise viscous interactions of the corner vortex, the adjacent TGL vortex and the no-slip condition along the cavity bottom. This secondary vortex is not stationary which is owed to the fact that the adjacent TGL vortices change in size and meander along the spanwise plane.

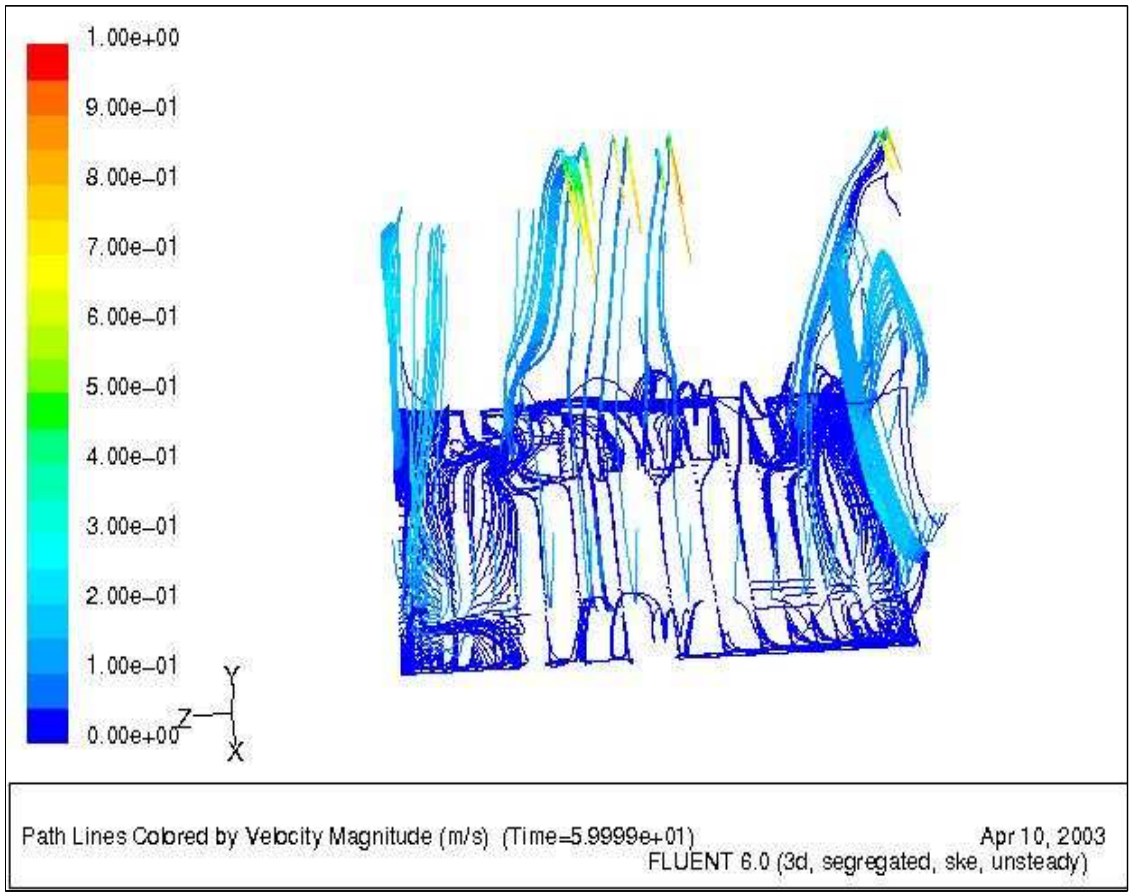

Fig. 29. Spiralling spanwise motions due to interactions among the primary recirculation vortex, downstream secondary eddy, TGL vortex and corner vortices

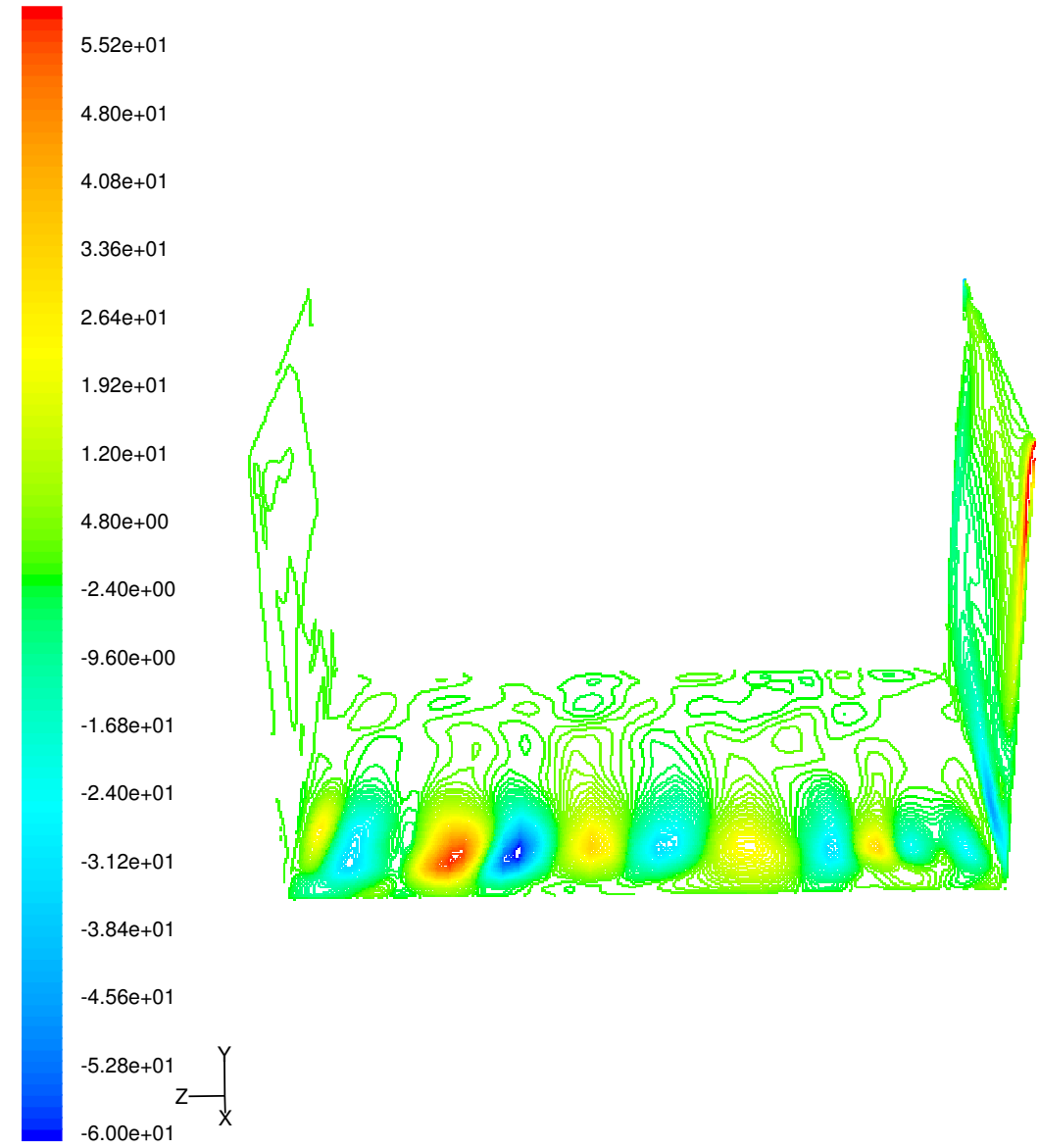

Fig. 30. Spanwise distribution and streamwise extent of the TGL vortex contours

Table II. Grid Sizes and Grading Schemes for Clustered Grid

	f_k	Grid size	Grading Scheme Ratio(R)	y(meters)
1	0.2	95*95*95	1.10	1.7114e-4
2	0.4	81*81*81	1.11	2.3460e-4
3	0.5	75*75*75	1.115	3.2750e-4
4	0.7	64*64*64	1.117	3.2937e-4
5	1.0	51*51*51	1.125	3.0846e-4

2. Clustered Grid Vs Uniform Grid

In order to reduce the error near the boundaries obtained by the simulations that were performed in the previous section using the uniform grid (UG), a clustered grid (CG) arrangement is employed. The main difference between the two grid arrangements is found in the way the grid points are spaced along the cavity boundaries. Moreover, the grid sizes that are used are identical to the ones used in the uniform grid, but the points are clustered more closely to the wall. The clustered grid for the various f_k values and their grading scheme is listed in the table II. The y^+ values for the various grid sizes lie between 12 and 30.

All simulations have been performed using the ZT model. Figures 31 and 32 show mean U and V velocity profiles for a typical RANS simulation (f_k=1.0), performed using both grids. As evident from the plots, the CG arrangement seems to give better agreement with LES than the corresponding UG arangement. Also, marginally more scales of flow appear to be resolved by using the CG arrangement, when instantaneous X-vorticity contour plots (Figs. 33 and 34) are compared for both grids.

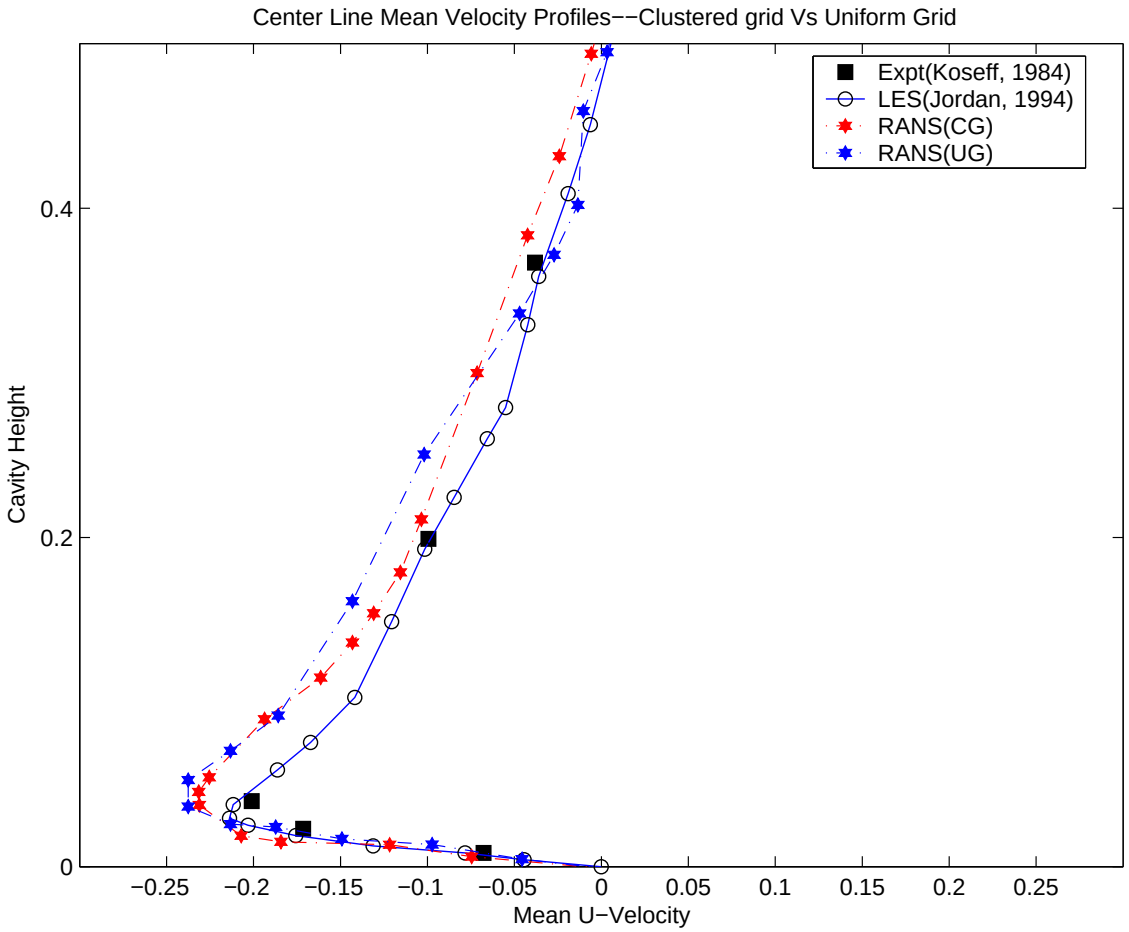

Fig. 31. Mean U-Velocity profiles, bottom wall closeup, (RANS, CG Vs UG)

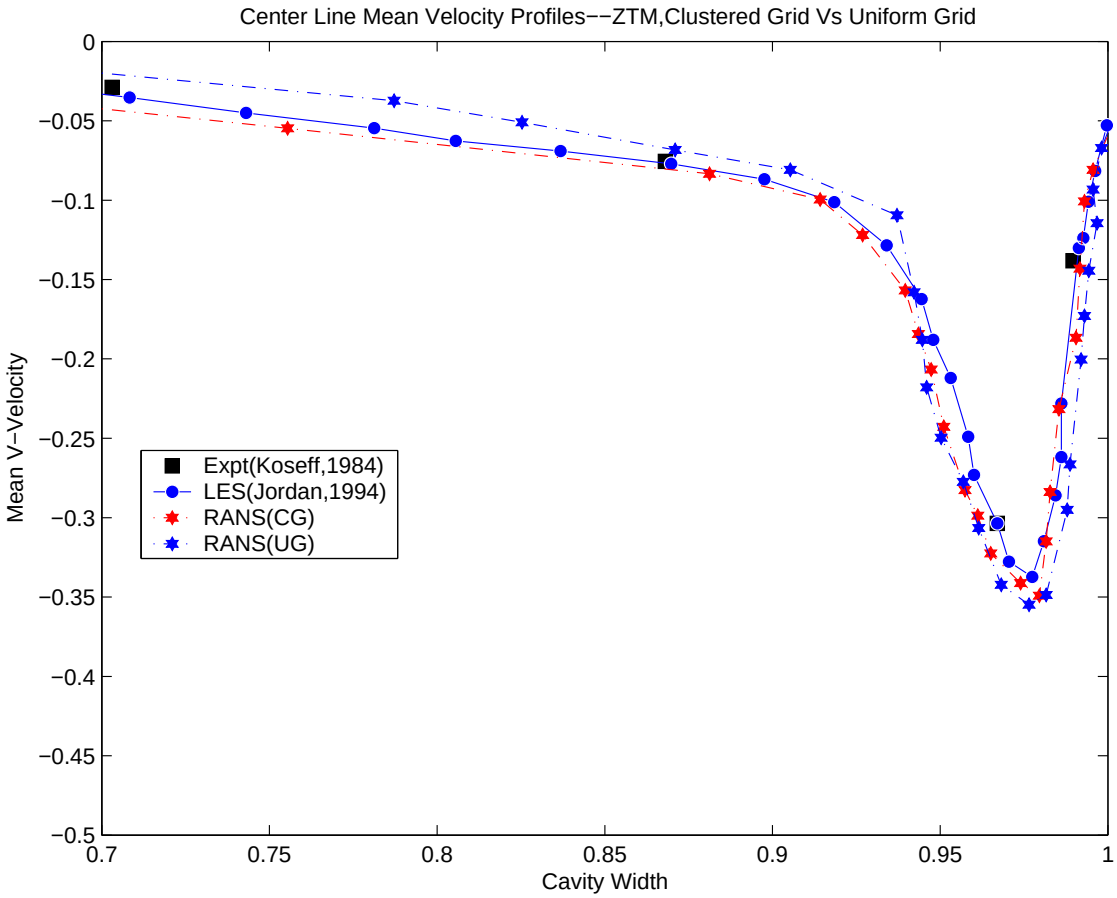

Fig. 32. Mean V-Velocity profiles, downstream wall closeup, (RANS, CG Vs UG)

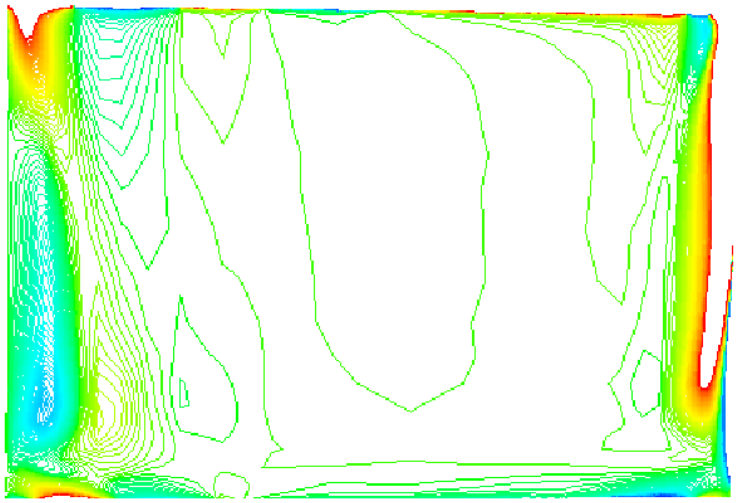

Fig. 33. X-Vorticity contours along downstream wall, (RANS, CG)

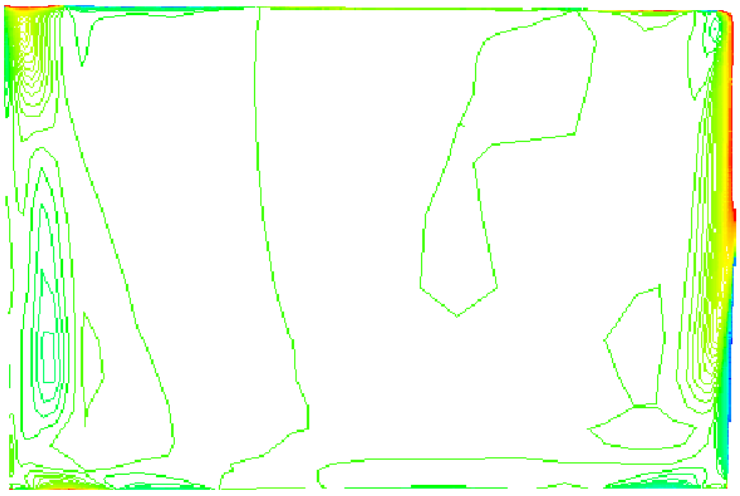

Fig. 34. X-Vorticity contours along downstream wall, (RANS, UG)

Figures 35 and 36 show mean velocity profiles for a value of $f_k = 0.7$, generated using either grid arrangement. Two important inferences that can be drawn from these plots are (i) the CG arrangement seems to show better convergence towards LES and experiment than the corresponding UG arrangement and (ii) the f_k=0.7 case of the CG arrangement is considerably better in accuracy than the corresponding RANS result. These observations are especially evident near the boundaries adjoining the cavities where a majority of the disagreement was observed. The instantaneous contour plots for X-vorticity (Figs. 37 and 38), once again depict the fact that marginally more scales of flow are resolved when employing the CG arrangement.

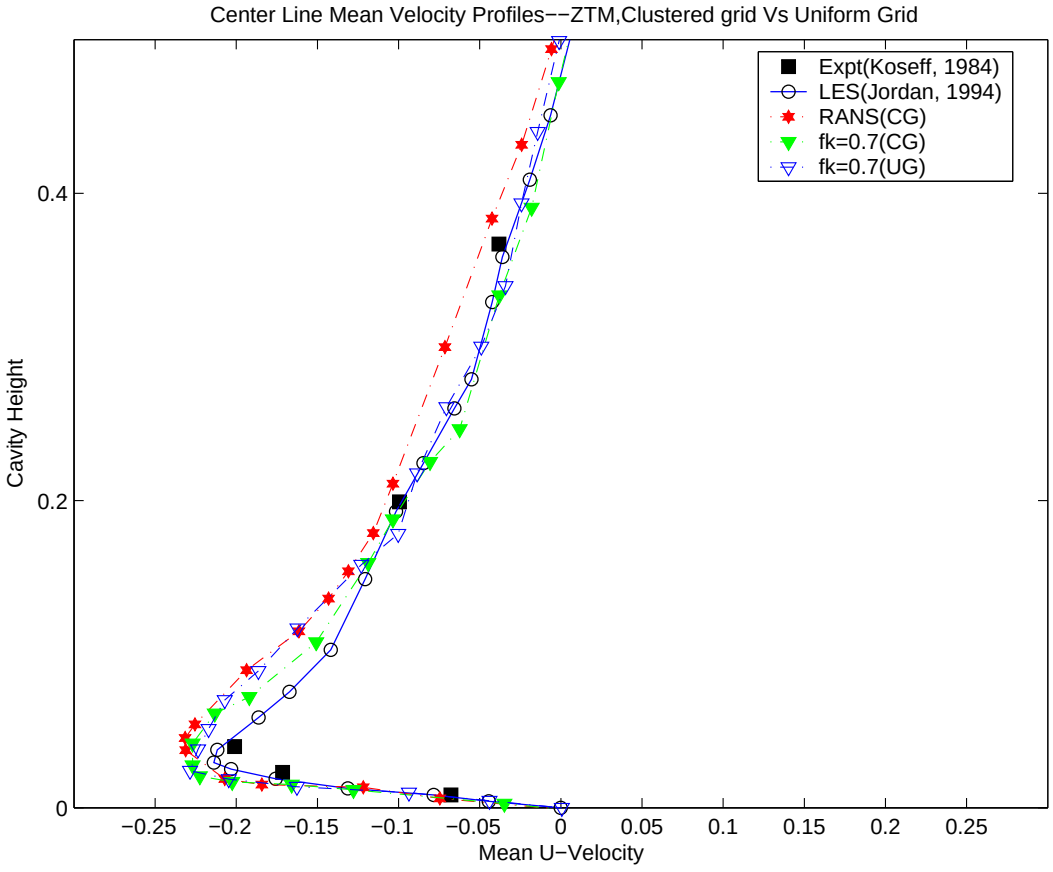

Fig. 35. Mean U-Velocity profiles, bottom wall closeup, $f_k = 0.7$, (CG Vs UG)

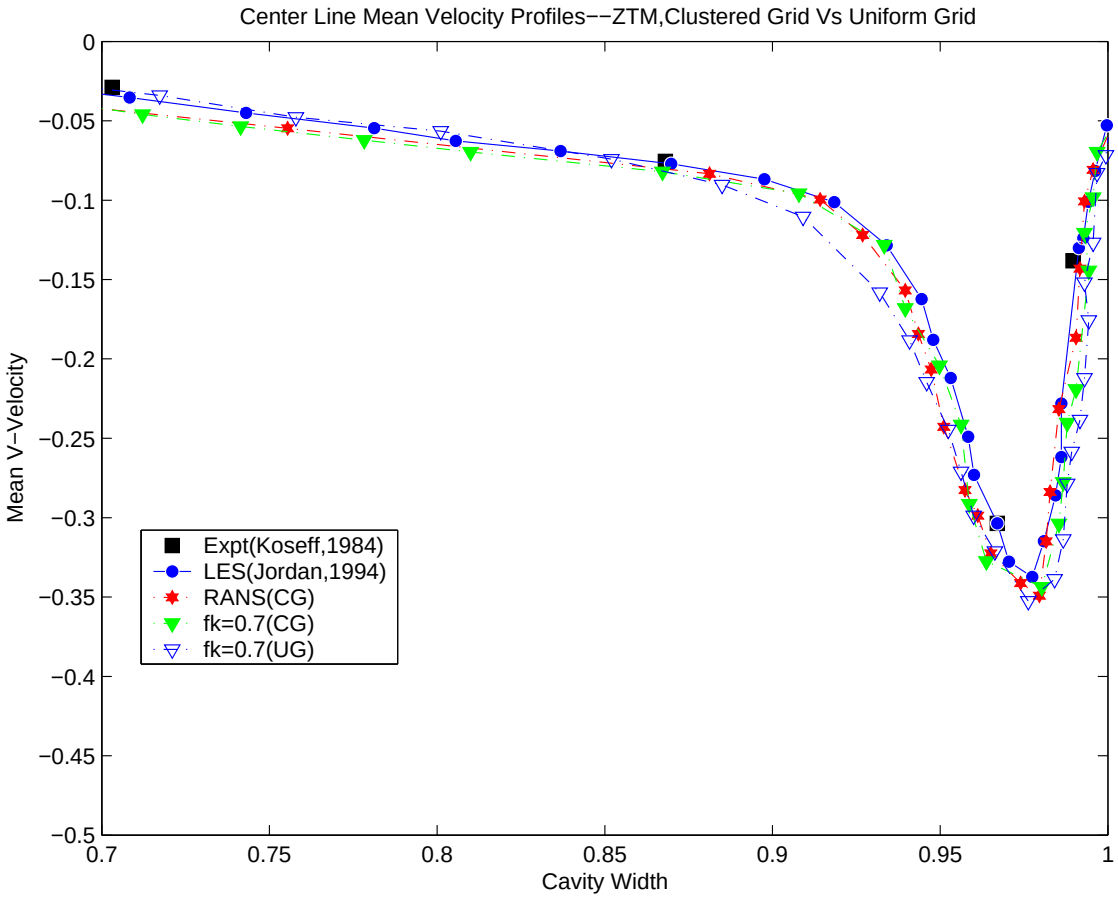

Fig. 36. Mean V-Velocity profiles, downstream wall closeup, $f_k = 0.7$, (CG Vs UG)

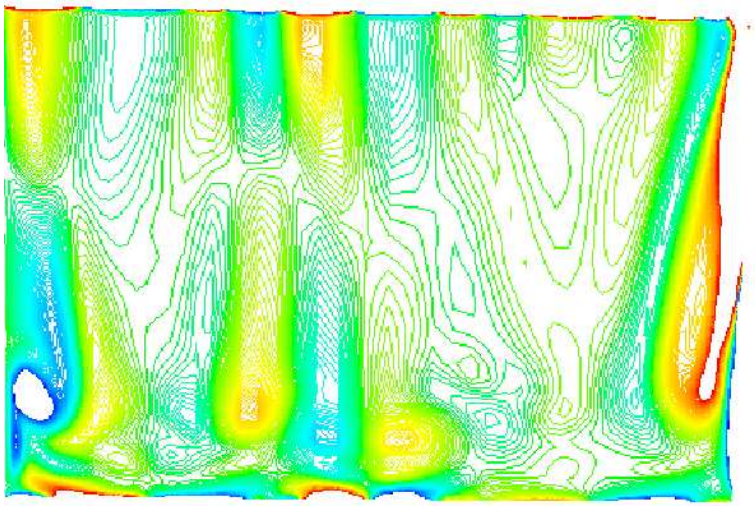

Fig. 37. X-Vorticity contours along downstream wall, ($f_k = 0.7$, CG)

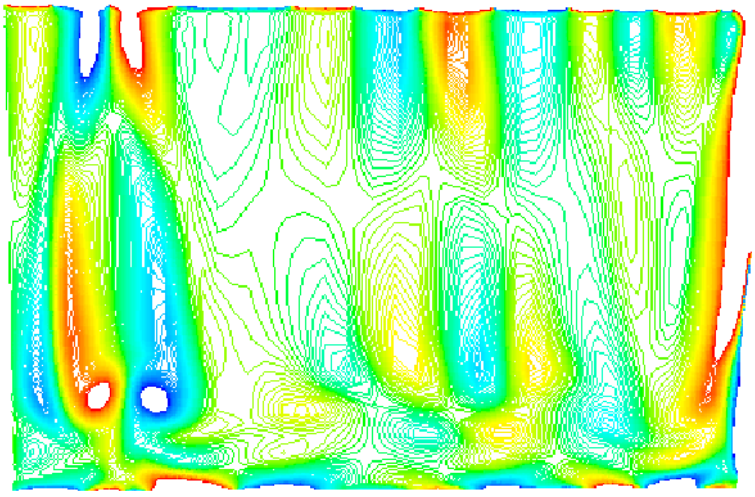

Fig. 38. X-Vorticity contours along downstream wall, ($f_k = 0.7$, UG)

As the value of f_k decreases, a significant improvement in the accuracy of the numerical solution is observed. This is apparent from the plots of statistical quantities along the cavity centerlines for various f_k values (0.5 (Figures 39, 40), 0.4 (Figs. 43, 44) and 0.2 (Figs. 47, 48)). These plots illustrate the fact that for a given f_k value, the CG arrangement gives closer agreement with LES and experiment than the corresponding UG arrangement. As the value of f_k is reduced, nearly LES-accurate results are obtained for the CG arrangement. This conclusion can be drawn by examining figures 51-54, where PANS calculations are compared against literature for all values of f_k using both grid arrangements. Figures 47 and 48 for f_k=0.2 show very close agreement with LES and experiment and are, in fact, nearly as accurate.

On comparing subsequent plots of X-vorticity contours for either grid arrangement, for f_k values of 0.5 (Figs. 41, 42), 0.4 (Figs. 45, 46) and 0.2 (Figs. 49, 50), it is observed that marginally more flow features are resolved, in terms of appearances of TGL vortex pairs. Maximum physical resolution is obtained for f_k=0.2, where almost 7 TGL vortex pairs (Fig. 49) can be seen. Figures 51-54 are plots that show the distribution of centerline mean velocities for the full cavity cross-section. These figures once again indicate that, on the whole, the ZT model performs better than the MT model for the entire cavity. On analyzing the results obtained in this section, it seems plausible to conclude that the physical resolution seems to depend on the prescription of f_k, while the numerical accuracy depends on the density and kind of grid used. This statement is substantiated by results presented in the following section, where a grid convergence study of the numerical solutionis presented.

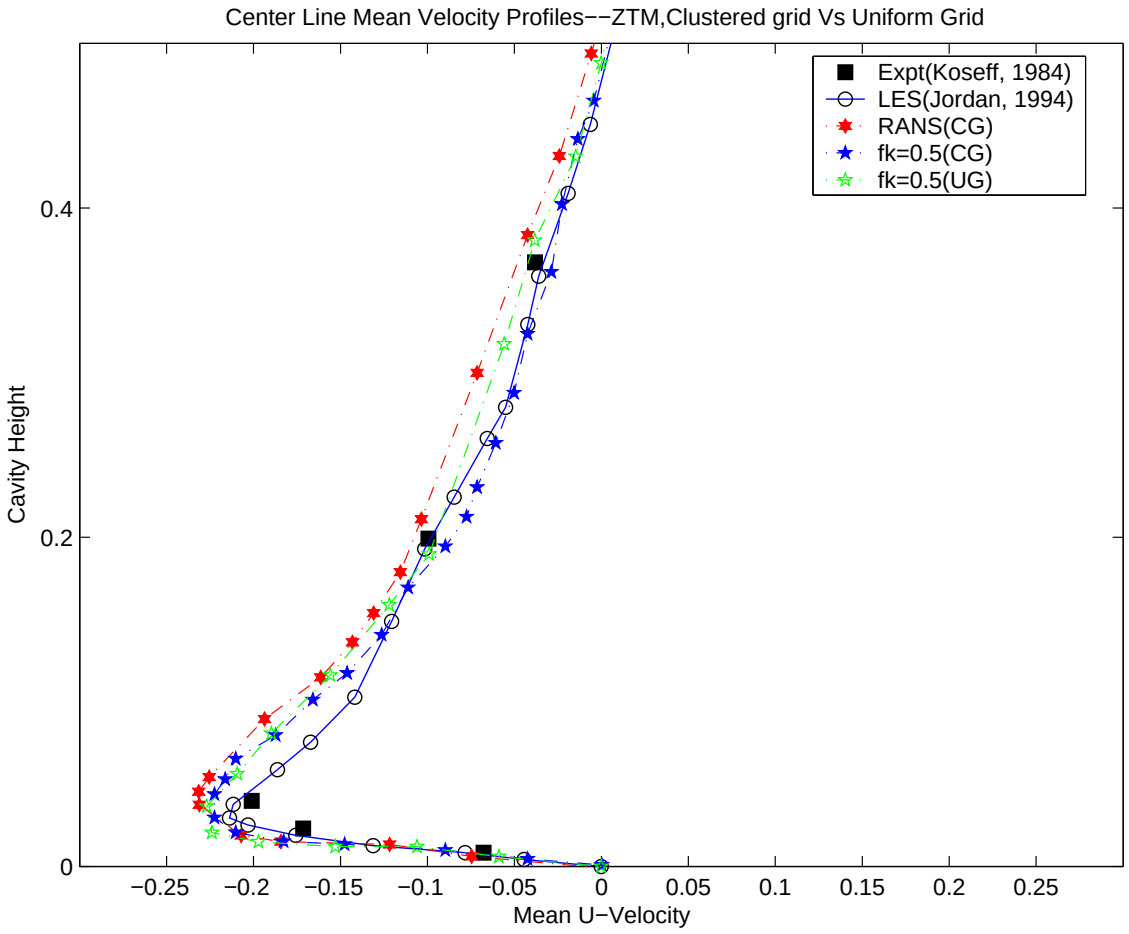

Fig. 39. Mean U-Velocity profiles, bottom wall closeup, $f_k = 0.5$, (CG Vs UG)

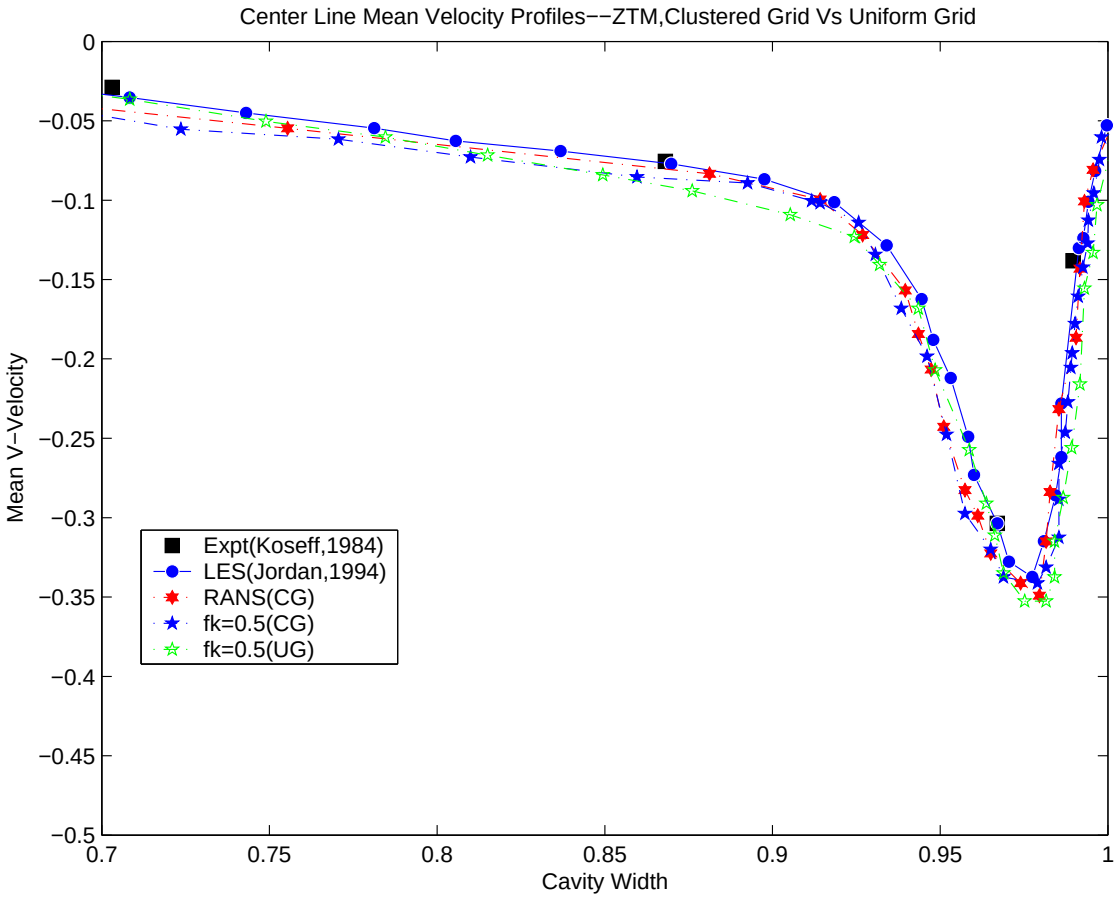

Fig. 40. Mean V-Velocity profiles, downstream wall closeup, $f_k = 0.5$, (CG Vs UG)

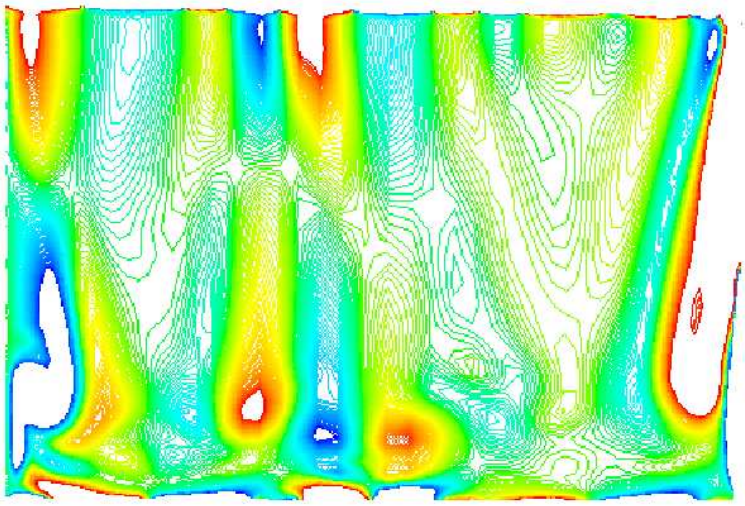

Fig. 41. X-Vorticity contours along downstream wall, ($f_k = 0.5$, CG)

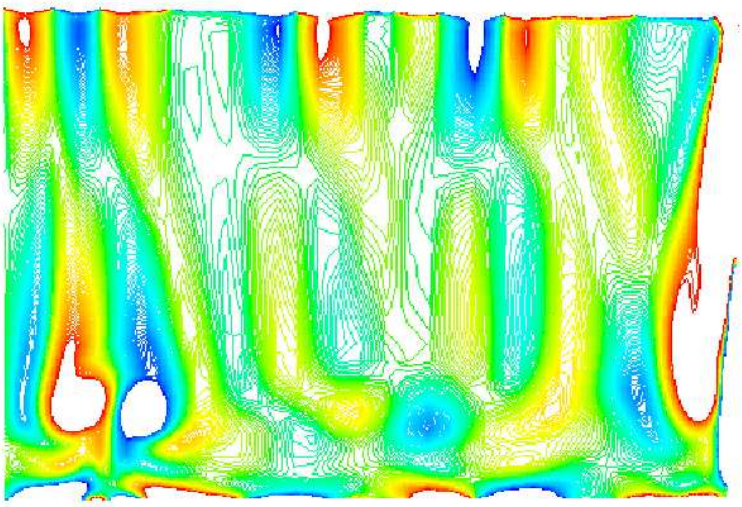

Fig. 42. X-Vorticity contours along downstream wall, ($f_k = 0.5$, UG)

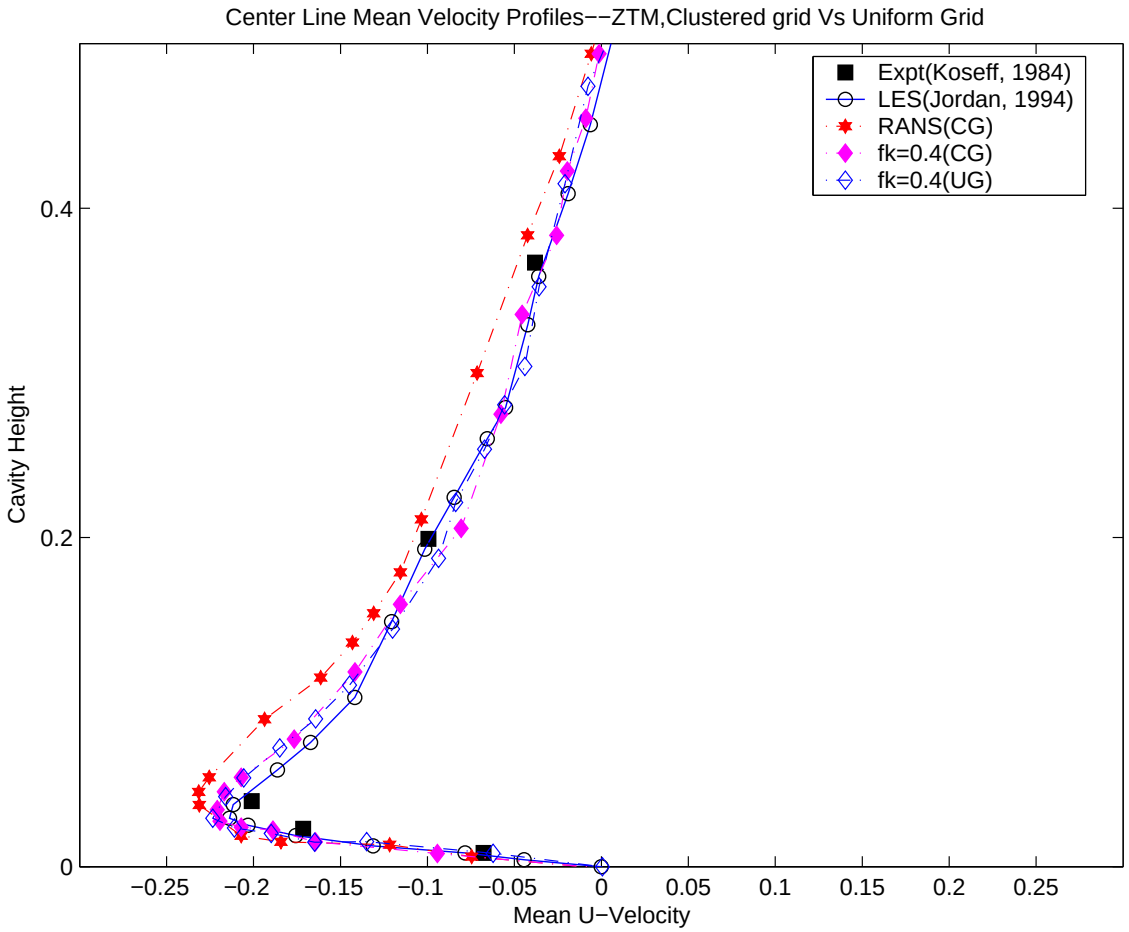

Fig. 43. Mean U-Velocity profiles, bottom wall closeup, $f_k = 0.4$, (CG Vs UG)

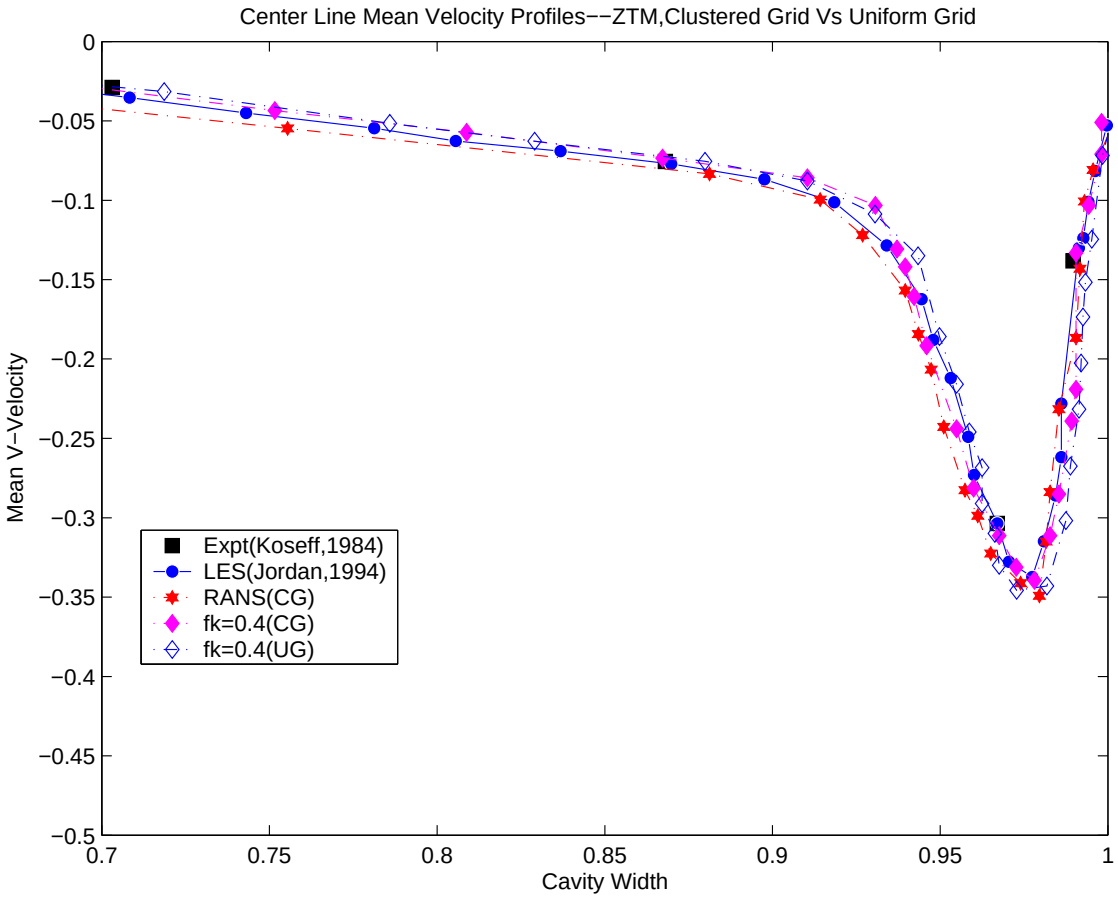

Fig. 44. Mean V-Velocity profiles, downstream wall closeup, $f_k = 0.4$, (CG Vs UG)

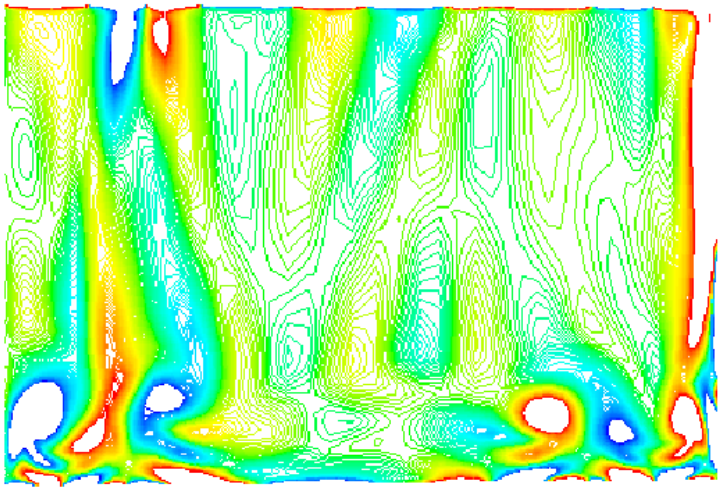

Fig. 45. X-Vorticity contours along downstream wall, ($f_k = 0.4$, CG)

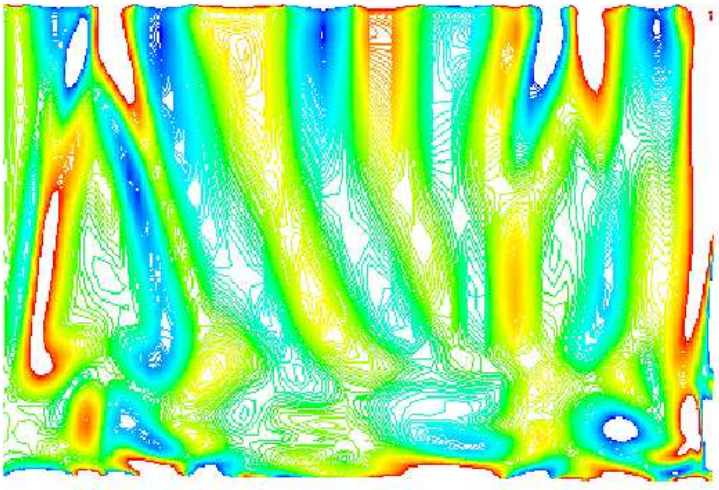

Fig. 46. X-Vorticity contours along downstream wall, ($f_k = 0.4$, UG)

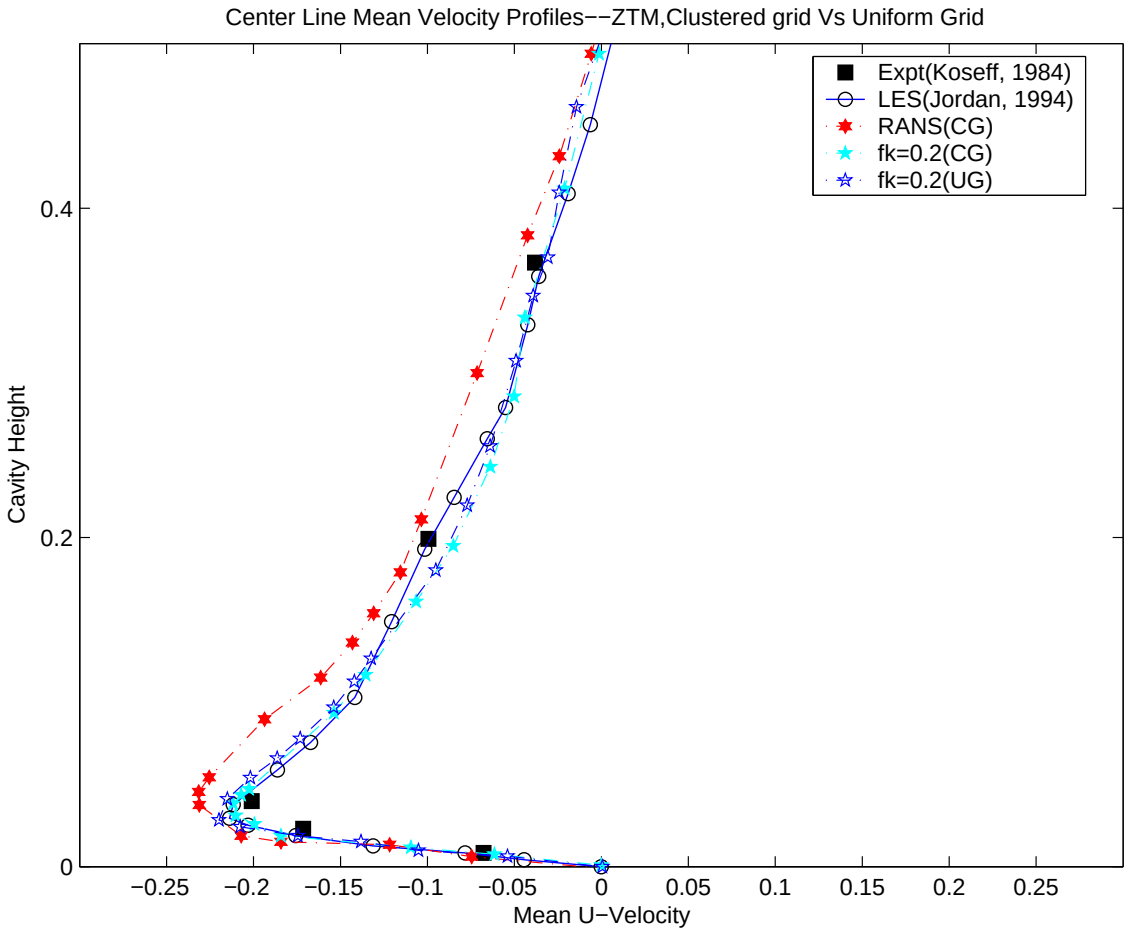

Fig. 47. Mean U-Velocity profiles, bottom wall closeup, $f_k = 0.2$, (CG Vs UG)

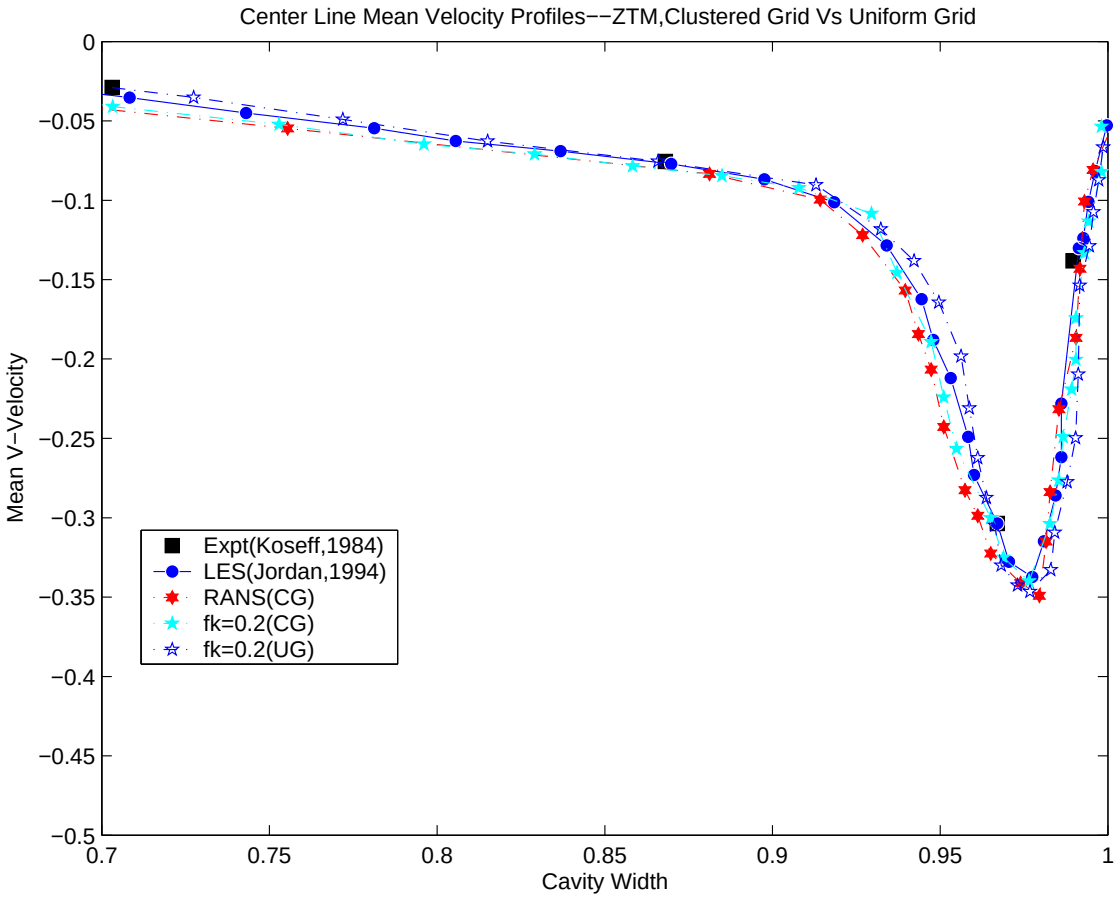

Fig. 48. Mean V-Velocity profiles, downstream wall closeup, $f_k = 0.2$, (CG Vs UG)

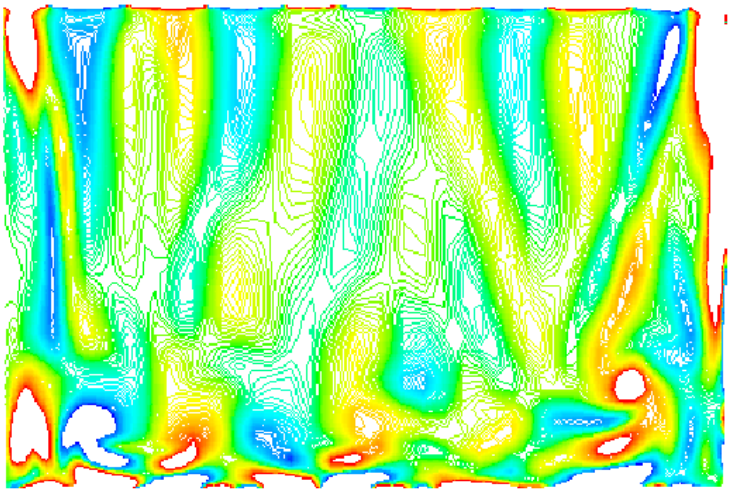

Fig. 49. X-Vorticity contours along downstream wall, ($f_k = 0.2$, CG)

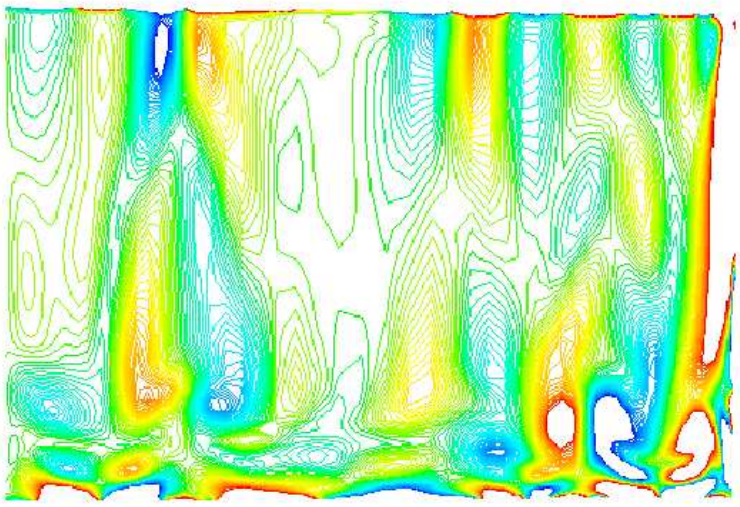

Fig. 50. X-Vorticity contours along downstream wall, ($f_k = 0.2$, UG)

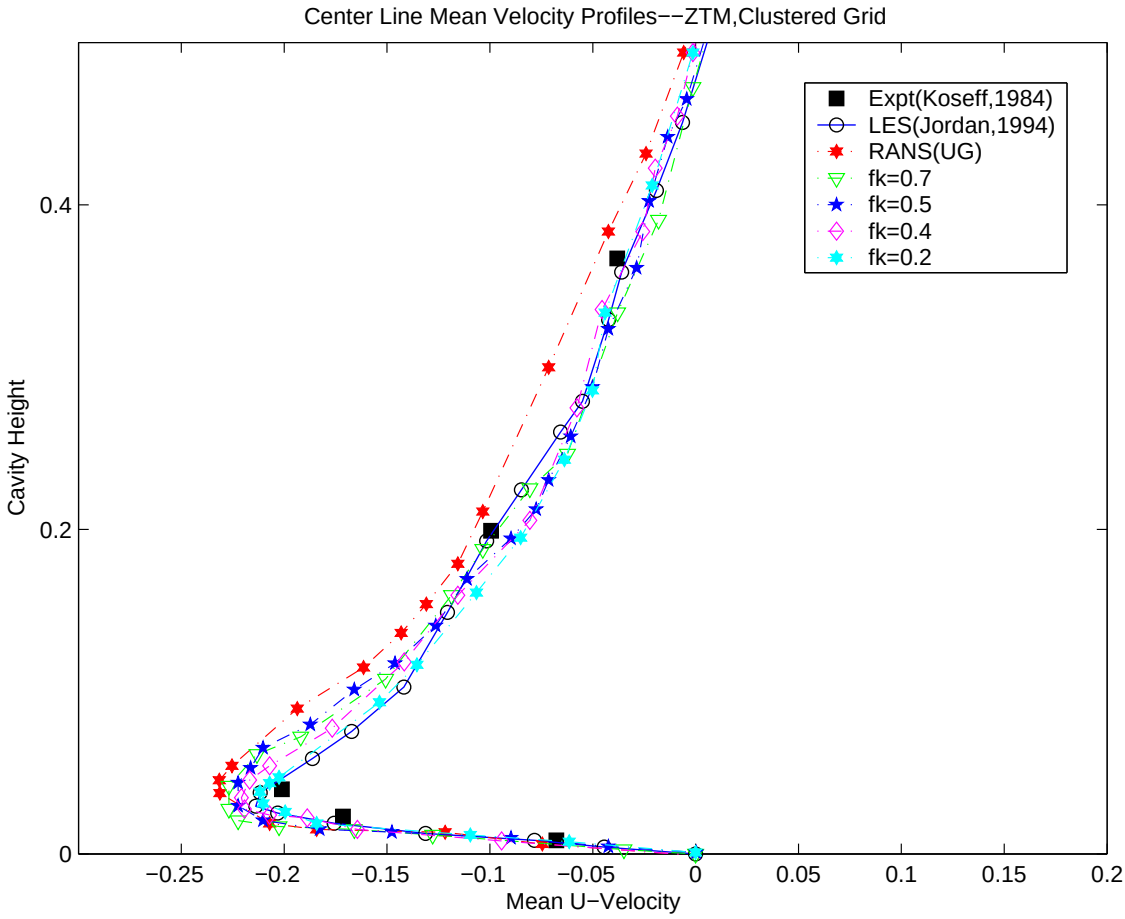

Fig. 51. Mean U-Velocity profiles, bottom wall closeup, (ZT, CG)

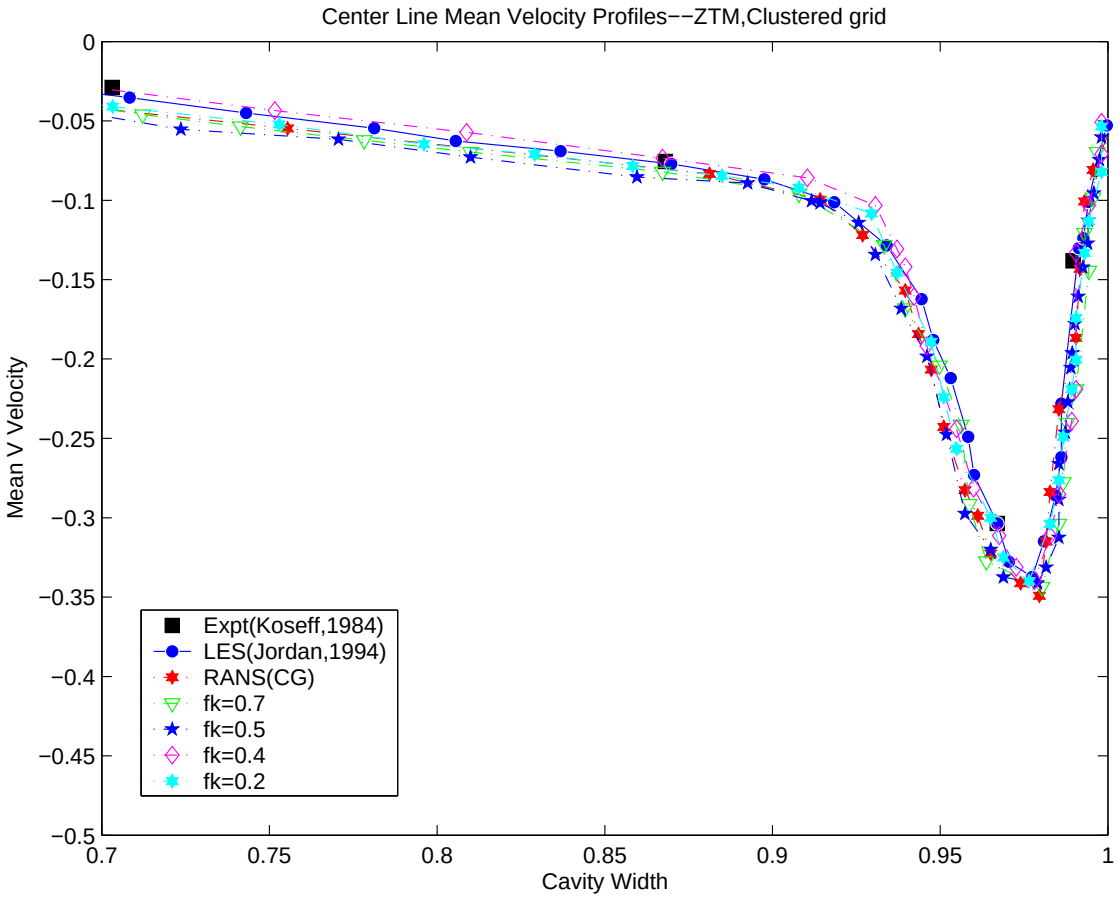

Fig. 52. Mean V-Velocity profiles, downstream wall closeup, (ZT, CG)

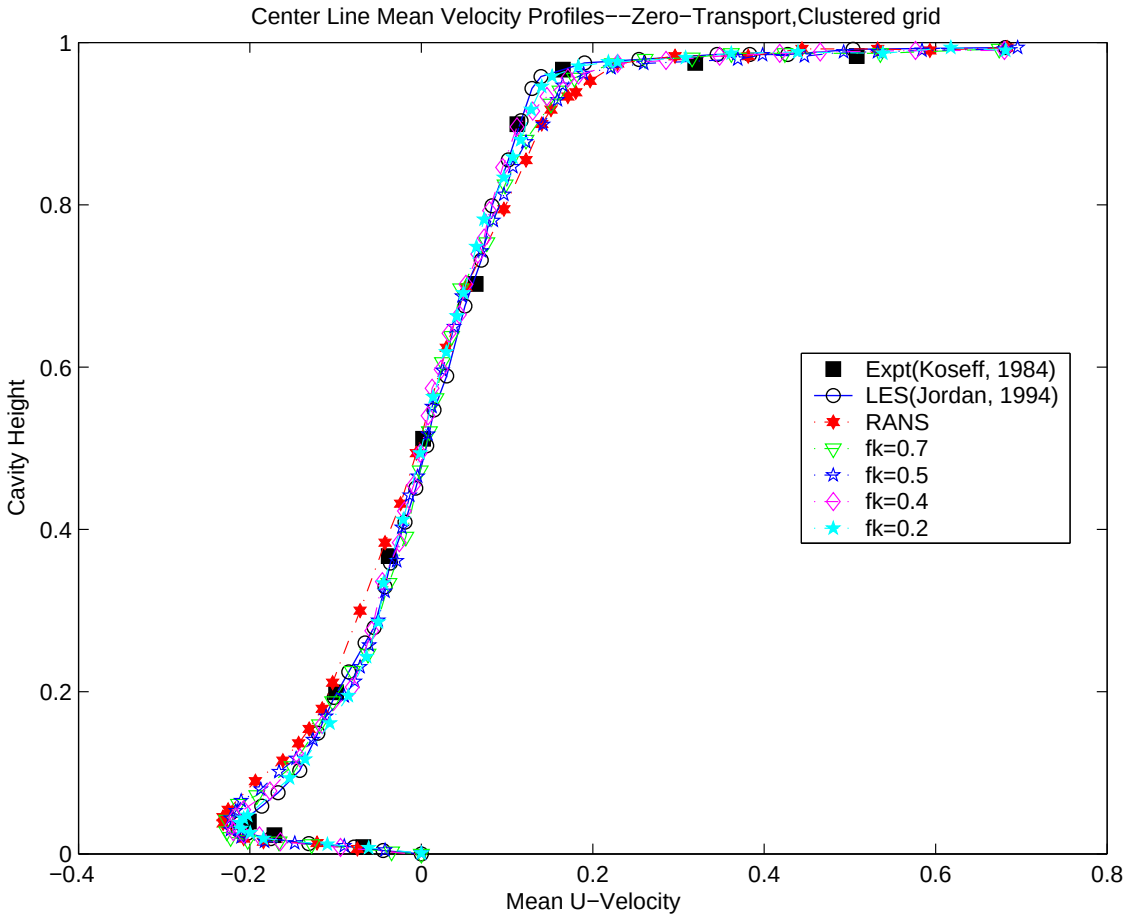

Fig. 53. Mean U-Velocity profiles, full cavity, (ZT, CG)

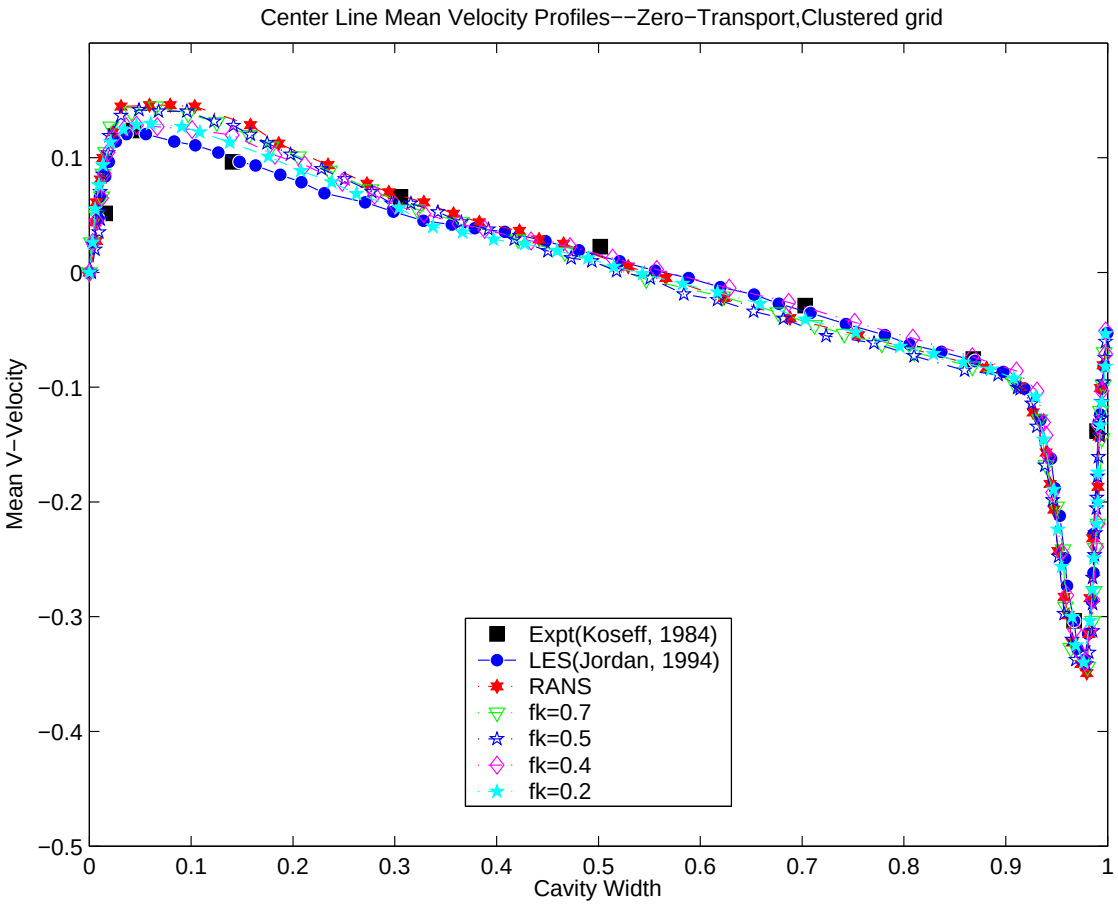

Fig. 54. Mean U-Velocity profiles, bottom wall closeup, (ZT, CG)

3. Grid Convergence

A very important issue in all of CFD is **grid convergence** or **grid insensitivity** [29]. As a result of the finite sizes of the finite-difference cells used in computations, numerical errors exist between the solution of the discretized equations and the exact solution of the differential equations. It is important to know the magnitude of such errors so that fine enough grids can be suitably employed to reduce the error to an acceptable level. Grid sensitivity studies should therefore be done for all CFD work and it is of even greater importance for turbulence-model computations because of the need to separate numerical error from the modeling error.

A common way to demonstrate grid convergence is to repeat the same computation with twice as many or half the number of grid points and compare the two solutions by checking the magnitude of the discretization error. This kind of check has been made in the present study and simulations have been performed for f_k values of 1.0 (RANS) and 0.7 using an 81*81*81 clustered grid arrangement. These results are compared with the results obtained by simulations performed using the previous grid sizes (refer Table II). From figures 55-58, it is useful to note that for both cases, the numerical error near the boundaries is considerably reduced by employing finer grids and it appears that the tendency is towards convergence with results presented in literature.

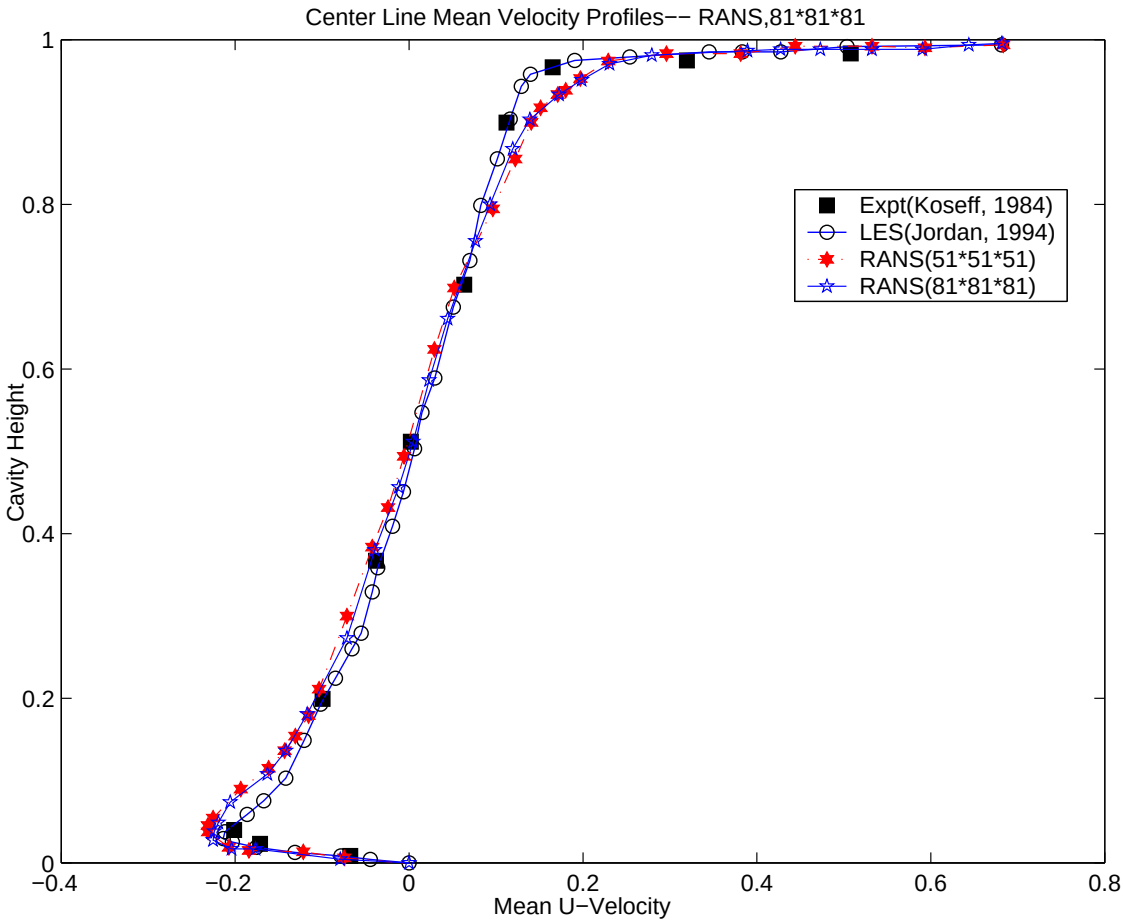

Fig. 55. Mean U-Velocity profiles, (RANS: 81*81*81 Vs 51*51*51)

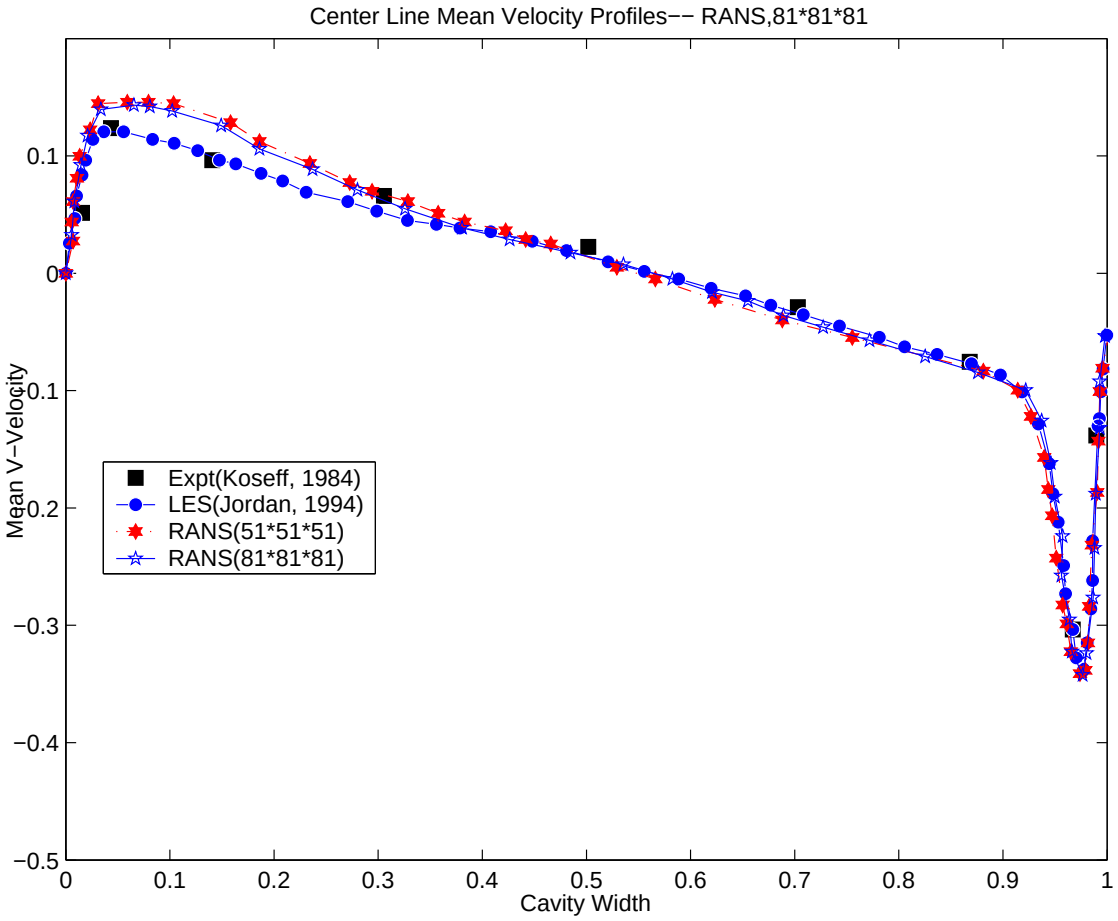

Fig. 56. Mean V-Velocity profiles, (RANS: 81*81*81 Vs 51*51*51)

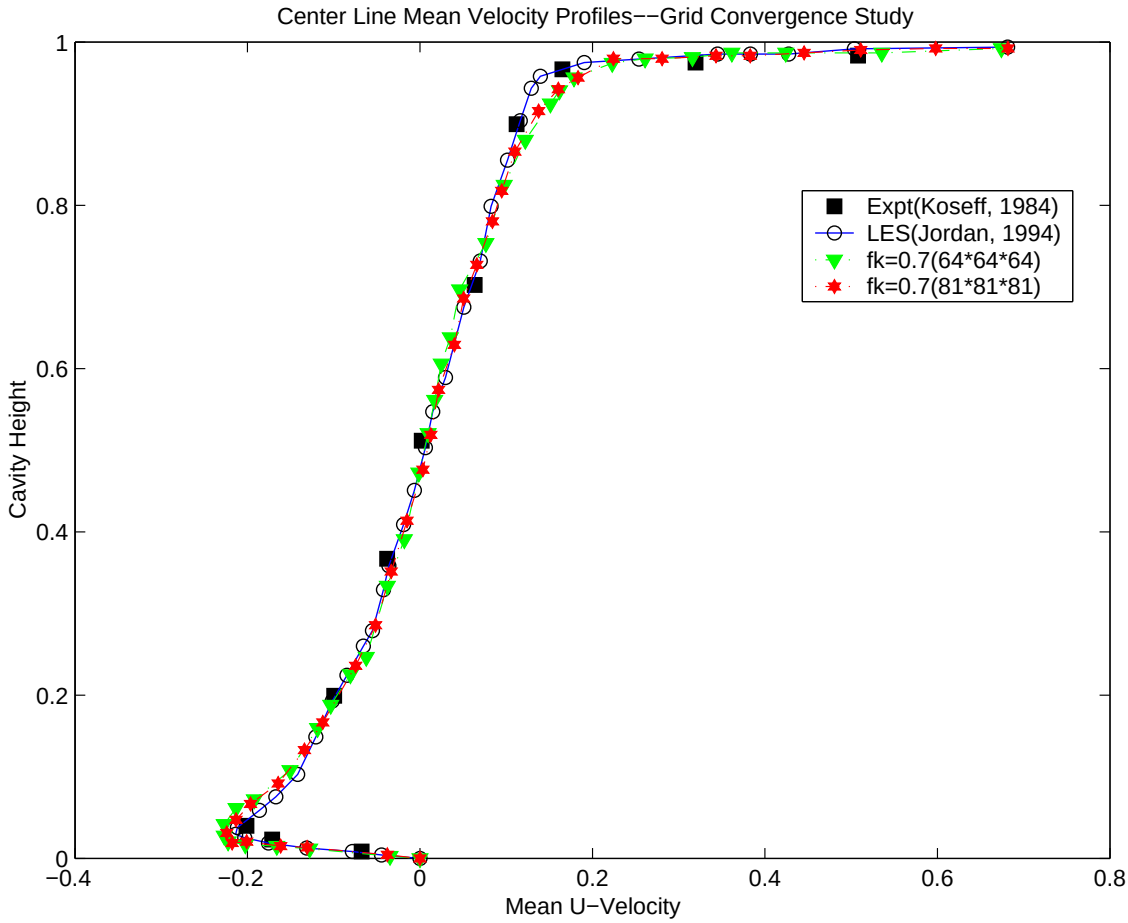

Fig. 57. Mean U-Velocity profiles, ($f_k = 0.7$: 81*81*81 Vs 64*64*64)

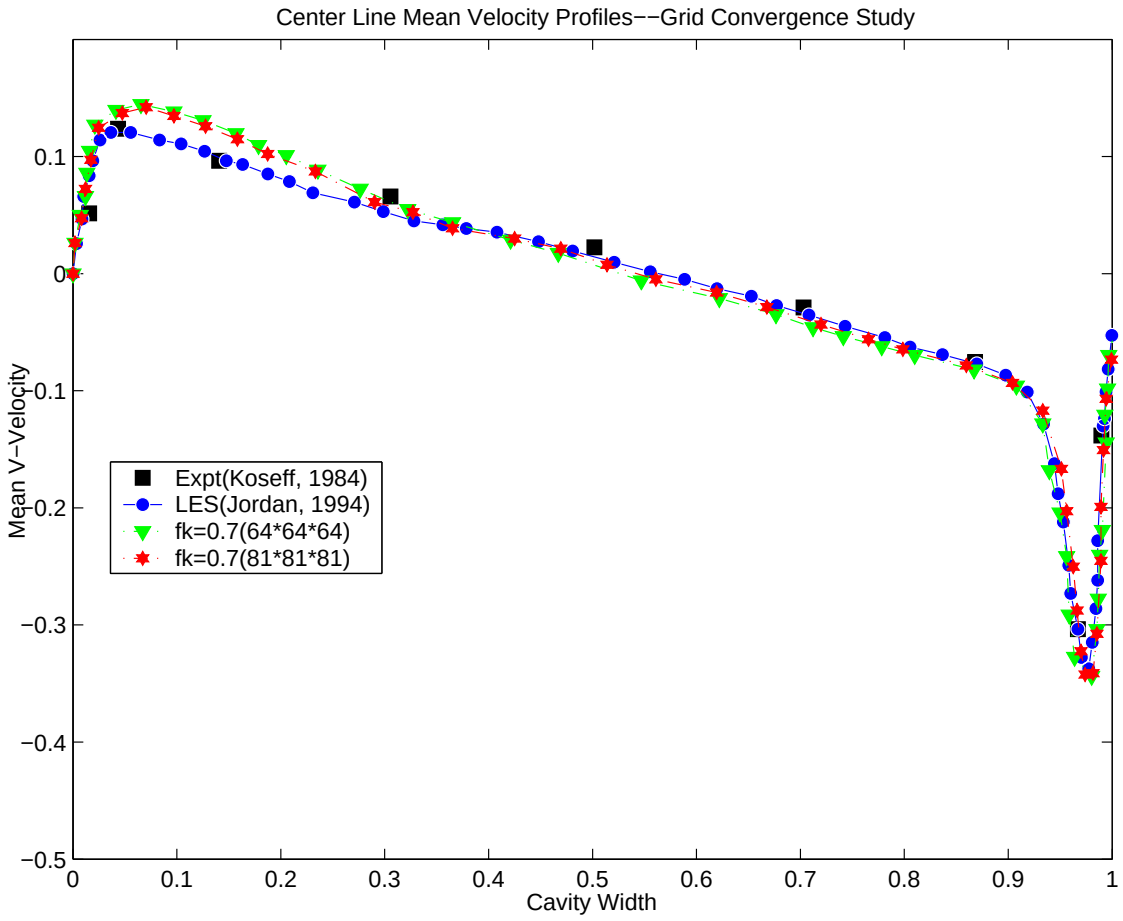

Fig. 58. Mean V-Velocity profiles, ($f_k = 0.7$: 81*81*81 Vs 64*64*64)

4. Results for Mixed Model

An additional simulation using a mixed transport model has also been also performed for $f_k = 0.5$, by changing the value of σ_{ϵ_u} as $\sigma_\epsilon \frac{f_k^2}{f_\epsilon}$ while preserving the standard value of $\sigma_{k_u} = \sigma_k$. This essentially implies that a ZT-type assumption is applied for unresolved dissipation (ϵ_u) while an MT-type assumption is applied for unresolved kinetic energy (K_u). The goal here is to determine the effect of both models on unresolved kinetic-energy (K_u) and dissipation (ϵ_u) and essentially to ascertain which of these assumptions performs better for either term. All computations have been performed on a clustered grid arrangement and results are compared for identical grid sizes.

From the plots of turbulent quantities along cavity centerlines (Figs. 59 and 60), only a very slight improvement near the walls adjoining the boundaries can be noticed when the mixed model is compared against the ZT model. This demonstrates the fact that the ZT model performs better than or is superior to the MT model for ϵ_u, while both models are adequate for K_u, and this is in accordance with the theory discussed in chapter III.

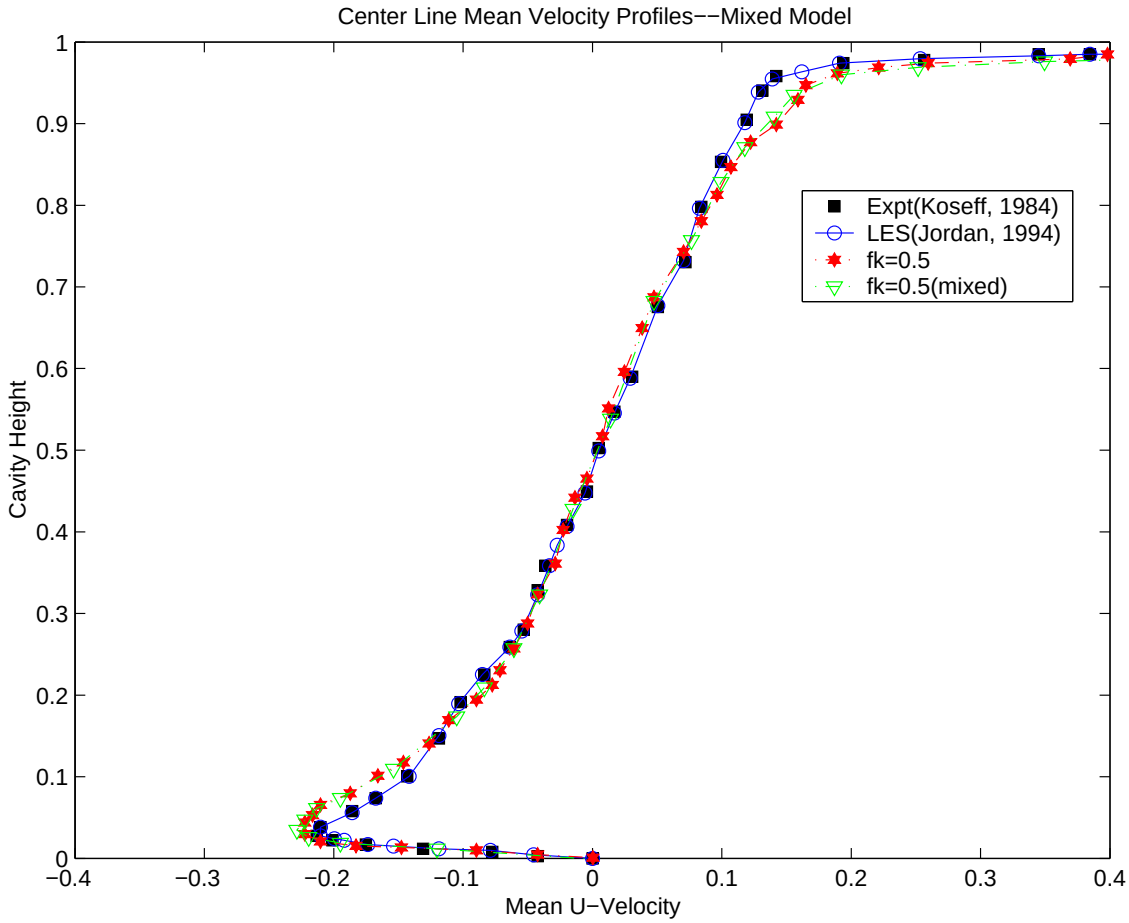

Fig. 59. Mean U-Velocity profiles, (Mixed Model, CG)

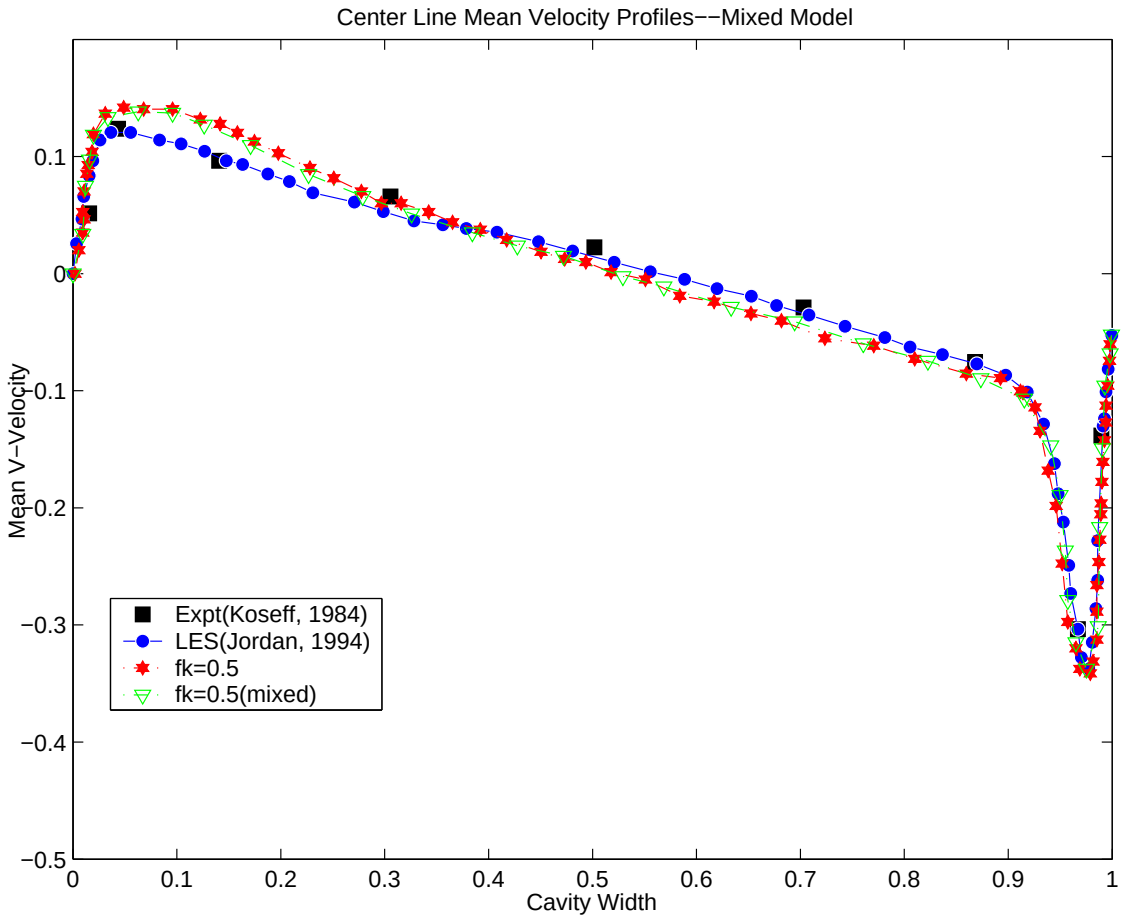

Fig. 60. Mean V-Velocity profiles, (Mixed Model, CG)

5. Results for SAR=0.5:1:1 and 1:1:1

Simulations have also performed to observe the effects of reducing SAR on the accuracy of PANS calculations and compare these with LES results available in literature (Prasad et al, 1989 [19]). These were done for a single f_k value of 0.5, on spanwise aspect ratios of 0.5:1:1 and 1:1:1. From figures 61 and 62, it is observed that at the given high Reynolds number ($Re = 10,000$), the plots for centerline mean velocities have smoother profiles than the corresponding LES results at the boundaries. On comparing both results, it is observed that PANS seems to be performing well as the center of the cavity is approached.

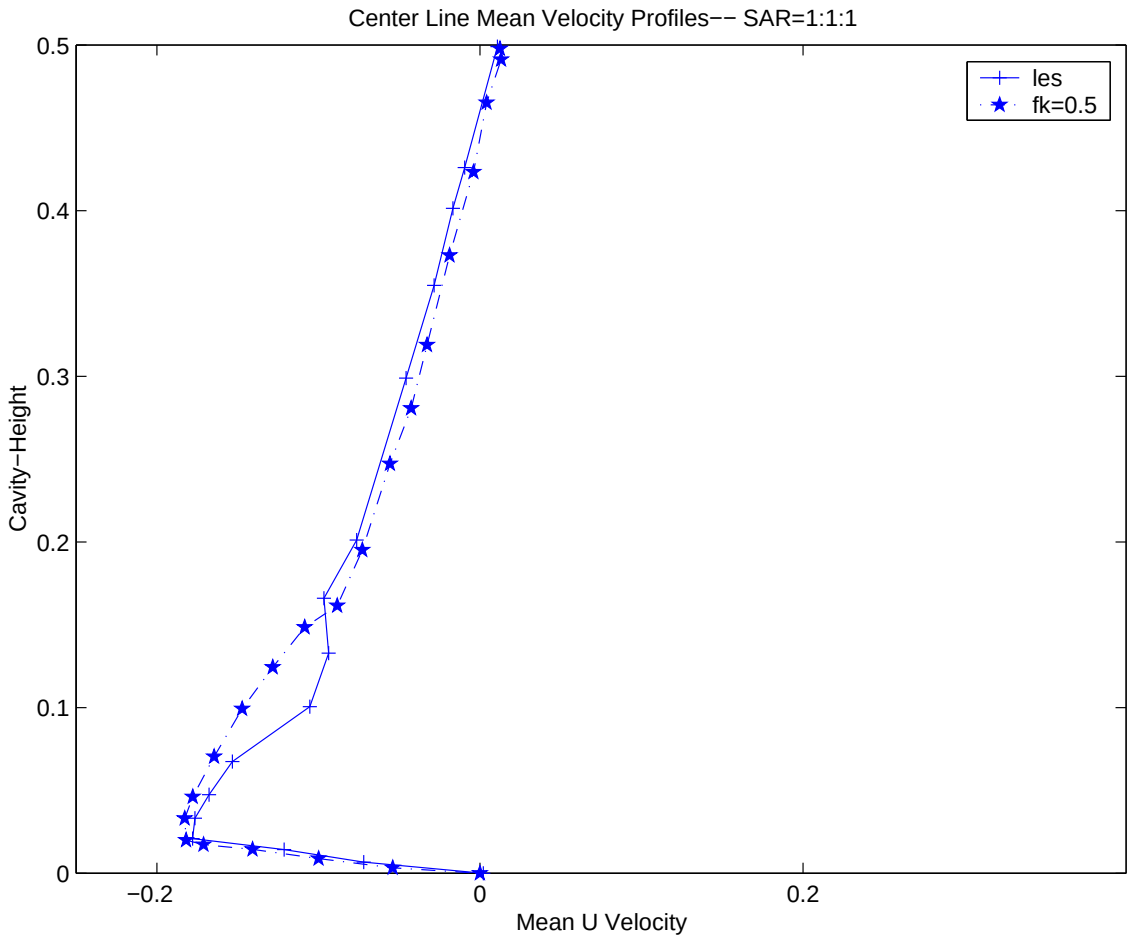

Fig. 61. Mean U-Velocity profiles for SAR = 1:1:1, bottom wall closeup, (ZT, CG)

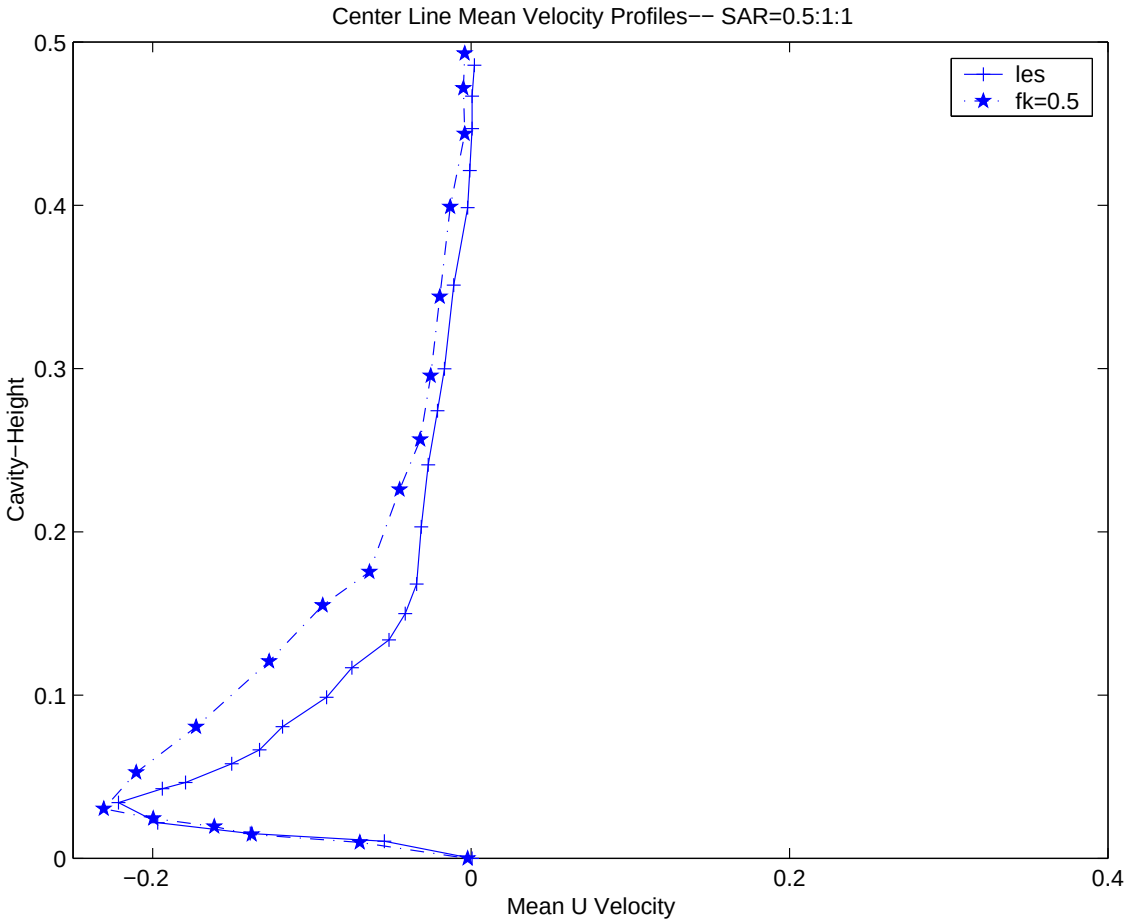

Fig. 62. Mean U-Velocity profiles for SAR = 0.5:1:1, bottom wall closeup, (ZT, CG)

CHAPTER VI

SUMMARY AND CONCLUSIONS

In the present study, a detailed numerical investigation of the three-dimensional lid-driven cavity flow is carried out using a new turbulence modeling technique, know as the Partially Averaged Navier Stokes method or PANS. Flow studies have been conducted at Re=10000 on a lid-driven cavity for spanwise aspect ratios (SAR) of 3:1:1,1:1:1 and 0.5:1:1, with the top surface imparted with a constant velocity of 1 m/s. The investigation consists of two parts. The first primarily focuses on the effects of two turbulent transport models (the Zero-Transport (ZT) and Maximum-Transport (MT)) on PANS calculations to ascertain which model performs better for K_u and ϵ_u. The second focuses on the effect of grid sketching on the accuracy of the numerical solution obtained by PANS, which is explained by comparing the results generated on a clustered grid as against those generated on a uniform grid.

The main conclusions that can be drawn by observing all the results are:

(i) as the value of f_k is decreased from 1 (corresponding to RANS) to 0 (corresponding to DNS) more scales of flow are resolved in terms of the appearance of flow features, such as the TGL vortices, as evident from the contour plots of X-vorticity,

(ii) the ZT model is superior to the MT model for unresolved dissipation (ϵ_u),

(iii) both models are adequate for unresolved kinetic energy (K_u) and

(iv) for a given grid size, grid sketching improves the accuracy of the numerical solution, as seen by comparisons of statistical quantities with LES and experiment available in literature.

As a final note, in view of all the results, it is seems justifiable to conclude that the PANS model is capable of serving as a **bridging model** between RANS and DNS.

REFERENCES

[1] Chiang, T. P., Sheu, W. H., and Hwang, R. R., 1998, "Effect of Reynolds Number on the Eddy Structure in a Lid-Driven Cavity", *International Journal for Numerical Methods in Fluids*, Vol. 16, pp. 557-579.

[2] Roshko, A., 1955, NACA Tech. Notes, No. 3488.

[3] Ghia, U., Ghia, K. N., and Shin, G. T., 1982, "Solutions of Incompressible Flow Using the Navier-Stokes Equations and a Multi-grid Method", *Journal of Computational Physics*, Vol. 48, pp. 387-411.

[4] Gustafson, K., and Halasi, K., 1986, "Vortex Dynamics of Cavity Flows", *Journal of Computational Physics*, Vol. 64, No. 2, pp. 279-319.

[5] Young, D. L., Liggett, J. A., and Gallagher, R. H., 1976, "Unsteady Stratified Circulation in a Cavity", *J.Eng.Mech.Div.*, ASCE 102, No. EM6, pp. 1009-1023.

[6] Ideriah, F. J. K., 1978, "On Turbulent Forced Convection in a Square Cavity", *Numerical Methods in Laminar/Turbulent Flow*, Proceedings 1st International Conference, Newark, NJ, pp. 257-269.

[7] Gaskell, P. H., and Lau, A. K. C., 1988, "The Method of Curvature Compensation and Its Use in the Prediction of Highly Recirculating Flows", *AIAA/ASME/SIAM/APS 1st National Fluid Dynamics Congress*, pp. 272-279.

[8] Soh, W. Y., and Goodrich, J. W., 1988, "Unsteady Solutions of Incompressible Navier-Stokes Equations",*Journal of Computational Physics*, Vol. 79, pp. 113-134.

[9] Koseff, J. R., and Street, R. L., 1984a, "Visualization Studies of a Shear Three-Dimensional Recirculation Flow", ASME *J. Fluid. Eng.*, Vol. 106, No. 1, pp. 21-29.

[10] Pan, F., and Acrivos, A., 1967, "Steady Flows in Rectangular Cavities", *J.Fluid.Mech*, Vol. 28, pp. 643-655.

[11] Mills, R. D., 1965, "Numerical Solutions of the Viscous Equations for a Class of Closed Flows", *J. Roy. Aero. Soc. 69*, pp. 714-718.

[12] Koseff, J. R., and Street, R. L., 1984b, "On End-Wall Effects in a Lid-Driven Cavity Flow", ASME *J. Fluid. Eng.*, Vol. 106, No. 1, pp. 385-389.

[13] Koseff, J. R., and Street, R. L., 1984c, "The Lid-Driven Cavity Flow: A Synthesis of Qualitative and Quantitative Observations ", ASME *J. Fluid. Eng.*, Vol. 106, No. 1, pp. 390-398.

[14] Ramanan, N., and Homsy, G. M., 1994, "Liner Stability of Lid-Driven Cavity Flow", *Physics of Fluids*, Vol. 6, pp. 2690.

[15] Aidun, C. K., Triantafillopoulos, N. G., and Benson, J. D., 1991, "Global stability of a Lid-Driven Cavity with Throughflow: Flow Visualisation Studies", *Physics of Fluids A*, Vol. 3, pp. 2081-2091.

[16] Jordan, S. A., and Ragab, S. A., 1994, "On the Unsteady and Turbulent Characteristics of Three-Dimensional Shear-Driven Cavity Flow ", *Journal of Fluids Engineering*, Vol. 116, pp. 439-449.

[17] Kim, J., and Moin, P., 1985, "Application of a Fractional-Step Method to Incompressible Navier-Stokes Equations", *Journal of Computational Physics*, Vol. 59, pp. 308-310.

[18] Frietas, C. J., Street, R. L., Findikakis, A. N., and Koseff, J. R., 1985, "Numerical Simulation of Three-Dimensional Flow in a Cavity", *International Journal of Numerical Methods in Fluids*, Vol. 5, No. 6, pp. 561-576.

[19] Prasad, A. K., and Koseff, J. R., 1989, "Reynolds Number and End-Wall Effects on a Lid-Driven Cavity Flow", *Physics of Fluids*, Vol. 1, No. 2, pp. 208-218.

[20] Spalart, P. R., 2000, "Trends in Turbulent Treatments", AIAA, *Fluids 2000*, 2000th ed. Denver, CO, 2000 pp. 2000-2306.

[21] Germano, M., 1992, "Turbulence: The Filtering Approach", *J.Fluid.Mech*, Vol. 124, pp. 413-423.

[22] Girimaji, S. S., 2003, "Partially-Averaged Navier-Stokes Method: A Variable Resolution (from RANS to DNS) Turbulence Model", submitted to *Physics of Fluids*.

[23] Lilly, D. K., 1966, "On the Application of Eddy Viscosity Concept in the Inertial Sub-Range of Turbulence", *NCAR*, Boulder, Colorado, Manuscript, 123.

[24] Deardorff, J. W., 1970, "A Numerical Study of Three-Dimensional Channel Flow at Large Reynolds Numbers", *J.Fluid.Mech*, Vol. 41, pp. 453-480.

[25] Khorrami, M. R., Singer, B., and Berkman, M. E., 2002a, "Time-accuarate Simulations and Acoustic Analysis of a Slat Free Shear Layer", *AIAA*, Vol. 40, No. 7, pp. 1284-1291.

[26] Khorrami, M. R., Singer, B., and Lockard, D., 2002b, "Time-accuarate Simulations and Acoustic Analysis of a Slat Free Shear Layer, Part 2", in *AIAA Journal*, Breckenridge, CO, AIAA/CEAS Aeroacoustic Conference and Exhibit, pp. 2002-2579.

[27] Girimaji, S. S., October 2002, "Unsteady RANS Method for Turbulence: Fundamentals and Model Development", under consideration for publication in *J.Fluid.Mech.*

[28] *The FLUENT Users Manual*, 2001st ed., Texas A & M University, College Station, TX.

[29] Wilcox, C. D., 1994, "Turbulence Modeling for CFD", 1st ed., DCW Industries Inc., La Canada,CA.

VITA

Aditya Murthi was born in New Delhi, India. He obtained his Bachelors of Engineering degree (with honors) in mechanical engineering from Amrita Institute of Technology and Science, Bharathiyar University, Coimbatore, India in April 2001. Before joining Texas A&M University in Fall 2001, he taught at an Aeronautical Institute. He intends to pursue the Ph.D. degree, after he completes his master's degree.

The typist for this thesis was Aditya Murthi.